(61)

Hot-Filament Chemical Vapor Deposition of Selectively Deposited Diamond and Silicone Thin Films

by

Michael Chiu Kwan

M.S., Chemical Engineering Practice
Massachusetts Institute of Technology, 1993

B.S., Chemical Engineering
California Institute of Technology, 1991

SUBMITTED TO THE DEPARTMENT OF CHEMICAL ENGINEERING IN PARTIAL FULFILLMENT OF THE REQUIREMENTS FOR THE DEGREE OF

DOCTOR OF PHILOSOPHY IN CHEMICAL ENGINEERING
AT THE
MASSACHUSETTS INSTITUTE OF TECHNOLOGY

SEPTEMBER, 1997

Signature of Author: _____
Department of Chemical Engineering
July 15, 1997

Certified by: _____
Karen K. Gleason
Associate Professor of Chemical Engineering
Thesis Supervisor

Accepted by: _____
Robert E. Cohen
St. Laurent Professor of Chemical Engineering
Chairman, Committee for Graduate Students

Hot-Filament Chemical Vapor Deposition of Selectively Deposited Diamond and Silicone Thin Films

by

Michael C. Kwan

Submitted to the Department of Chemical Engineering on
July 15, 1997 in Partial Fulfillment of the Requirements
for the Degree of Doctor of Philosophy in Chemical
Engineering

ABSTRACT

Hot-filament pyrolytic chemical vapor deposition was used to deposit thin films of diamond and silicone. While these materials have very different materials properties, the CVD process to make them share many similarities, including precursor generation, gas phase transport, and surface reaction.

One of the key hurdles to the successful commercialization of diamond thin films for bulk applications such as thermal management substrates is the low rate of deposition. While it has been known for some time that the presence of atomic hydrogen is very important to the diamond deposition process, there has been no clear consensus as to whether the gas phase transport limited concentration of H-atoms at the substrate is the primary determining factor for the growth rate.

In order to try to make that determination, two different methods were used to selectively nucleate diamond deposits on a silicon substrate. The variation in deposition rate across the substrate was measured by analyzing the difference in surface coverage. This variation was analyzed through a three dimensional, finite-difference model that included growth species generation, gas phase transport and surface reaction. A Damköhler number of 1.5 was used to fit the model to the data, indicating that the growth rate was transport limited. Furthermore, an assumption of hydrogen atoms as the growth limiting species yielded a first order surface reaction rate constant that matched well with literature values for H-atom abstraction from a hydrogenated diamond surface whereas the assumption that methyl radicals were the growth limiting species did not result in a kinetic rate constant that matched the estimated rate constant for methyl addition to a diamond lattice.

The hot-filament CVD technique was applied in a novel manner to deposit polyorgano-siloxanes (silicone-like) thin films with the structure, $-(O-RR'Si-O)_n-$. All of the literature on polyorganosiloxane films to date have used plasma methods to activate the gas phase. Characterization with FTIR, XPS, and ^{29}Si NMR demonstrate that the film is composed of long chains or large rings of greater than ten dimethylsiloxane repeating units. Additional evidence indicates that the film is methyl deficient relative to a conventionally

polymerized polydimethylsiloxane standard and that Si-Si bonds could be acting as crosslinks.

Because of the similarities between the two processes, a two dimensional version of the finite difference generation / transport / reaction model was applied to the silicone deposition system. The model was fitted to a baseline deposition with a Damköhler number of 6, again indicating a transport limited system. The effect on the deposition rate across a 2" Si wafer was measured as the reactor pressure and filament-to-substrate spacing were halved. When applied to simulate these new conditions, the model correctly predicted that the growth rate was not affected by the pressure change and that the growth rate in the center of the wafer nearly doubled as the filament-to-substrate spacing was halved.

Thesis Supervisor: Karen K. Gleason
Title: Associate Professor of Chemical Engineering

Dedicated to my parents

献给我父母

ACKNOWLEDGEMENTS

This thesis would not have been possible without my advisor, Karen Gleason. Her willingness to let me pursue my own ideas and directions plus her patient teaching and even temper have made my Ph.D. experience a successful one. I am likewise indebted to the members of my thesis committee, Profs. Herb Sawin, Jack Howard, and Klavs Jensen, for helpful discussions in their areas of expertise. I have also had many great teachers in the practical aspects of doing science in the Center for Materials Science and Engineering, including Mike Frongillo, Rich Perilli, Tim McClure, May Lu, and Libby Shaw.

Any mention of research related discussions would not be complete without bringing up the day-to-day interactions with the members of my research group. I am particularly grateful to Colin Wolden for discussions on all aspects of diamond CVD and Bruce Scruggs for making life in lab "interesting" as only he can. I would also like to thank Saibal Mitra, Dave Lathrop, Scott Limb, Cathy Labelle, Wai-Kit Chang, Ken Lau, Leslie Loo, and Hilton Pryce Lewis for their assistance and general presence in lab. Life in lab just wouldn't have been the same without all of you.

Because working on a thesis is sometimes more than one person can handle, I would also like to acknowledge the help of the chemical engineering support staff, particularly Craig Abernathy, Kathy Brownell, Ilda Moura, and Janet Fischer and Elaine Aufiero-Peters in the graduate student office.

Outside of work, I would like to thank Ralph Lin, Mike Chou, and Jinha Kim for their friendship over the last six years. Their constant presence, love for life, and general willingness to do all sorts of stuff have made life at MIT actually fun at times. I have also made many new friends while at MIT, both within the department and without. They are too numerous to mention by name but of them all, one in particular holds a special place in my heart. My relationship with my wife, Sharlene Liu, began at MIT and has been a source of happiness and inspiration for me the last few years. I think that it's fair to say that without her, I would probably still not be done today.

Last of all, I would like to thank my family - my brother, Jimmy, for being there, and my parents for their support, their insistence that I hit the books before all else, and for providing the means by which I have come to where I am today.

Thank you all.

TABLE OF CONTENTS

LIST OF FIGURES

LIST OF TABLES

1. INTRODUCTION

Pyrolytic chemical vapor deposition (PyCVD) refers to the deposition of a material from the reaction of gas phase precursor molecules that have been generated pyrolytically; i.e., by thermal means at a hot surface. PyCVD is distinct from some other types of thermal CVD processes in which the growth on a heated substrate results from the cracking of molecules on the substrate. Examples include the CVD of polysilicon, silicon nitride, silicon dioxide and tungsten.[1] PyCVD is characterized by a relatively cool substrate which does not generate growth precursors or participate in the reaction. PyCVD is also different from combustion processes since no oxygen is used. Previous examples of PyCVD processes include diamond,[2] polyfluorocarbon,[3] and poly-para-xylylene[4] and its co-monomers.[5,6]

This thesis will examine the PyCVD of two types of materials. First, issues in diamond hot-filament CVD (HFCVD) will be addressed. The body of literature on diamond CVD has grown considerably since the work of Matsumoto.[2] Generally speaking, diamond CVD systems typically have in common low pressure operation with a gas composition of 99% H_2 and 1% of a carbon containing gas such as CH_4 and some form of remote energetic gas activation. The key technological issues in diamond CVD are the deposition of a single-crystal, large area thin film and for bulk application, increased growth rates.

A large area, single-crystal film would allow us to realize some of the exceptional properties of natural diamond such as high thermal conductivity (20 W cm^{-1} K^{-1}), extreme hardness (10^4 kg mm^{-2}), good resistivity (10^{14} Ω cm), and a wide bandgap (5.45 eV). The

problem lies with the difficulty in growing heteroepitaxially on non-diamond substrates due to strain in the films from lattice and thermal expansion coefficient mismatches.[7] Chapter 3 deals with an attempt to address this problem by nucleating diamond on carbon seeds diffused into zeolite channels. Based on work on mosaic films that were nucleated on sub-millimeter scale arrays of natural diamond seeds, it was postulated that nucleation on a much smaller scale would generate contiguous, single-crystal films much faster.

The problem of low growth rates can be approached by attempting to understand the underlying chemistry and physics behind the diamond CVD process. Generally, any CVD process can be broken down into homogeneous gas phase physics, gas phase chemistry, transport, and surface reactions.

In HFCVD, there are no gas phase physical processes as in plasma deposition systems but there is the added complication of heterogeneous reactions at the hot-filament. Studies on tungsten filaments have shown that they are effective in the catalytic dissociation of molecular hydrogen[8,9] and that in diamond CVD systems, they interact with the carbon in the gas phase to form carbide.[10] Work on tantalum filaments using selective ^{13}C isotopic labeling have also shown that there is significant heterogeneous exchange at the carburized filament surface.[11]

The gas phase chemistry can be approached by borrowing from the extensive combustion literature.[12] A highly detailed kinetic study with an 89 reaction, 39 species reaction mechanism has been proposed by Frenklach and Wang.[13] While such an approach is interesting because it is capable of capturing almost all of the chemistry going on, it may be more useful to examine a subset of the larger mechanism. Wolden *et al.* have used a

brute force sensitivity analysis to do just that, reducing the mechanism down to 6 key reaction and 6 species.[14]

Measurements of the concentration of the main gas phase species have been made. Hsu has used molecular beam mass spectrometry to determine the concentrations of H, H_2, CH_3, CH_4, and C_2H_2.[15] Chen *et al.* have made non-intrusive *in-situ* measurements of gas phase H-atom concentrations in a HFCVD system by coherent anti-Stokes Raman scattering.[16] Using an optical technique with third harmonic generation, Connell *et al.* have made similar measurements of absolute H-atom concentrations. In both cases, they concluded that the H profiles could be explained by the coupled gas phase diffusion and loss at the growing diamond surface.[17]

Additional work on the importance of transport in diamond CVD has usually been done through modeling. In hot-filament and microwave systems, convective flow is typically very slow relative to diffusion ($Pe_{H2} \sim 10^{-3}$) and large diffusion boundary layers develop.[18] In high flow systems such as dc-arc jet reactors, a thinner momentum boundary layer develops near the surface and diffusion is again important.[19] Because many of the gas phase reactions are driven by atomic hydrogen, transport limitations on the H-atom concentration directly affects the gas chemistry.[20]

Finally, the surface reactions are what ultimately determine how carbon is incorporated into the diamond lattice. The role of hydrogen atoms has been fairly well studied and it is generally agreed that at the surface, H-atoms act to abstract H_2 to activate sites for carbon addition, to stabilize surface sp^3 carbon, and to etch sp^2 carbon. [20,21,22] Work using time-of-flight ion scatter and recoil spectroscopy[23] and photionization mass spectrometry[24] have measured the surface kinetics for H-atom adsorption, desorption, and

abstraction. The actual mechanism for carbon incorporation has not been conclusively determined. A number of proposals have been put forward including growth by methyl addition[22,25] and acetylene addition.[26] The general consensus seems to be that the methyl addition reaction best explains the experimental results.[27,28] The diamond surface itself has been modeled by structures as large as a 330 atom C lattice[29] to a model 9-carbon hydrocarbon[22] to a simple C^* site.[20]

One of the issues which has not been clearly resolved in the discussion of surface kinetics, however, is which, if any, of the many surface reactions is rate limiting. Does the abstraction of hydrogen from the surface to create reactive sites limit the growth rate or is it the actual carbon incorporation kinetics? In addition, while transport effects are acknowledged to have an impact on the H-atom concentration profile, does this limitation ultimately control the growth rate or do the surface kinetics?

In modeling the growth of diamond in a dc-arc plasma-jet reactor using the full transport equations and including gas-phase and surface chemistry, Coltrin and Dandy concluded that high growth rates can be achieved even without the presence of CH_3 and that the rate of diamond growth is governed by either gas-phase or surface kinetic limitations, not mass-transfer limitations.[30] They argued that if mass transfer were limiting, growth rates in plasma-gun reactors would be over 10^4 times greater than in HFVCD or microwave reactors. Using a considerably less computationally intense approach, Butler and Woodin have proposed a model which shows that the growth of adsorbed hydrocarbons into the lattice depends on the atomic hydrogen flux (which is transport limited) and that diamond growth is limited by hydrogen abstraction at low temperatures.[20]

By analyzing the spatial variance in deposition rate on a selectively nucleated wafer deposited in a HFCVD diamond reactor, we propose to show that the growth rate is transport limited as implied by Butler and Woodin and that this limitation can be explained by a hydrogen transport / surface reaction model. We also will argue that the kinetic rate constant that is calculated from the model does not correspond to a methyl addition reaction as the growth limiting step.

Chapter 4 discusses a new method for selectively depositing diamond films on silicon wafers with micron scale resolution and excellent selectivity. Chapter 5 presents an analysis of the HFCVD of these selectively deposited diamond films using a simple diffusion / reaction model. In addition to explaining the experimentally observed variations in growth rate, the model also attempts to shed light on the importance of hydrogen atoms in the growth kinetics of diamond.

The second part of this thesis deals with a completely new PyCVD process to deposit solid thin films of polydimethylsiloxane (PDMS, a.k.a. silicone) with a hot-filament system. Up to this point, only plasma polymerized (PP) PDMS films using tetramethyldisiloxane,[31] hexamethyldisiloxane (HMDSO),[32] hexamethylcyclotrisiloxane (D_3), or octamethylcyclotetrasiloxane (D_4)[33,34,35] as a feed gas have been reported. Typical maximum growth rates from the literature for the plasma polymerization of HMDSO range from 0.5 to 2.6 $\mu g\ cm^{-2}\ s^{-1}$ depending on the plasma polymerization method.[36,37]

Due to the large amount of literature on PP organosilicon compounds in general, there has been a considerable amount of work published on the characterization of this class of thin films. Techniques used include infrared absorption spectroscopy,[33,34,38] Auger electron spectroscopy, [39] x-ray photoelectron spectroscopy,[34,35] solid state nuclear

magnetic resonance spectroscopy,[34,35,40] thermogravimetric analysis,[41] scanning electron microscopy,[42] and elemental analysis.[32]

For the r.f. PP thin film of D_4, Rau and Kulisch have concluded based on IR spectroscopy that the most significant differences between the monomer and the polymer film was the splitting of the asymmetric Si-O-Si stretching peak, which they attributed to longer siloxane chains and greater polysiloxane rings, and the reduced carbon content in the film, which was deduced from the reduction in the intensity of the CH_2 and CH_3 stretching peaks.[33] They also observed the presence of a small Si-H peak. Tajima and Yamamoto have also characterized r.f. PP thin films of D_4 by IR spectroscopy but did not observe any Si-H. Using ^{29}Si-NMR, they observed three signals which they assigned to $(CH_3)_3Si$-O-, -O-$(CH_3)_2Si$-O-, and CH_3Si(O-)$_3$.[34] Sakata *et al.* employed XPS to analyze PP films of D_4 and came to the conclusion that 97% of the silicon was still in the +2 oxidation state as in the starting monomer.

Because only plasma polymerized silicone films have been reported so far, it has been speculated that an electron impact initiated mechanism is responsible for film deposition.[33] However, electron impact and UV photolysis events are clearly rare in a pyrolytic system so another mechanism must be responsible for growth.

Chapter 6 discusses the details of the HFCVD silicone process and the materials characterization analyses. Chapter 7 presents the results from applying a version of the diamond HFCVD diffusion / reaction model to try to understand the relative role of transport and surface kinetics. Possible mechanisms for the PDMS PyCVD process are discussed in the light of the results in Chapters 6 and 7.

In the following two sections, a more extensive review of the literature on diamond and silicone CVD will be presented with an emphasis on material relevant to this work.

1.1 Review of diamond thin film CVD

1.1.1 History

The first person to produce synthetic diamonds via any method was Eversole, who in 1952, achieved growth on diamonds seeds with a carbon monoxide / hydrocarbon mixture at moderate pressures.[43]

This work, however, was overshadowed by the discovery of a high pressure / high temperature (HPHT) process at Allemanna Svenska Elektriska Aktiebolaget (ASEA) in Sweden in 1953 and, independently, at General Electric in 1955.[44,45] HPHT synthesis involves the conversion of non-diamond carbon to diamond at pressures and temperatures where diamond is the thermodynamically stable phase; i.e., over 50 kbar and 2000 °C.

Serious study of the chemical vapor deposition (CVD) of metastable diamond from the gas phase began in the late 1950's with work from Deryagin's group in the USSR.[46] They synthesized diamond through the thermal decomposition of CBr_4 and CCl_4 as well as hydrocarbon / hydrogen mixtures. In the U.S., Angus and coworkers followed a similar approach in the late 1960's and demonstrated the growth of boron doped p-type semiconducting diamond.[47,48] However, because of the extremely slow growth rate of the CVD method of diamond synthesis (<0.1 μm/hr) as compared to the HPHT method (~1000 μm/hr), little attention was devoted to the field until the late 1970's when growth rates of up to 5 μm/hr were reported by Russian researchers, notably Deryagin and Spitsyn.[49,50] These reports were closely followed in 1982-83 by a series of papers by researchers at the

National Institute for Research in Inorganic Materials (NIRIM) in Japan in which they reported the growth of diamond films in an open flow system at several microns per hour using methane in an excess of hydrogen.[2,51] Since that time, the field has exploded, yielding several hundred new papers a year.

1.1.2 Chemical vapor deposition techniques

At present, there are more than ten different methods for the chemical vapor deposition of diamond. The hot filament method of diamond CVD (HFCVD) was the earliest used and consists of a steady state flow reactor in which the gas mixture is passed over a resistively heated filament made of a refractory metal such as tungsten, tantalum, molybdenum, or rhenium. (See Figure 1-1) The filament can be straight or formed into any number of coiled or planar shapes with the shape affecting the uniformity of the deposit.[52,53] Filament temperatures are typically 2500 K. Growth rates for this method are approximately 1 μm/hr.

Plasma reactors have also been used extensively to deposit diamond films, with microwave generated plasmas (MPCVD) being the most common because they are more efficient than r.f. plasmas for the dissociation of H_2 and because the absence of an electrode minimizes the codeposition of metal contaminants. Schematically, a basic microwave reactor consists of a quartz tube placed in a microwave cavity and a magnetic waveguide to contain the plasma.[54] Alternative methods include r.f induced[55,56] and DC discharge plasmas.[57,58] Growth rates for these methods are in the 10 μm/hr range.

Although the HFCVD and MPCVD methods differ greatly in specifics, they have in common the high energy activation of a hydrocarbon / hydrogen mixture in the gas phase

followed by transport to a growing surface. The gas phase composition is typically < 2% of a carbon source gas in hydrogen; additional gases such as oxygen, oxygen-containing hydrocarbons (e.g. acetone,[59,60] methanol,[61] ethanol[62]), halogenated hydrocarbons,[63] and noble gases have also been added. In order to formalize this commonality among different deposition systems, Bachmann, *et al.* have compiled gas composition data from the literature for a variety of systems to arrive at an empirical C-H-O ternary phase diagram[64] (Figure 1-2). The main item to note is the narrow "diamond growth domain" about the CO/H line in the center of the diagram. In carbon-rich environments, non-diamond phases of carbon are kinetically favored and deposit preferentially over diamond. In oxygen-rich environments, etching by atomic H and O leads to no net growth.

The other two important operating parameters are the system pressure and the substrate temperature. The former can range anywhere from 0.5 torr on up to atmospheric with typical operations in the 10-100 torr range. If the system pressure is too low or too high, only amorphous or graphitic carbon can be deposited; however the optimal operating range seems to vary considerably from reactor to reactor. The effective gas phase temperature at the point of activation will vary depending on the activation method but will generally be from 2000 K to over 2800 K while the substrate temperature will usually range from 900 K to 1300 K. At substrate temperatures above 1600 K, only graphitic deposits have been observed[64] while growth at temperatures as low as 403 K have been reported in $CO/O_2/H_2$ microwave plasmas.[65]

Significantly higher growth rates on the order of 100 μm/hr have been achieved with combustion and DC plasma jets. Compared to HFCVD and MPCVD reactors, these systems are characterized by higher gas temperatures (3500 K - 6000 K), flow rates

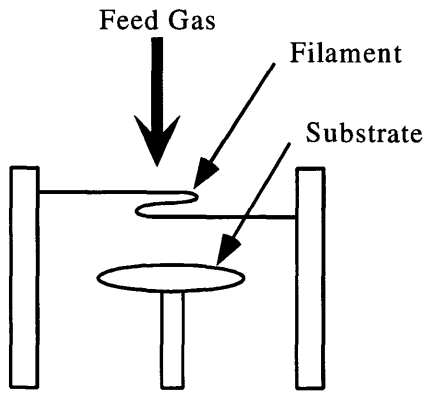

Figure 1-1: Diamond hot-filament CVD reactor schematic

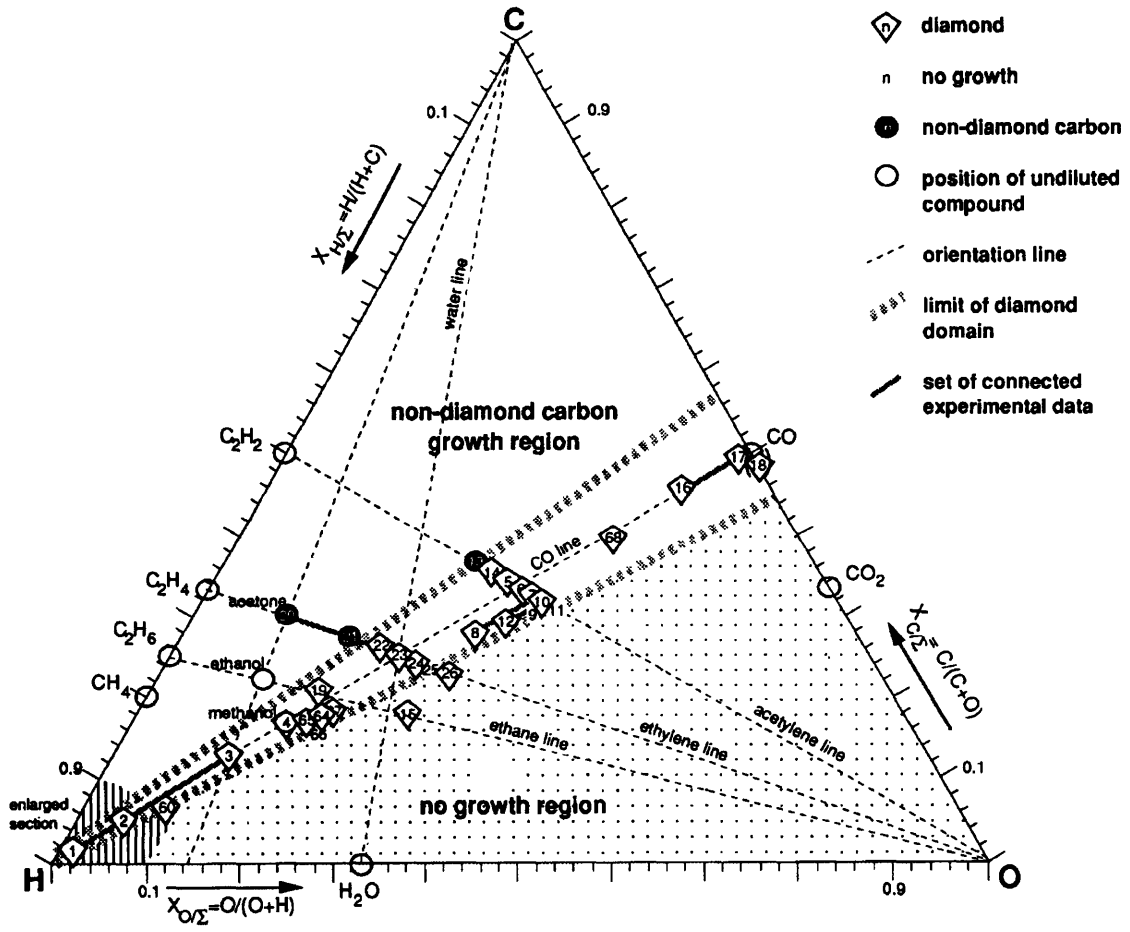

Figure 1-2: Atomic C-H-O diamond deposition phase diagram

From P. K. Bachmann, D. Leers, and H. Lydtin, *Diamond Relat. Mater.*, **1**, 1-12 (1991).

(10 l/min vs. 0.5 l/min), and operating pressures (300 - 760 torr). Initially, combustion systems were conventional oxyacetylene torches operated at slightly fuel rich conditions (R = $\frac{C_2H_2}{O_2}$ = 1.1).[66] Films from these system were non-uniform and occured in annular regions corresponding to the different flame zones.[66,67] Flat-flame burners, however, have achieved large area uniformity at both atmospheric[68,69] and reduced pressures.[70,71] Plasma jets are basically rapidly quenched DC plasmas and do not appear to suffer from the non-uniformities of early combustion systems.[72] Schematics of each method are shown in Figures 1-3 and 1-4.

The highest growth rates reported to date have been with DC or RF arc discharge plasma jet reactors in which a supersonic jet of gas is passed through a DC arc discharge plasma and impinged upon a cooled substrate. A typical system is shown in Figure 1-5; growth rates reportedly approach 1000 μm/hr.[73]

1.1.3 Substrate effects on nucleation and film growth

Diamond films have been deposited on a variety of substrates, but most commonly, doped single-crystal silicon wafers are used because they are stable in the high temperature diamond growth environment as well as being relatively inexpensive and readily available. On clean, mirror-polished Si wafers, diamond particles nucleate at a density of 10^3 cm^{-2}. In order to enhance the nucleation rate and reduce the induction time to growth, wafers are typically either scratched or seeded with diamond powder.[74] Any number of hard materials (e.g. diamond, Al_2O_3, SiC, BN) can be used to scratch the surface and introduce nucleation sites but diamond has the most pronounced effect, increasing the nucleation density to 10^8 - 10^9 cm^{-2}. While there is some evidence that sharp features enhance nucleation,[75,76]

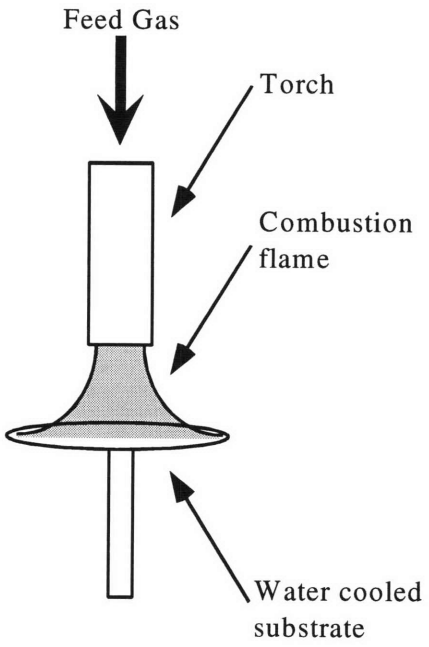

Figure 1-3: Diamond combustion reactor schematic

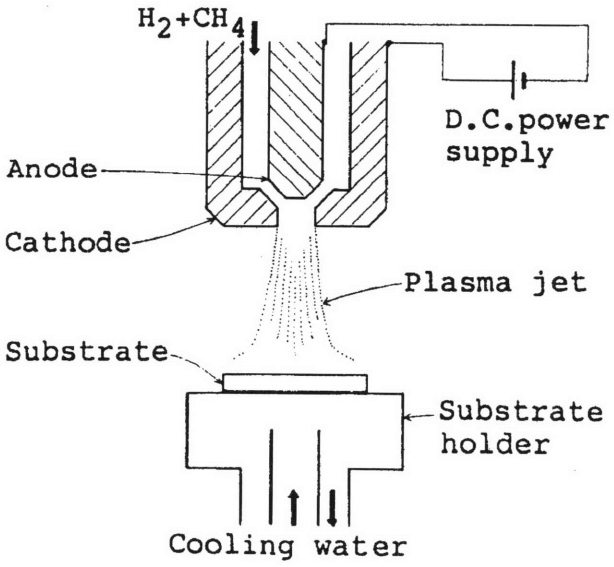

Figure 1-4: Diamond plasma jet reactor schematic

From K. Kurihara, K. Sasaki, M. Kawarada, and N. Koshino, *Appl. Phys. Lett.*, **52** (6), 437-438 (1988).

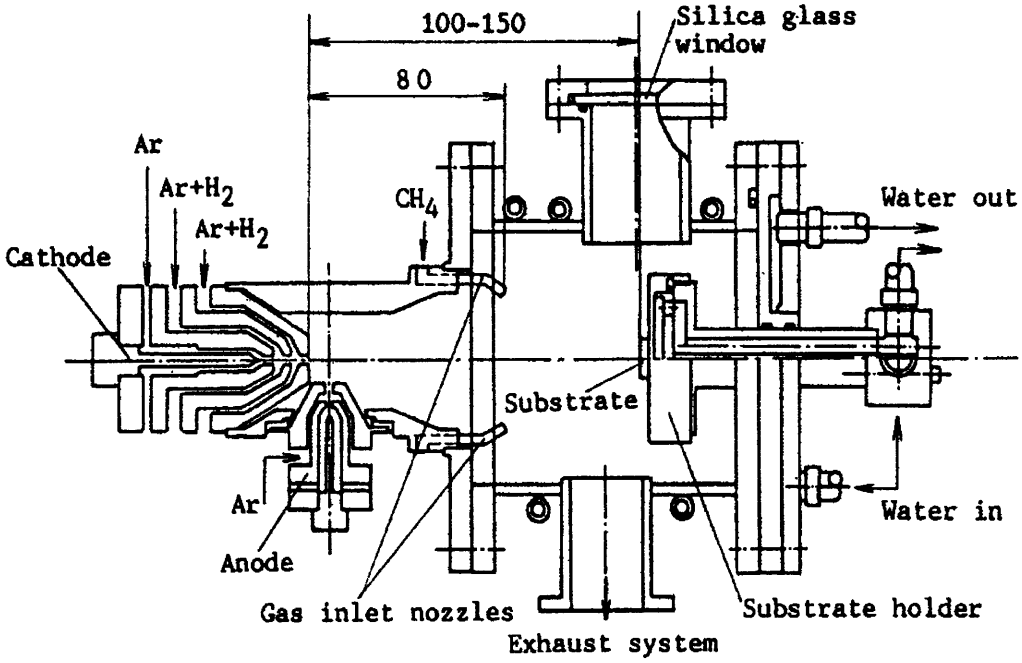

Figure 1-5: Diamond dc arcjet schematic

From N. Ohtake, and M. Yoshikawa, *J. Electrochem. Soc.*, **137** (2), 717-722 (1990).

possibly by lowering the critical free energy for nucleation, it is generally agreed that the imbedding of sub-micron diamond particles is primarily responsible for the greatly enhanced nucleation on diamond scratched substrates.[77,78]

Enhanced nucleation has also been observed on otherwise untreated surfaces via the introduction of a carbon source at or near the growth surface. Rudder, *et al.* observed that the placement of micron-sized graphite fibers on otherwise clean substrates such as silicon, nickel, fused silica, and crystalline quartz led to diamond deposits that mimic the position of the graphite fibers.[79] They speculated that the graphite fibers were altering the local gas phase chemistry at the substrate surface. In a related experiment, Barnes and Wu deposited an amorphous carbon film onto a diamond scratch silicon wafer and observed an increase in the nucleation density to $3x10^{10}$ cm^{-2} from $2x10^{6}$ cm^{-2} for an uncoated, scratched wafer.[80] In this case, they speculated that nucleation enhancement was via the introduction of more carbonaceous sites. Similarly, by subliming a thin layer of C_{70} buckyballs onto a silicon substrate and pretreating it in a relatively carbon rich microwave discharge (CH_4:H_2 / 1:5) under negative bias, Meilunas and Chang also observed vastly improved nucleation.[81] In this case, it is also unclear whether nucleation occured directly on the C_{70} molecules or whether they were simply providing an added carbon source similar to the graphite fibers. On the other hand, Pehrsson and Morrish have reported that they did <u>not</u> observe increased nucleation on a variety of substrates coated with a hydrocarbon-based oil.[82] Instead, they noticed that, for oil coated samples, the induction time to reach the maximum nucleation density was considerably less than that for the uncoated samples. They hypothesized that the reduced induction time resulted from a saturation of the growing surface which led to more carbon being available for growth. Taken together,

these reports indicate that diamond nucleation can be enhanced by relatively stable carbon source at the surface while "transient" carbon sources can at best accelerate the nucleation process but not add to the ultimate nucleation density.

Whether grown on seeded, scratched, or carbon coated substrates, CVD diamond films deposited on non-diamond materials are inevitably polycrystalline with grains 1-30 μm in size, depending on the initial nucleation density and film thickness. The only sure way to grow a smooth, single-crystal film is through homoepitaxy on a diamond substrate but even that is nontrivial. Chu, *et al.* have shown that growth on the (100) face of diamond produces a smooth, stress-free film while (111) and (110) films exhibited graphitic inclusions and cracked spontaneously to relieve stress.[83] Building upon the idea that the ideal substrate for diamond growth is diamond, Posthill and coworkers have developed a tiling process by which smaller natural diamonds were bonded together to form a larger single crystal substrate for homoepitaxial growth.[84] In order to reuse this tiled substrate, they demonstrated a liftoff process by which they could remove a free-standing CVD diamond film that had been deposited on the tiled diamond substrate by graphitizing and etching away a previously implanted carbon layer.[85] However, since it is still impractical and fairly difficult to grow a large area film on a new diamond substrate each time, there has also been considerable effort focused on the epitaxy of diamond on non-diamond substrates. The majority of work has centered on studying materials with the face centered cubic (fcc) structure and an interatomic spacing close to that of diamond, 3.567Å. Table 1-1 lists several materials that have been tried, their lattice parameter, and percent mismatch relative to diamond.

Cubic boron nitride (c-BN) is extremely similar to diamond. Its crystal structure is composed of interpenetrating fcc lattices of B and N instead of two C lattices as in diamond. Yoshikawa, *et al.* grew a 0.1 μm thick diamond film on the (111) surface of c-BN. By using micro-Raman spectroscopy, they showed via the frequency shift of the characteristic diamond peak from 1332 cm^{-1} to 1325 cm^{-1} that there was a 1.8% strain in the film.[7] This compares to the 1.4% mismatch between the diamond and c-BN lattices. Using reflection high-energy electron diffraction (RHEED), Koizumi, *et al.* provided further evidence that true heteroepitaxy of diamond on c-BN had been achieved.[86] However, because large sized c-BN crystals are synthesized from hexagonal boron nitride in a HPHT process nearly identical to that used for HPHT diamond synthesis, it is likewise very difficult to generate large crystals of this substrate, and little additional progress has been made.

In spite of having the lowest lattice mismatch, epitaxial growth on nickel (Ni) has yet to be proved. In a series of *in situ* experiments, Belton and Schmieg used surface analysis and diffraction techniques to show that deposition on the Ni (100) surface

Table 1-1: Comparison of lattice parameters of several diamond heteroepitaxy candidates and their relative % mismatch

Substrate Material	Lattice parameter	% Mismatch
cubic boron nitride (c-BN)	3.616 Å	1.4 %
nickel (Ni)	3.524 Å	-1.2 %
copper (Cu)	3.6148 Å	1.3 %
beta silicon carbide (ß-SiC)	4.36 Å	22 %

proceeds by the interstitial diffusion of C followed by the development of graphitic and glassy carbon layers.[87] Unsurprisingly, subsequent diamond growth over these poorly oriented films was not in registry with the underlying Ni surface. On the other hand, Sato *et al.* claim to have grown individual diamond crystals epitaxially on nickel.[88] However, since they did not give their experimental details or the details of the x-ray analysis upon which they based their claim, it is still not clear if growth is possible. Recently Yang, *et al.* reported the growth of <100> and <111> oriented diamond nuclei on diamond scratched Ni substrates using a multi-step anneal and HFCVD deposition process.[89] In a following paper, they further reported that the oriented diamond grains appeared to grow together without clear grain boundaries.[90] However, the degree of orientation was not measured via diffraction nor was heteroepitaxy confirmed through cross-section transmission electron microscopy thereby making quantitative evaluation impossible. In addition, consistent orientation of only about 85% of the nuclei was achieved. A much higher degree of alignment would be necessary to achieve the thermal and electronic properties of single crystal diamond.

Copper is an interesting substrate for diamond deposition because, in addition to having a close lattice match, it does not react with carbon to form a carbide as nickel does. To date there have been two closely related ion implantation techniques reported for the production of diamond films on copper. Prins and Gaigher used what they termed "implanted-atom-outdiffusion-epitaxy" (IAOE) to grow their films.[91] Basically, their technique involved implanting C ions at 120 keV and a dose of 5×10^{17} cm^{-2} into a crystalline copper substrate heated to 900 °C. By floating films onto TEM grids, Prins obtained electron diffraction patterns which he interpreted to be indicative of diamond.

However S.-Tong Lee and coworkers were not only unable to reproduce Prins' results but showed through a thorough and careful analysis that the films were highly oriented crystalline graphite.[92] They also demonstrated that unless extreme care was exercised when using diffraction patterns to differentiate between polycrystalline diamond and polycrystalline graphite, misidentification can occur. Recently Hoff and others, in collaboration with Prins, succeeded in reproducing the original Prins and Gaiger result.[93] Analysis via micro-Raman spectroscopy and electron diffraction clearly indicated a stressed diamond film but the result was by no means reproducible. Only three films of twenty-five showed traces of diamond.

Using a similar method, Narayan, *et al.* have also reported diamond growth on copper.[94] But instead of a high temperature implantation, they implanted C atoms with energies in the 60-120 keV range to doses of 1.0×10^{18} - 2.0×10^{18} cm^{-2} at room temperature. The as-implanted specimens were then laser annealed with nanosecond excimer laser pulses to rapidly melt and resolidify the implanted regions. The films were thoroughly characterized through scanning electron microscopy, x-ray diffraction, Rutherford backscattering/ion channeling, and Auger and Raman spectroscopies. However, two separate attempts to reproduce this result by workers at Eastman Kodak Corporate Research Laboratories[95] and at Oak Ridge National Laboratory[96] were unsuccessful.

Because of the lack of clear successes with heteroepitaxy on closely lattice matched substrate, alternate approaches employing mosaic and oriented, textured films have been pursued. Mosaic and textured films are polycrystalline films that have almost all of their

grains aligned in a preferred orientation. These films all exhibit low angle grain boundaries of 0.2 - 5% due to tilt and azimuthal misorientations.[97,98] (See Figure 1-6.)

Using an approach that has been termed "artifical epitaxy"[99] and standard photolithographic patterning techniques, Geis and coworkers have developed a method for producing mosiac films. They etched a square array of 90 μm x 90 μm inverted pyramidal pits with their centers 100 μm apart into a (100) Si substrate and then seeded these pits with 75-100 μm sized, (111) faceted diamond crystals. Figure 1-7 schematically details the process. Subsequent growth on these seeded substrates under conditions which favor (100) faceted growth produced coalescent films with only low angle grain boundaries. Geis *et al.* have also demonstrated another mosaic process in which a continuous homoepitaxial film is grown on a layer of smaller (250 μm on a side), oriented diamond cubes.[100] In a related paper, Pryor, *et al.* reported that the performance of diodes created with mosaic films approached those made from single-crystal films while polycrystalline diamond diodes consistently shorted.[101]

Most recently, Spitzl, *et al.* reported the deposition of micron thick diamond films on porous silicon substrates of varying porosity.[102,103] Depending on the etching conditions used and the doping of the substrate, the randomly distributed features on porous silicon can have an interpore spacing of anywhere from 5 nm to 200 nm.

According to Wild *et al.*, (100) textured films can be produced from randomly oriented nuclei once the film is made sufficiently thick.[104] Modeling showed that the film thickness required to generate well-textured films depends on the initial spacing of the nuclei; closely spaced nuclei allow the formation of a textured film at smaller film thicknesses than do widely spaced nuclei.[105] When compared with the mosaic film

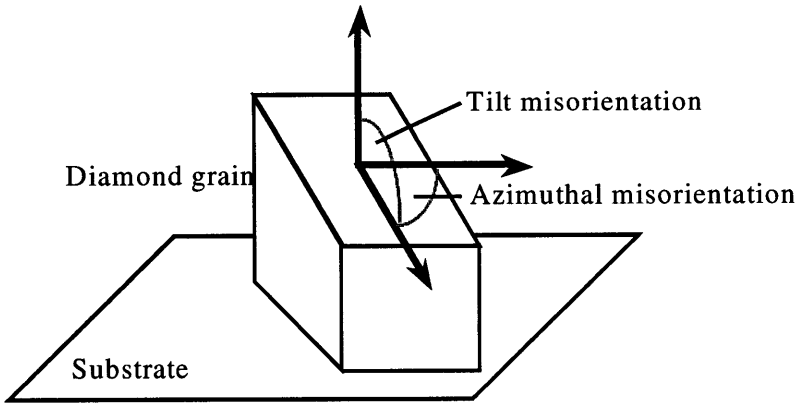

Figure 1-6: Definition of *tilt* and *azimuthal* misorientations.

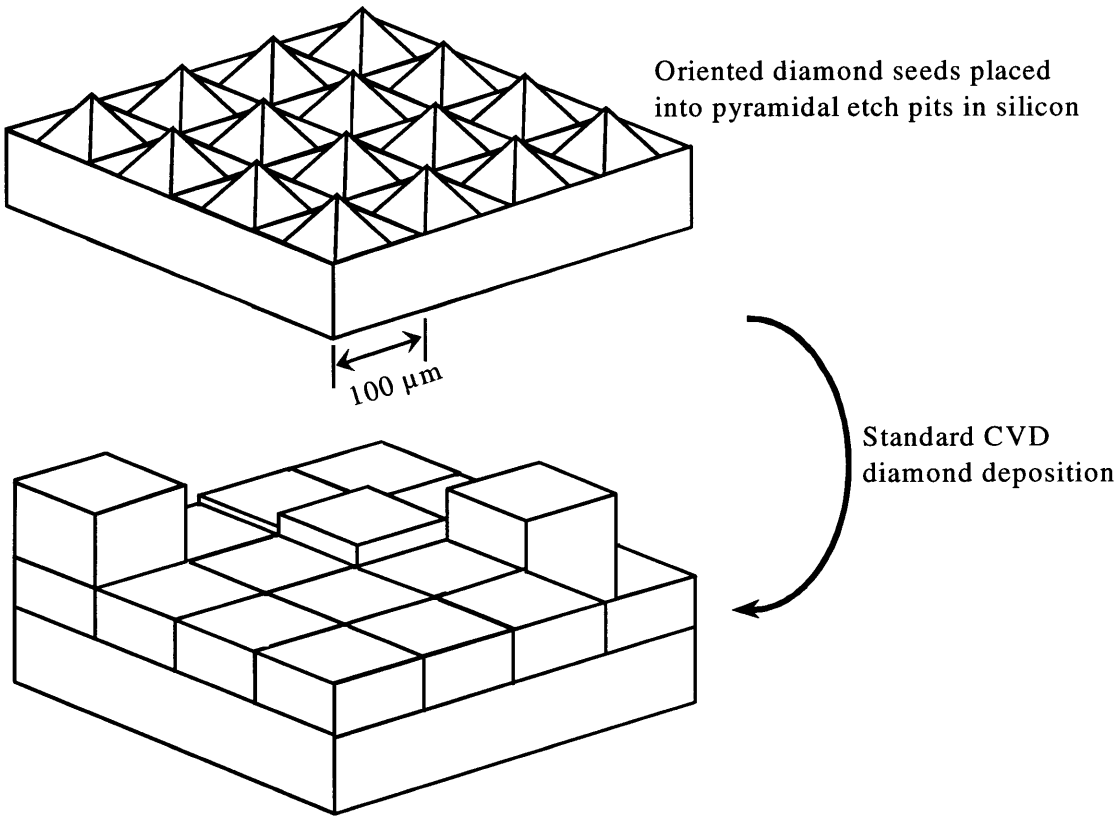

Figure 1-7: Diamond mosaic film deposition

technique, growth on porous silicon represents a three orders of magnitude decrease in the spacing of the nucleation centers. Therefore it is expected that films grown on porous silicon would require considerably less time to achieve a well-formed morphology than those grown on lithographically defined substrates.

Workers at North Carolina State University have taken yet another approach using ß-silicon carbide (ß-SiC) as a substrate. Despite having a large lattice mismatch with diamond (22%), it is speculated that epitaxy is possible[106] since ß-SiC grows epitaxially on Si despite a 24% lattice mismatch.[107,108] Indeed, Stoner, *et al.* have produced a (100) textured diamond film on (100) Si[109] using a multi-step process involving epitaxial ß-SiC growth on Si, followed by DC bias-enhanced nucleation, and finally microwave plasma deposition with deposition parameters that favor (100) oriented grain growth. While this film still possesses low angle grain boundaries, nearly 100% of the grains are epitaxially oriented with respect to the substrate. Furthermore, since it has been demonstrated that the smoothness of a textured film improves with film thickness due to the dominance of the fastest growing face parallel to the substrate surface,[104] they have also postulated that any minor tilt misorientation will be overgrown. While this phenomenon will not eliminate any azimuthal misorientations, it is noted that azimuthal misorientations due to a misfit dislocation will likely be tilt misoriented as well so that further growth should also eliminate these defects.[109]

1.1.4 Nucleation and growth processes

Figure 1-8 schematically outlines the separate physical and chemical processes which are involved in diamond nucleation and growth regardless of the deposition method.

First, reactive species are generated by a highly energetic activation process which may involve heterogeneous chemistry on a hot filament,[9,11] combustion chemistry in a flame,[13,110] or radical chemistry in a plasma.[111] Species which have been considered as possible growth precursors include CH_3, C_2H_2, CH, CH_2, C, C_2, C_2H, and CO.

Next, transport of the activated species to the surface occurs primarily via diffusion through a stagnant boundary layer. The mass Peclet number is on the order of 10^{-2} - 10^{-3}, indicating that for mass transport, diffusion dominates over convection. Experimentally, it has been observed by Everson & Tamor[112] and Molinari, *et al.*[113] that the average crystal size of well separated diamond nuclei correlate with their number density, with smaller crystals in the regions of higher nucleation. Molinari, *et al.* have advanced the explanation that this coupling of average crystal size and nucleation density is due to differences in the rate of H-radical recombination on diamond and on silicon. By assuming that the diamond surface is a more efficient H-atom recombination catalyst and that the system pressure is high enough such that gas phase diffusion normal to the substrate is slow relative to H-atom surface recombination, they then argue that densely nucleated substrates would be subject to a lower local H-atom concentration than sparsely nucleated ones because they have a higher fractional surface coverage of diamond. By further assuming that the sequence

$$C_{diamond}\text{-}H + H\bullet \longrightarrow C_{diamond}\bullet + H_2$$

$$C_{diamond}\bullet + CH_3\bullet \longrightarrow C_{diamond}\text{-}CH_3$$

dominated the growth process, they concluded that this diffusion-limited variation in H-atom concentration was the basis for the observed coupled behavior. However,

experiments at a lower pressure where gas phase diffusion is faster did not produce noticeably different results.

Reactive species may then adsorb onto, desorb from, or recombine on the surface. In the earliest stages of growth, the adsorbed species may also react with the substrate surface e.g., forming a carbide on Si and W substrates before becoming available for nucleation. However, the precise details of this initial process and the exact nature of the nucleation site are not well known. There is evidence to support growth on nanometer sized diamond particles embedded in the polishing process[77,78] but this does not explain the non-zero nucleation observed on untreated silicon substrates. In light of the *in-situ* surface analysis work of Belton, *et al.* in which they identified a clear SiC surface layer after 15 minutes of growth before any diamond could be detected[114] and the work on growth on ß-SiC by Stoner, Glass, Zhu, and others at North Carolina State,[98,106] one could speculate that the surface carburization reaction on a clean Si wafer leads to small, isolated areas of crystalline ß-SiC that nucleate diamond in a mixture of other SiC phases that do not. Another, more classic, approach would be based on the clustering of diamond growth precursors until a "critical cluster size" was exceeded and a stable nuclei was then formed.

In addition to the nucleation problem, there is the question of how growth proceeds after nucleation. To date, all of the proposed detailed growth mechanisms have been based on the addition of a methyl radical[22,115] or an acetylene molecule[26,116,117] to a hydrogen terminated surface. Tsuda, *et al.* have proposed a mechanism in which all of the terminated hydrogens on a (111) surface are first replaced by methyl groups through either the direct addition of methylene or a hydrogen abstraction followed by a methyl radical addition[115]. Using semi-empirical quantum calculations, they found that three neighboring

methyl groups could spontaneously form a diamond structure via a methyl cation intermediate. However, Anderson, *et al.* have calculated that while a single methyl binds readily with an energy of 3.07 eV, a second methyl only binds weakly with an energy of 0.87 eV while further methyl additions are energetically unfavored.[118] In addition to the energetically disallowed generation of a methyl covered surface, the presence of a methyl cation in a hot-filament or combustion reactor is also highly improbable.

The earliest mechanism involving acetylene as a growth species was proposed by Frenklach and Spear and consisted of surface activation through the abstraction of a hydrogen atom from a surface carbon followed by the addition of an acetylene or "acetylenic" molecule such as C_2H, C_2H_3, or C_4H_2.[26] Acetylene was proposed because of its abundance in high temperature processes such as hydrocarbon pyrolysis,[119,120] combustion,[110] and plasmas[111] and because of its importance in the formation of high molecular weight hydrocarbons and eventually solid carbon in sooting flames.[121,122] Frenklach has also proposed that the kinetics of the gas-diamond surface reactions can be estimated form similar gas-phase reactions.[13,21] This method has been used successfully to estimate the gas phase kinetics of high molecular weight alkanes.[12,123]

Harris has suggested a mechanism in which a small portion of the diamond (100) surface is modeled by a bicyclo[3,3,1]nonane molecule.[22] Growth is hypothesized to proceed by methyl addition after a hydrogen abstraction ($HH \rightarrow H^* \rightarrow HM^*$ in Figure 1-9). Subsequent hydrogen abstractions from the methyl group and the neighboring lattice site then result in incorporation into the diamond lattice.

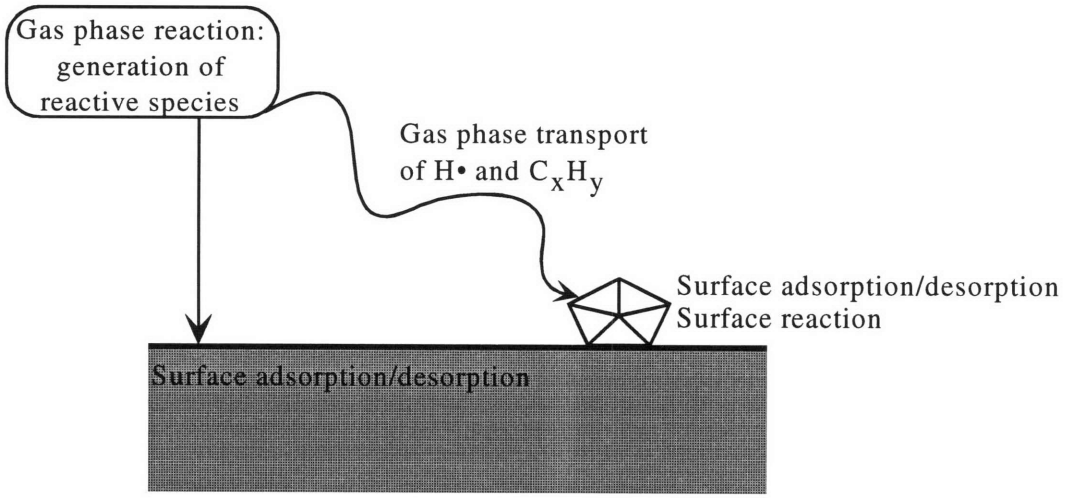

Figure 1-8: Description of physical process in pyrolytic CVD

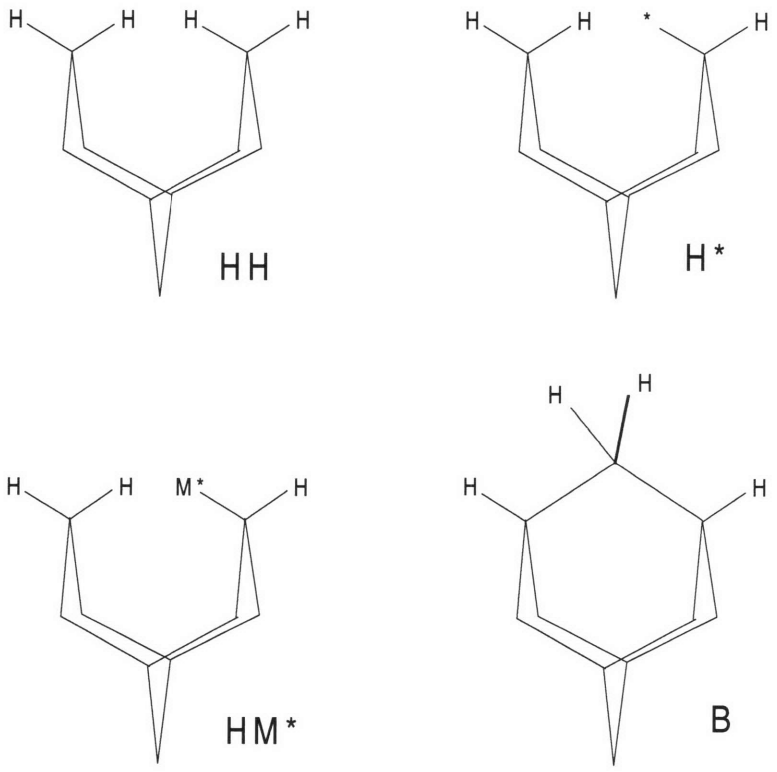

Figure 1-9: Atomistic model for H_2 abstraction from the diamond (100) surface (Harris, 1990)

Adapted from S. J. Harris, *J. Appl. Phys.*, **56**, 2298 (1990).

1.2 Review of silicone thin film CVD

The term silicone generally refers to the class of organosilicon monomers and polymers that contain Si-C bonds. In a more restrictive sense, it has also been used to refer to organosilicon polymers in which the Si atoms are bonded through oxygen atoms; i.e., 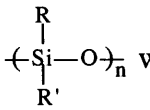 where R and R' are organic groups. A more precise term for these compounds would be polyorganosiloxanes; for the case where R and R' are $-CH_3$, the polymerized compound is referred to as polydimethylsiloxane (PDMS). In the following review, the term silicones and polyorganosiloxanes will be used interchangeably.

1.2.1 Thin film chemical vapor deposition processes

To date, all attempts to deposit thin films of silicone have focused on plasma polymerization of various monomers. An extensive review of such work has been conducted by Wróbel and Wertheimer.[124] For the most part, the plasma processes used to deposit these films were fairly conventional, ranging from audio and radio frequency capacitively coupled discharges to microwave discharges. A slight twist was introduced by Rau and Kulisch who investigated the effect of using a remote Ar or Ar/O_2 plasma source instead of the usual direct plasma to polymerize the monomer gas.[33] The most notable difference among these many deposition processes, aside from differences in operating parameters such as pressure, flow rate, power, substrate temperature, DC bias, and so on, was the variety of monomers used. In their review, Wróbel and Wertheimer listed 52 different monomer / monomer-gas mixtures which have been reported. The range of starting materials varied from the simplest organosilicon compound, tetramethylsilane

(TMS),[34] through the more complex basic organosiloxanes, hexamethyldisiloxane (HMDSO),[32] on up to octamethylcyclotetrasiloxane (D_4), the cyclic tetramer of the basic dimethylsiloxane building block.[33,34,35] Mixtures of organosilicon monomers and process gases such as oxygen, hydrogen, and argon have also been tried.[125,126,127] Generally, the addition of these gases serve to eliminate organic groups from the film[125,126] and in the extreme case of tetraethoxysilane and oxygen, all organic groups are removed and silicon oxide films are produced.[127]

By analyzing the gas phase composition of a plasma process with mass spectroscopy, Hays determined that, for an r.f. plasma discharge of methyltrimethoxysilane, the most abundant chemical species included C_1, C_2, and C_3 hydrocarbon fragments as well as siloxy compounds.[128] Optical emission spectroscopy on an r.f. plasma of tetramethylsilane showed the spectra lines of atomic hydrogen and CH•.[129] Wróbel and Wertheimer believe that these and other data indicate that the dominant characteristic of monomer fragmentation for methylsilicon monomers is the abstraction of the methyl groups.[124]

However, silicon NMR of PP HMDSO and D_4 films both have shown the presence of mid-chain dimethylsiloxane units plus $-O-(CH_3)Si-(O)_2-$ and $-Si(O)_4-$ crosslink units as well as $(CH_3)_3Si-O-$ terminal groups indicating that the highly energetic plasma environment fragments the monomers non-selectively, resulting in a severely scrambled gas phase composition.[32,34,40]

Rau *et al.* have concluded that direct plasma dissociation by electron impact plays a prominent role in the polymerization of HMDSO and D_4.[33] Based on their work with a remote r.f. plasma reactor, they have observed a linear dependence of growth rate with r.f.

power, with growth rates of about 50 Å/min for the reactor in remote plasma mode (P<30 W) on up to a maximum of 400 Å/min in a direct plasma.

Wróbel has further postulated a radical plasma polymerization mechanism for methylsilicon monomers based on the generation of reactive silene units ($\diagup\!\!\diagdown Si{=}CH_2$).[130] Studies of UV photolysis of methylsilicon compounds have shown that the conversion to silylmethyl groups to silene is an important step in the process.[131] The disproportionation reactions of methyl and silyl radicals, which result from the electron impact and photolysis of methylsilicon monomer molecules, may also lead to silene generation.[132] Because of the reactive, diradical nature of the silene units, it was hypothesized that they could easily propagate chain growth by reacting with other silene units or with silyl and silylmethyl radicals. An ionic mechanism by which sililene cations could react with the oxygen in a siloxane unit to lengthen the chain and to crosslink the film has also been proposed:[133]

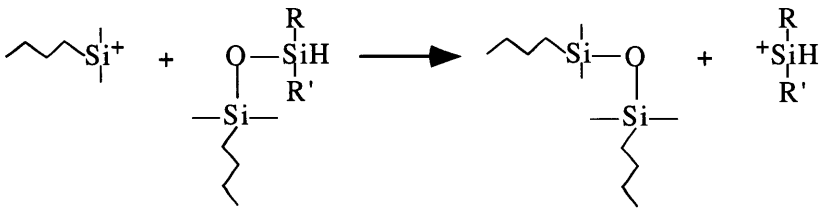

1.2.2 Applications

As a bulk material, silicones are available in many forms, ranging from low viscosity oils on up to highly crosslinked resins and rubbers. They are used in a range of everyday applications from electrical insulation to stopcock greases to bathroom caulking. In industrial applications, silicones are used as low concentration defoaming agents, paint additives, and plastic mold release agents.[134] In the field of biomedical applications, silicones are one of the most widely used and studied biomaterials. They have been widely

used as breast implants, penile implants, testicular implants, joint replacements, cerebrovascular shunts, heart valves, cardiac pacing lead insulation, indwelling catheter material, intraocular lenses, and carriers for cochlear electrodes.[135] Generally speaking, as a solid structural material silicones are one of the most biocompatible, long-term materials yet developed. The widely publicized problems with silicone breast implants appear to be due to the leaking or diffusion of the silicone gel from the inside of the implant into the body.[136] For this reason, saline filled silicone implants are considered a better alternative to the conventional gel filled ones.

Silicones also have a wide variety of real and potential applications as chemical vapor deposited thin films. In the biomedical area, they could be used as a well adherent, conformal coating on implantable devices which have complex topologies and small dimensions. Chawla has coated Celgard-2400® (microporous polypropylene) and Silastic® membranes with plasma polymerized hexamethylcyclotrisiloxane (D_3) and octamethyl-cyclotetrasiloxane (D_4) films and evaluated the samples using an *in vitro* loop[137] and an *ex vivo* shunt system with a canine model.[42,138] In both cases, the number of platelets and leukocytes adhering to the samples were microscopically determined to be less than on the untreated controls. Ishikawa *et al.* examined a number of RF plasma polymerized polyorganosiloxane monomers and found that the number of platelets adhering to coated glass slides as well as the amount of ATP released from these platelets in a human blood *in vitro* system was 10-30% less than the uncoated slides.[139]

Ozdural *et al.* have coated hemoperfusion-grade charcoal by exposure to a hexamethyldisiloxane plasma and found that coatings characterized by less than 2% weight

gain did not affect creatine adsorption from canine blood while preventing the release of charcoal particles and minimizing platelet retention.[140]

In other applications, organosilicon films have been used as protective coatings on optical devices. Plasma polymerized hexamethyldisiloxane has been used to protect Al and Ag coated front surface mirrors from abrasion and weathering.[141,142] NASA has developed and patented an anti-reflection, scratch-resistant coating from plasma polymerized vinyltrimethoxysilane.[143,144,145]

Plasma polymerized hexamethyldisiloxane and vinyltrimethylsilane films have also been shown to have potential applications in integrated optics as particle-free, low attenuation planar light guides.[146,147] In addition, it has been shown that the index of refraction can be precisely tailored by copolymerizing two monomers in varying proportions.[148]

Because silicones are generally gas permeable, Sakata and coworkers have applied plasma polymerized films from various organosilicon monomers to develop a thin, well-adherent, pinhole free permselective membranes.[35,149,150] In particular, they have deposited films on porous polypropylene substrates that display oxygen-to-nitrogen permeability ratios as high as 3.5.[35]

References

1. S. Wolf, and R. N. Tauber, *Silicon Processing for the VLSI Era*; Vol. 1: Process Technology. Lattice Press: Sunset Beach. 1986.
2. S. Matsumoto, Y. Sato, M. Tsutsumi, and N. Setaka, *J. Mater. Sci.*, **17**, 3106-3112 (1982).
3. S. J. Limb, C. B. Labelle, K. K. Gleason, D. J. Edell, and E. F. Gleason, *Appl. Phys. Lett.*, **68** (20), 2810-2812 (1996).
4. M. Szwarc, *Discuss. Faraday Soc.*, **2**, 46-49 (1947).
5. V. Sochilin, K. Mailyan, L. Aleksandrova, A. Nikolaev, A. Pebalk, and I. Kardash, *Doklady Akademii Nauk SSR*, **339** (1), 173-176 (1991).
6. J. F. Gaynor, and S. B. Desu, *J. Mater. Res.*, **9** (12), 3125-3130 (1994).
7. M. Yoshikawa, H. Ishida, A. Ishitani, T. Murakami, S. Koizumi, and T. Inuzuka, *Appl. Phys. Lett.*, **57** (5), 428-430 (1990).
8. T. W. Hickmott, *J. Chem. Phys.*, **32**, 810 (1960).
9. C. Wolden, and K. K. Gleason, *Appl. Phys. Lett.*, **62** (19), 2329-2331 (1993).
10. T. D. Moustakas, *Solid State Ionics*, **32/33**, 861-868 (1989).
11. K. M. McNamara, and K. K. Gleason, *J. Electrochem. Soc.*, **140** (2), L22-L24 (1993).
12. J. Warnatz, *Combustion Chemistry*, ed. by W. C. Gardiner. Springer-Verlag: New York. 1984. pp 197.
13. M. Frenklach, and H. Wang, *Phys. Rev. B*, **43** (2), 1520-1545 (1991).
14. C. A. Wolden, K. K. Gleason, and J. B. Howard, *Combustion and Flame*, **96**, 75 (1994).
15. W. L. Hsu, *Appl. Phys. Lett.*, **59** (12), 1427-1429 (1991).
16. K.-H. Chen, M.-C. Chuang, C. M. Penney, and W. F. Banholzer, *J. Appl. Phys.*, **71** (3), 1485-1493 (1992).
17. L. L. Connell, J. W. Fleming, H.-N. Chu, D. J. Vestyck Jr., E. Jensen, and J. E. Butler, *J. Appl. Phys.*, **78** (6), 3622-3634 (1995).
18. D. G. Goodwin, *J. Appl. Phys.*, **74** (11), 6895-6906 (1993).
19. D. S. Dandy, and M. E. Coltrin, *J. Mater. Res.*, **10** (8), 1993-2010 (1995).
20. J. E. Butler, and R. L. Woodin, *Phil. Trans. R. Soc. Lond. A*, **342**, 209-224 (1993).
21. M. Frenklach, *J. Appl. Phys.*, **65** (12), 5142-5149 (1989).
22. S. J. Harris, *J. Appl. Phys.*, **56**, 2298 (1990).

23. D. D. Koleske, S. M. Gates, B. D. Thoms, J. N. Russell, Jr., and J. E. Butler, *J. Chem. Phys.*, **102** (2), 992-1002 (1995).

24. L. N. Krasnoperov, I. J. Kalinovski, H.-N. Chu, and D. Gutman, *J. Phys. Chem.*, **97**, 11787-11796 (1993).

25. D. G. Goodwin, *Appl. Phys. Lett.*, **59** (3), 277-279 (1991).

26. M. Frenklach, and K. E. Spear, *J. Mater. Res.*, **3** (1), 133-140 (1988).

27. M. P. D'Evelyn, C. J. Chu, R. H. Hange, and J. L. Margrave, *J. Appl. Phys.*, **71** (3), 1528-1530 (1992).

28. W. A. Yarbrough, K. Tankala, and T. DebRoy, *J. Mater. Res.*, **7** (2), 379-383 (1992).

29. S. J. Harris, and D. G. Goodwin, *J. Phys. Chem.*, **97**, 23-28 (1993).

30. M. E. Coltrin, and D. D. Dandy, *J. Appl. Phys.*, **74** (9), 5803-5820 (1993).

31. A. K. Sharma, and H. Yasuda, *Thin Solid Films*, **110**, 171-184 (1983).

32. I. Tajima, and M. Yamamoto, *J. Polym. Sci. Polym. Chem.*, **23**, 615-622 (1985).

33. C. Rau, and W. Kulisch, *Thin Solid Films*, **249**, 28-37 (1994).

34. I. Tajima, and M. Yamamoto, *J. Polym. Sci. Polym. Chem.*, **25**, 1737-1744 (1987).

35. J. Sakata, M. Yamamoto, and M. Hirai, *J. Appl. Polym. Sci.*, **31**, 1999-2006 (1986).

36. Y. Segui, and A. Bui, *J. Appl. Polym. Sci.*, **20**, 1611-1618 (1976).

37. A. M. Wróbel, M. R. Wertheimer, J. Dib, and H. P. Schreiber, *J. Macromol. Sci.-Chem. A.*, **14**, 321-337 (1980).

38. S. Sahli, M. A. Djouadi, S. Hadj-Moussa, F. Mansour, M. S. Aida, and Y. Segui, *Mater. Chem. Phys.*, **33**, 106-109 (1993).

39. V. S. Nguyen, J. Underhill, S. Fridman, and P. Pan, *J. Electrochem. Soc.*, **132**, 1925-1932 (1985).

40. R. A. Assink, A. K. Hays, R. W. Bild, and B. L. Hawkins, *J. Vac. Sci. Technol. A*, **3** (6), 2629-2633 (1985).

41. N. Inagaki, and M. Taki, *J. Appl. Polym. Sci.*, **27**, 4337-4343 (1982).

42. A. S. Chawla, *Trans. Am. Soc. Artif. Intern. Organs*, **25**, 287-293 (1979).

43. J. C. Angus, and C. C. Hayman, *Science*, **241**, 913-921 (1988).

44. F. P. Bundy, H. T. Hall, H. M. Strong, and R. H. Wentorf, *Nature*, **176**, 51-55 (1955).

45. H. Liander, and E. Lundblad, *Arkiv för Kemi*, **16** (9), 139-149 (1960).

46. B. V. Deryagin, and B. B. Spitsyn. *USSR Author's Certificate No. 399134*; . 1956.

47. J. C. Angus, N. C. Gardner, D. J. Poferl, S. Chauhan, and T. J. N. P. Sung, *Sint. Almazy*, **3**, 38 (1971).

48. D. J. Poferl, N. C. Gardner, and J. C. Angus, *J. Appl. Phys.*, **44**, 1428 (1973).

49. B. V. Deryagin, B. V. Spitsyn, L. L. Bouilov, A. A. Klochkov, A. E. Gorodestskii, and A. V. Smol'yanov, *Sov. Phys. Dokl.*, **21**, 676 (1976).

50. B. V. Spitsyn, L. L. Bouilov, and B. V. Deryagin, *J. Cryst. Growth*, **52**, 219 (1981).

51. S. Matsumoto, Y. Sato, M. Kamo, and N. Setaka, *Jpn. J. Appl. Phys.*, **21 part 2** (4), L183-L185 (1982).

52. C. A. Wolden, S. Mitra, and K. K. Gleason, *J. Appl. Phys.*, **72** (8), 3750-3758 (1992).

53. E. N. Farabaugh, A. Feldman, and L. Robins in *Proceedings of the 2nd International Conference on the New Diamond Science and Technology*, ed. by R. Messier, J. T. Glass, J. E. Butler, and R. Roy, 449-454, (1991).

54. M. Kamo, Y. Sato, S. Matsumoto, and N. Setaka, *J. Cryst. Growth*, **62**, 642-644 (1983).

55. S. Matsumoto, *J. Mater. Sci. Lett.*, **4**, 600-602 (1985).

56. S. Matsumoto, M. Hino, and T. Kobayashi, *Appl. Phys. Lett.*, **51** (10), 737-739 (1987).

57. K. Suzuki, A. Sawabe, H. Yasuda, and T. Inuzuka, *Appl. Phys. Lett.*, **50** (12), 728-729 (1987).

58. K. Suzuki, A. Sawabe, and T. Inuzuka, *Jpn. J. Appl. Phys.*, **29** (1), 153-157 (1990).

59. S. Okoli, R. Haubner, and B. Lux, *Journal de Physique*, **50** (5; C5), 159-167 (1989).

60. J. S. Kim, M. H. Kim, S. S. Park, and J. Y. Lee, *J. Appl. Phys.*, **67** (7), 3354 (1990).

61. M. Buck, T. J. Chang, J. J. Kaufman, and H. Seki in *Diamond, Silicon Carbide, and Related Wide Bandgap Semiconductors, MRS Symposia Proceedings*, **vol. 162**, ed. by J. T. Glass, R. Messier, and N. Fujimori, 97, (1990).

62. R. A. Rudder, G. C. Hudson, J. B. Posthill, R. E. Thomas, R. C. Hendry, D. P. Malta, R. J. Markunas, T. P. Humphreys, and R. J. Nemanich, *Appl. Phys. Lett.*, **60** (3), 329-331 (1992).

63. D. E. Patterson, B. J. Bai, C. J. Chu, R. H. Hauge, and J. L. Margrave in *Proceedings of the 2nd International Conference on the New Diamond Science and Technology*, ed. by R. Messier, J. T. Glass, J. E. Butler, and R. Roy, 433-438, (1991).

64. P. K. Bachmann, D. Leers, and H. Lydtin, *Diamond Relat. Mater.*, **1**, 1-12 (1991).

65. Y. Muranaka, H. Yamashita, and H. Miyadera, *J. Appl. Phys.*, **69** (12), 8145-8153 (1991).

66. K. V. Ravi, *J. Mater. Res.*, **7** (2), 384-393 (1992).

67. D. B. Oakes, J. E. Butler, K. A. Snail, W. A. Carrington, and L. M. Hanssen, *J. Appl. Phys.*, **69** (4), 2602-2610 (1991).

68. D. W. Hahn, C. F. Edwards, K. F. McCarty, and R. J. Kee, *Appl. Phys. Lett.*, **68**, 2158 (1996).

69. M. Murayama, S. Kojima, and K. Uchida, *J. Appl. Phys.*, **69**, 7924 (1991).

70. J. S. Kim, and M. A. Capelli, *J. Mater. Res.*, **10**, 149 (1995).

71. N. G. Glumac, and D. G. Goodwin, *Mater. Lett.*, **18**, 119 (1993).

72. K. Kurihara, K. Sasaki, M. Kawarada, and N. Koshino, *Appl. Phys. Lett.*, **52** (6), 437-438 (1988).

73. N. Ohtake, and M. Yoshikawa, *J. Electrochem. Soc.*, **137** (2), 717-722 (1990).

74. F. Jansen, M. A. Machonkin, and D. E. Kuhman, *J. Vac. Sci. Technol. A*, **8** (5), 3785-3790 (1990).

75. P. A. Dennig, and D. A. Stevenson, *Appl. Phys. Lett.*, **59** (13), 1562-1564 (1991).

76. R. Polini, *J. Appl. Phys.*, **72** (6), 2517-2519 (1992).

77. F. G. Celii, and J. E. Butler, *Annu. Rev. Phys. Chem.*, **42**, 643-684 (1991).

78. W. A. Yarbrough in *Applications of Diamond Films and Related Materials*, ed. by Y. Tzeng, M. Yoshikawa, M. Murakawa, and A. Feldman, 25-34, (1991).

79. R. A. Rudder, G. C. Hudson, R. C. Hendry, R. E. Thomas, J. B. Posthill, and R. J. Markunas in *Applications of Diamond Films and Related Materials*, ed. by Y. Tzeng, M. Yoshikawa, M. Murakawa, and A. Feldman, 395-398, (1991).

80. P. N. Barnes, and R. L. C. Wu, *Appl. Phys. Lett.*, **62** (1), 37-39 (1993).

81. R. J. Meilunas, R. P. H. Chang, S. Liu, and M. M. Kappes, *Appl. Phys. Lett.*, **59** (26), 3461-3463 (1991).

82. P. E. Pehrsson, and A. A. Morrish in *Proceedings of the 2nd International Conference on the New Diamond Science and Technology*, ed. by R. Messier, J. T. Glass, J. E. Butler, and R. Roy, 397-402, (1991).

83. C. J. Chu, M. P. D'Evelyn, R. H. Hauge, and J. L. Margrave, *Carbon*, **28**, 805 (1990).

84. J. B. Posthill, D. P. Malta, G. C. Hudson, R. E. Thomas, T. P. Humphreys, R. C. Hendry, R. A. Rudder, and R. J. Markunas, *Thin Solid Films*, **271** (1-2), 39-49 (1995).

85. J. B. Posthill, D. P. Malta, T. P. Humphreys, G. C. Hudson, R. E. Thomas, R. A. Rudder, and R. J. Markunas in *Film Synthesis and Growth Using Energetic Beams, MRS Symposium Proceedings*, **vol. 388**, ed. by H. A. Atwater, J. T. Dickinson, D. H. Lowndes, and A. Polman, 299-304, (1995).

86. S. Koizumi, T. Murakami, T. Inuzuka, and K. Suzuki, *Appl. Phys. Lett.*, **57** (6), 563-565 (1990).

87. D. N. Belton, and S. J. Schmieg, *J. Appl. Phys.*, **66** (9), 4223-4229 (1989).

88. Y. Sato, H. Fujita, T. Ando, T. Tanaka, and M. Kamo, *Phil. Trans. R. Soc. Lond. A*, **342**, 225-231 (1993).

89. P. C. Yang, W. Zhu, and J. T. Glass, *J. Mater. Res.*, **8** (8), 1773-1776 (1993).

90. W. Zhu, P. C. Yang, and J. T. Glass, *Appl. Phys. Lett.*, **63** (12), 1640-1642 (1993).

91. J. F. Prins, and H. L. Gaigher in *Proceedings of the 2nd International Conference on the New Diamond Science and Technology*, ed. by R. Messier, J. T. Glass, J. E. Butler, and R. Roy, 561-566, (1991).

92. S.-T. Lee, S. Chen, G. Braunstein, X. Feng, I. Bello, and W. M. Lau, *Appl. Phys. Lett.*, **59** (7), 785-787 (1991).

93. H. A. Hoff, D. J. Vestyck Jr., J. E. Butler, and J. F. Prins, *Appl. Phys. Lett.*, **62** (1), 34-36 (1993).

94. J. Narayan, V. P. Godbole, and C. W. White, *Science*, **252**, 416-418 (1991).

95. S.-T. Lee, S. Chen, J. Agostinelli, G. Braunstein, L. J. Huang, and W. M. Lau, *Appl. Phys. Lett.*, **60** (18), 2213-2215 (1992).

96. S. P. Withrow, C. W. White, R. A. Zuhr, J. W. McCamy, S. J. Pennycook, and J. D. M. Hembree, *J. Appl. Phys.*, **72** (8), 3485-3491 (1992).

97. M. W. Geis, H. I. Smith, A. Argoitia, J. Angus, G.-H. M. Ma, J. T. Glass, J. Butler, C. J. Robinson, and R. Pryor, *Appl. Phys. Lett.*, **58** (22), 2485-2487 (1991).

98. W. Zhu, X. H. Wang, B. R. Stoner, G. H. M. Ma, H. S. Kong, M. W. H. Braun, and J. T. Glass, *Phys. Rev. B*, **47** (11), 6529-6542 (1993).

99. N. N. Sheftal, *Growth of Crystals*; **vol. 10**, ed. by N. N. Sheftal. Consultants Bureau: New York. 1976.

100. M. W. Geis, N. N. Efremow, R. Susalka, J. C. Twichell, K. A. Snail, C. Spiro, B. Sweeting, and S. Holly, *Diamond Relat. Mater.*, **4**, 76-82 (1994).

101. R. W. Pryor, M. W. Geis, and H. R. Clark in *Mat. Res. Soc. Symp. Proc.*, **vol. 242**, 13-22, (1992).

102. R. Spitzl, V. Raiko, and J. Engemann, presented at the 4th European Conference on Diamond, Diamond-like and Related Materials, Albufeira and Algarve, Portugal, 1993 (unpublished).

103. R. Spitzl, V. Raiko, R. Heiderhoff, H. Gnaser, and J. Engemann, *Diamond Relat. Mater.*, **4**, 563-568 (1995).

104. C. Wild, P. Koidl, N. Herres, W. Müller-Sebert, and T. Eckermann, *Electrochem. Soc. Proc.*, **91-8**, 224-239 (1991).

105. C. Wild, P. Koidl, W. Müller-Sebert, H. Walcher, R. Kohl, N. Herres, and R. Locher, *Diamond Relat. Mater.*, **2**, 158-168 (1993).

106. B. R. Stoner, and J. T. Glass, *Appl. Phys. Lett.*, **60** (6), 698-700 (1992).

107. C. H. Carter, R. F. Davis, and S. R. Nutt, *J. Mater. Res.*, **1**, 811 (1986).

108. H. S. Kong, Y. C. Wang, J. T. Glass, and R. F. Davis, *J. Mater. Res.*, **3**, 521 (1988).

109. B. R. Stoner, S. R. Sahaida, J. P. Bade, P. Southworth, and P. J. Ellis, *J. Mater. Res.*, **8** (6), 1334-1340 (1993).

110. I. Glassman, *Combustion*; 2nd ed. Academic: Orlando. 1987.

111. H. V. Boenig, *Plasma Science and Technology*. Cornell U. P.: Ithaca, New York. 1982.

112. M. P. Everson, and M. A. Tamor, *J. Mater. Res.*, **7** (6), 1438-1444 (1992).

113. E. Molinari, R. Polini, M. L. Terranova, P. Ascarelli, and S. Fontana, *J. Mater. Res.*, **7** (7), 1778-1787 (1992).

114. D. N. Belton, S. J. Harris, S. J. Schmieg, A. M. Weiner, and T. A. Perry, *Appl. Phys. Lett.*, **54** (5), 416-417 (1989).

115. M. Tsuda, M. Nakajima, and S. Oikawa, *J. Am. Chem. Soc.*, **108**, 5780 (1986).

116. D. N. Belton, and S. J. Harris, *J. Chem. Phys.*, **96**, 2371 (1992).

117. M. Frenklach, *J. Chem. Phys.*, **97** (8), 5794-5802 (1992).

118. S. P. Mehandru, and A. B. Anderson, *J. Mater. Res.*, **5** (11), 2286-2295 (1990).

119. R. E. Duff, and S. H. Bauer, *J. Chem. Phys.*, **36**, 1754 (1962).

120. S. C. Khandelwal, and G. B. Skinner, *Shock Waves in Chemisty*, ed. by A. Lifshitz. Marcell Dekker: New York. 1981.

121. M. Frenklach, D. W. Clary, W. C. Gardiner, and S. T. Stein in *20th International Symposium on Combustion*, 887, (1984).

122. S. J. Harris, A. M. Weiner, and R. J. Blint, *Combustion and Flame*, **72**, 91 (1988).

123. C. K. Westbrook, J. Warnatz, and W. J. Pritz in *22nd International Symposium on Combustion*, 893, (1988).

124. A. M. Wróbel, and M. R. Wertheimer, *Plasma Deposition, Treatment, and Etching of Polymers*, ed. by R. d'Agostino. Academic Press: San Diego. 1990. pp 163-268.

125. R. Szeto, and D. W. Hess, *J. Polym. Sci. Polym. Lett. Ed.*, **19**, 119-123 (1981).

126. M. R. Alexander, R. D. Short, F. R. Jones, M. Stollenwerk, J. Zabold, and W. Michaeli, *J. Mater. Sci.*, **31**, 1879-1885 (1996).

127. D. R. Secrist, and J. D. Mackenzie, *J. Electrochem. Soc.*, **113**, 914-920 (1966).

128. A. K. Hays, *Thin Solid Films*, **84**, 401-407 (1981).

129. F. Kokai, T. Kubota, M. Ichijo, and K. Wakai, *Proc. ACS Div. of Polymeric Materials: Science and Engineering*, **56**, 505-509 (1988).

130. A. M. Wróbel, *Plasma Chem. Plasma Process.*, **7**, 429-450 (1987).

131. K. Obi, A. Clement, H. E. Gunning, and O. P. Stausz, *J. Am. Chem. Soc.*, **91**, 1622-1630 (1969).

132. L. Gammie, I. Safarik, O. P. Strausz, R. Roberge, and C. Sandorfy, *J. Am. Chem. Soc.*, **102**, 378-380 (1980).

133. A. M. Wróbel, M. Kryszewski, and M. Gazicki, *J. Macromol. Sci.-Chem. A.*, **A20** (5-6), 583-618 (1983).

134. W. Noll, *Chemistry and Technology of Silicones*; 2nd ed. Academic Press: New York. 1968.

135. R. v. Noort, and M. M. Black, *Biocompatibility of Clinical Implant Materials*; **vol. 2**, ed. by D. F. Williams. CRC Press: Boca Raton. 1981. pp 79-98.

136. W. Peters, D. Smith, S. Lugowski, A. McHugh, P. MacDonald, and C. Baines, *Immunology of Silicones*, ed. by M. Potter, and N. R. Rose. Springer-Verlag: Berlin. 1996. pp 30-48.

137. A. S. Chawla, *Artif. Organs*, **3**, 92 (1979).

138. A. S. Chawla, *Biomaterials*, **2**, 83-88 (1981).

139. Y. Ishikawa, S. Sasakawa, M. Takase, Y. Iriyama, and Y. Osada, *Makromol. Chem. Rapid Commun.*, **6**, 495-502 (1985).

140. A. R. Ozdural, J. Hameed, M. Y. Boluk, and E. Piskin, *ASAIO J.*, **3** (116), 1980 (1980).

141. K. W. Bieg, and K. B. Wischmann, *Solar Energy Mater.*, **3**, 301-316 (1980).

142. H. P. Schreiber, M. R. Wertheimer, and A. M. Wróbel, *Thin Solid Films*, **72**, 487-493 (1980).

143. T. Wydeven, *Appl. Opt.*, **16**, 717-721 (1977).

144. J. R. Hollahan, and T. Wydeven, U.S.A. Patent No. 4,137,265 (1979).

145. R. M. Kubacki, U.S.A. Patent No. 4,096,315 (1978).

146. P. K. Tien, *Rev. Mod. Phys.*, **49**, 361-420 (1977).

147. G. Smolinsky, P. K. Tien, and M. Vasile, U.S.A. Patent No. 3,822,928 (1974).

148. P. K. Tien, G. Smolinsky, and R. J. Martin, *Appl. Opt.*, **11**, 637-642 (1972).

149. M. Yamamoto, J. Sakata, and M. Hirai, *J. Appl. Polym. Sci.*, **29**, 2981-2987 (1984).

150. J. Sakata, and M. Yamamoto, *J. Appl. Polym. Sci., Appl. Polym. Symp.*, **42**, 339-356 (1988).

2. HOT-FILAMENT REACTOR DESCRIPTION

The hot-filament reactor used throughout this work has been described previously elsewhere[1] but an overview will be presented for completeness. Also, any modifications and additions to the original design will be described in detail.

An overview schematic of the HFCVD system is shown in Figure 2-1. The main reactor is made up of a homebuilt chamber which consists of a central body formed from a 10" x 10" x 5" aluminum block with an 8" diameter hole, a top 10" x 10" x 1" plate, and a bottom 10" x 10" x1" plate. Both plates have a circular o-ring groove cut into them; the chamber seals by using atmospheric pressure to squeeze the two plates against the body of the reactor. The plates are not otherwise directly attached to the chamber. The top plate has an o-ring sealed 6.5" quartz window mounted in the center and two gas outlets. In those cases where the hot filament must be mounted higher than the center of the chamber where it usually sits in order to provide additional clearance below it, a copper plate with several small openings is placed between the filament and the quartz plate to block out most of the radiation and prevent the window from overheating and damaging the seals. The original bottom plate had four feedthroughs, two for the DC power, one for the pressure transducer, and one for a gas inlet. Figure 2-2 and 2-3 show the new bottom plate which incorporates a translatable, water cooled copper stage; Figure 2-4 shows an exploded view of the stage itself. The stage allows samples to be positioned facing upwards over a 2" range of vertical movement and was designed to hold up to a 4" wafer. An internal tube running down the center of the stage allows a K-type chromel-alumel thermocouple (Omega, 1/16" diameter) to measure the backside temperature of the substrate. The

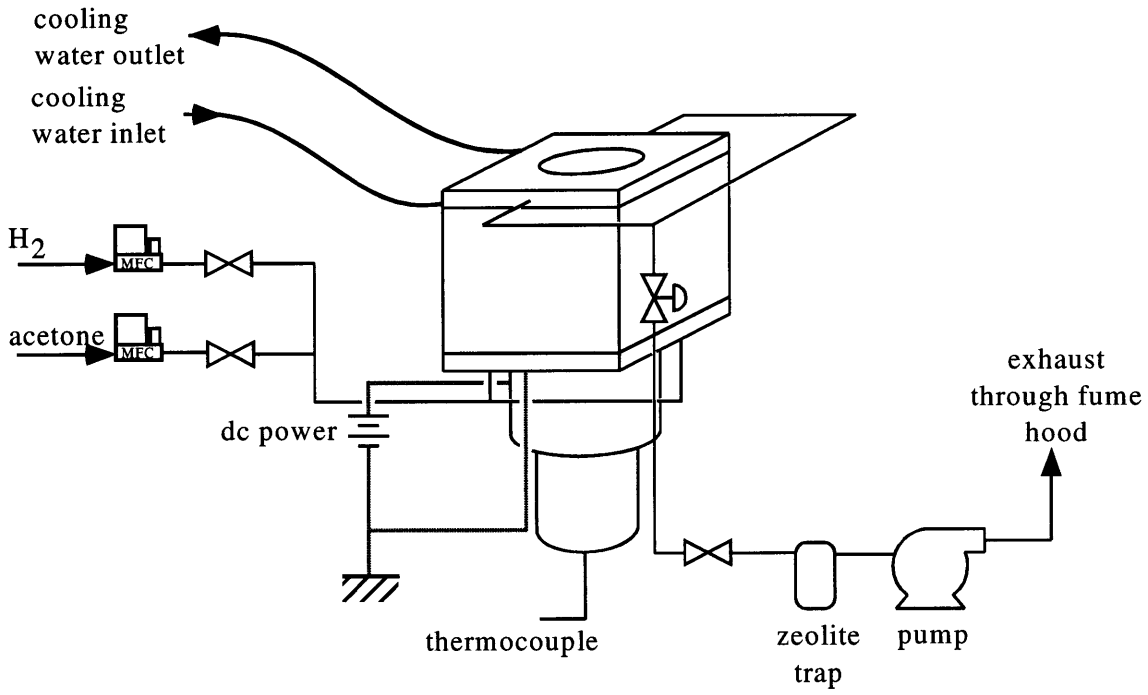

Figure 2-1: Process schematic of hot-filament CVD system

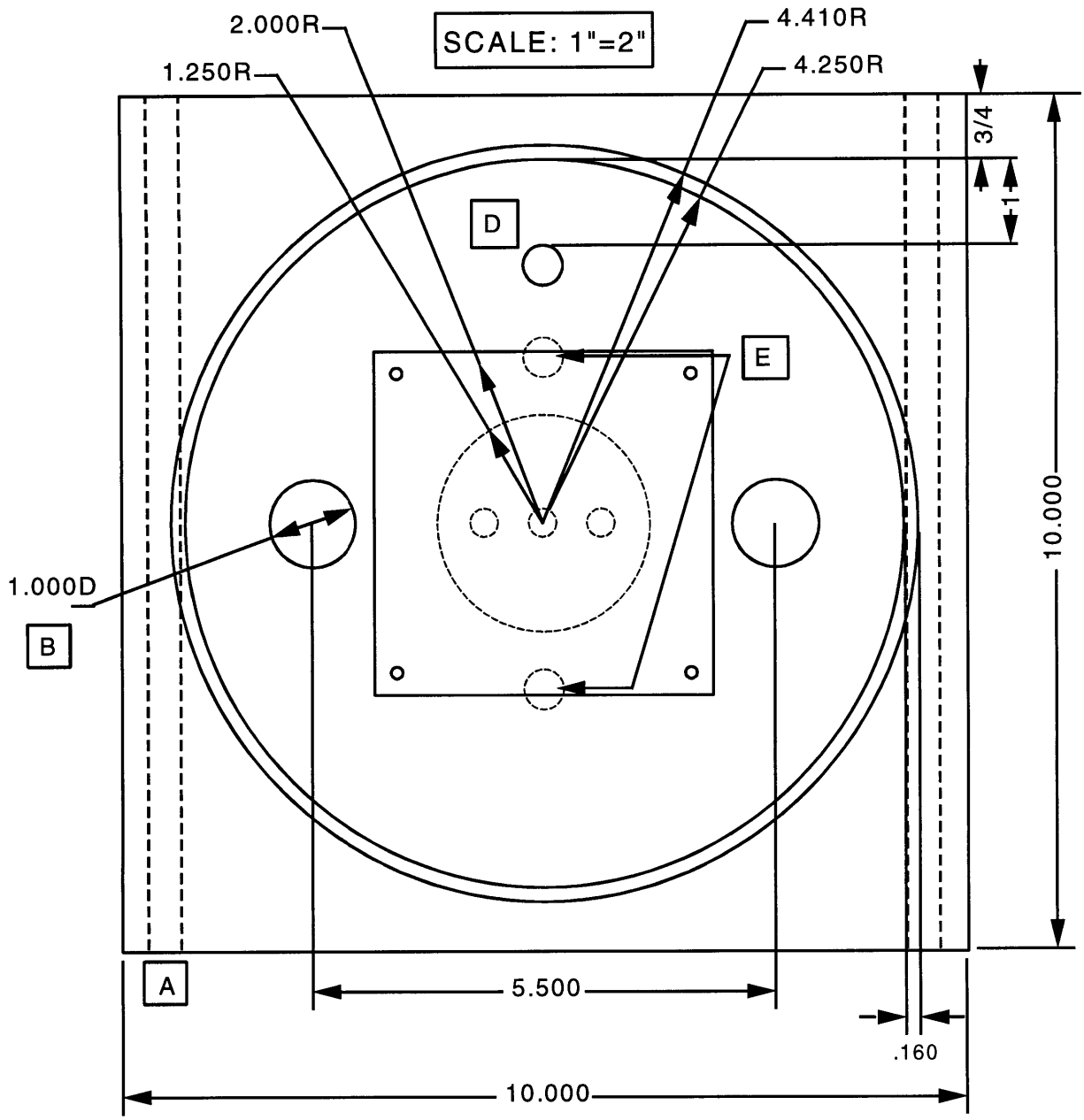

A) water cooling channels; 7/16-20 threads, 0.41" at each end

B) unthreaded holes for power feedthroughs

C) coolant feeds for stage; 5/16-24 threads, 0.34"

D) hole for pressure transducer; 7/16-20 thread, 0.41"

E) holes for exhaust to pump; 7/16-20 thread, 0.41"

F) 13 threads/inch, 1.6" on inner, 1.5" on outer. Threads should have a depth of 0.05". (=> 0.25mm per 1/8 turn)

G) 1/16" chamfer

TOP VIEW

Figure 2-2: Drawing of modified reactor bottom plate (top view)

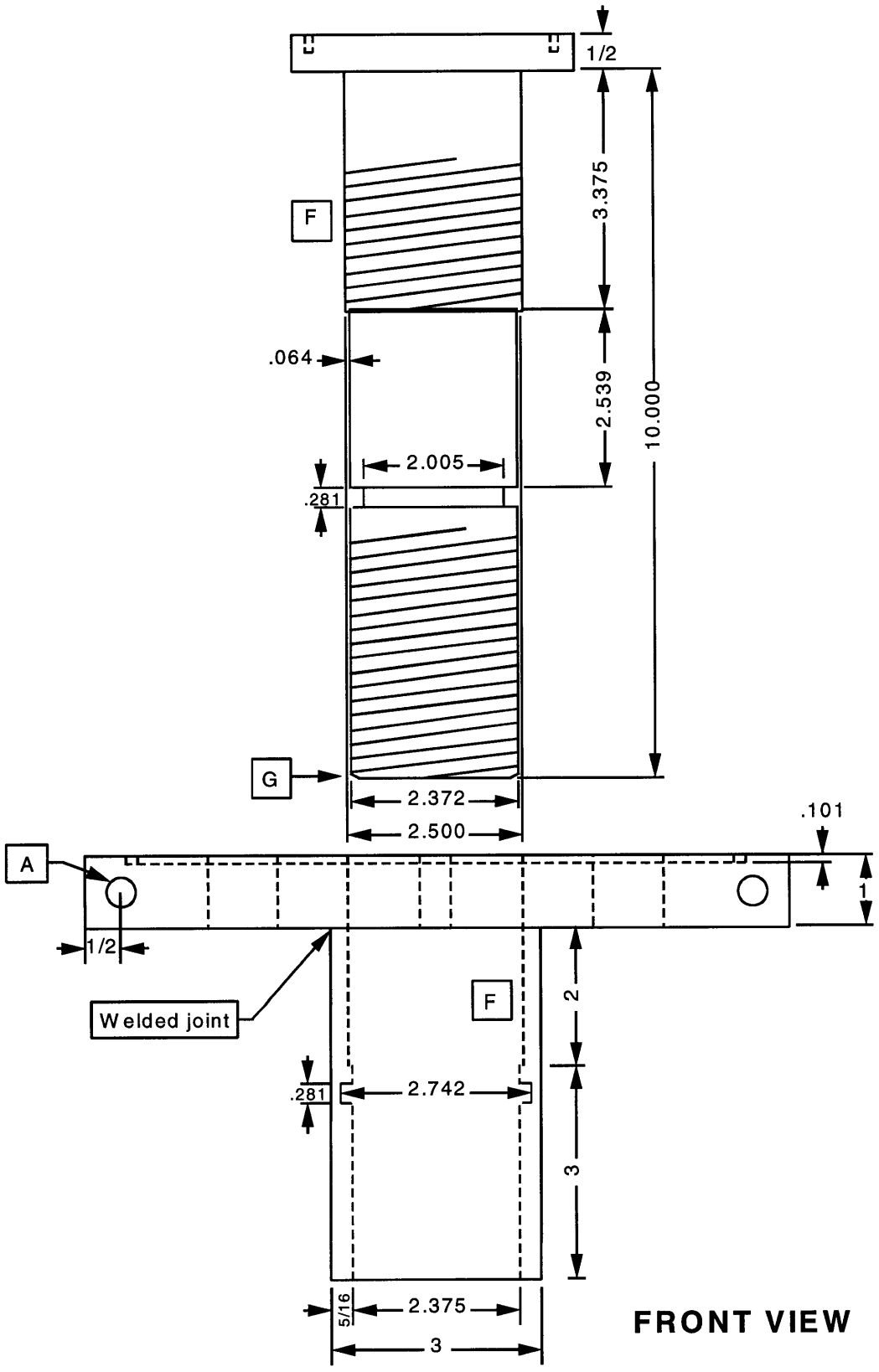

Figure 2-3: Drawing of modified reactor bottom plate (front view)

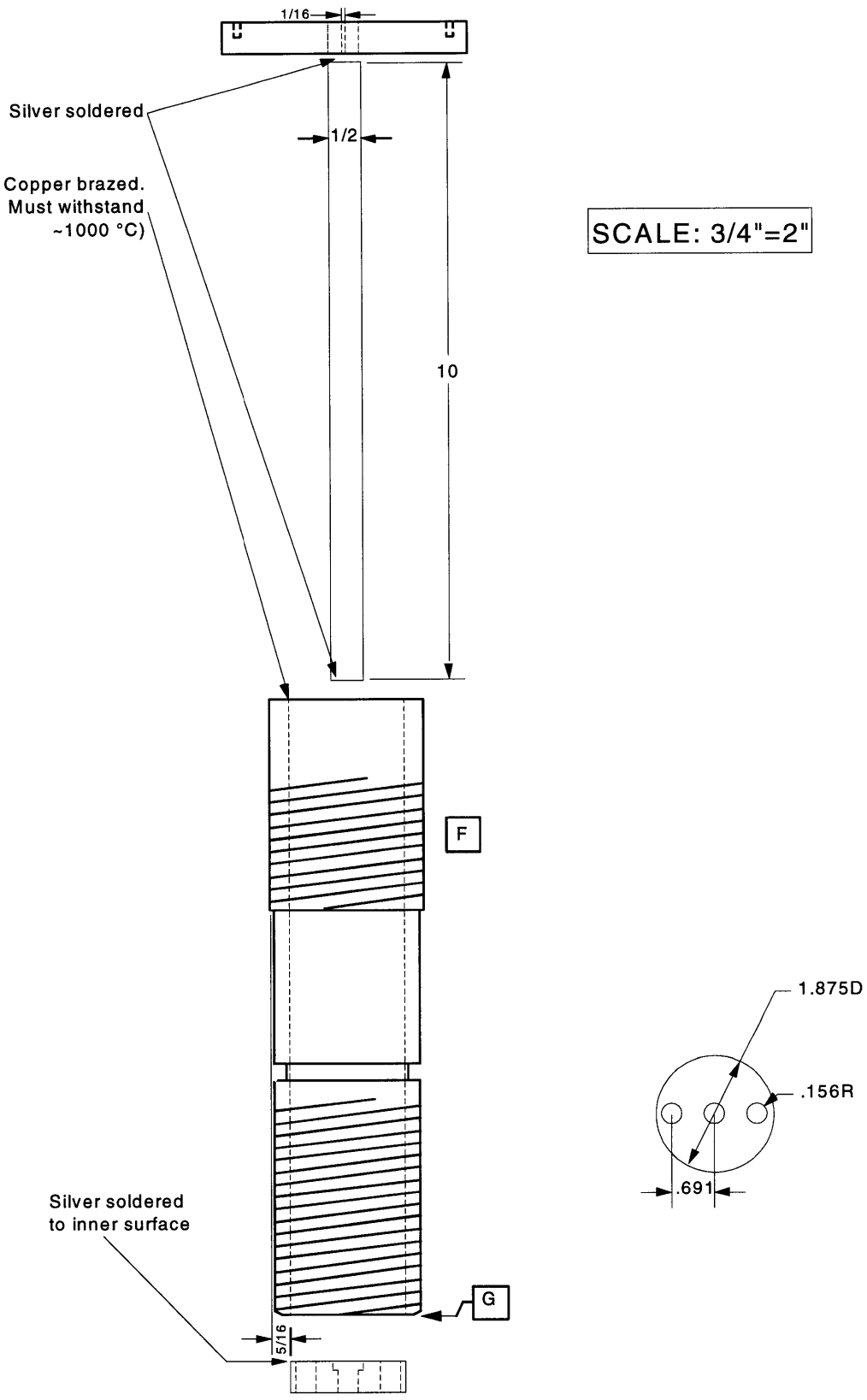

Figure 2-4: Drawing of translatable, water-cooled copper stage

thermocouple is sealed with an Ultra-Torr o-ring seal. The stage itself is sealed with one of two o-rings which grip the cylindrical portion of the stage. There were originally five feedthroughs in the modified bottom plate, two for the DC power feedthroughs, one for the pressure transducer, and two on either side of the stage for gas inlet. A sixth 1" throughhole was later added to accommodate either a Del-Base electrical feedthrough (ISI, 9414003) or a butterfly throttle valve (MDC, KBFV-100) on a Del-Base adapter.

Power to the hot filament was supplied through two high current Del-Base electrical feedthroughs (MDC, FHC-1000) which are capable of handling 1000 A at 50 V. The filament was clamped between copper plates which were bolted onto the feedthroughs. Two different power supplies have been used to power the filament. A large 10kW (Sorenson, DCR-32-310T1) supply was originally used; it was capable of delivering 310 A and 32V. Later on, a smaller 1kW (Sorenson, DCS-20-50, max. 50A at 20 V) supply was used because of electrical interference problems with the larger supply. The power was delivered to the power feedthroughs with high capacity arc-welding cable and attached to the atmospheric side of the feedthroughs with brass nuts. Both power supplies could be operated in voltage limiting or current limiting mode and have programmable overload settings. In the unlikely event of a filament breakage during operation, it is safer to be operating in voltage limited mode since the supply would automatically go to zero as the resistance increased. It is also a good idea to operate with a voltage overload alarm set to 10-20% higher than the highest normal operating voltage.

Unless otherwise stated, 1" diameter tantalum filaments (Alfa-Aesar) were used. Tantalum was chosen instead of tungsten because it is easier to shape at ambient conditions; tungsten is stiffer and generally needs to be heated to be worked. For the

diamond deposition experiments, newly formed Ta filaments were pretreated to grow a carbide layer on the outer surface before beginning any actual experiments. Relative to the standard deposition conditions, a typical pretreatment takes place at the same gas phase composition, elevated pressures (50 torr), and lower filament temperatures (stepwise increase to deposition conditions over 2 hours). This carburization would ordinarily occur on a fresh filament during the course of a deposition anyway. The pretreatment simply insures that this occurs in a controlled fashion and that the filament no longer acts to deplete carbon from the gas phase during an experiment. In addition, the formation of the hard carbide surface at a reduced filament temperature allows the filament to better hold its original shape when it is finally heated up to the actual operating temperature.

The body and the plates have a total of ten through channels for water cooling. Copper, not plastic, tubing should be used to route water in the cooling system since they are not susceptible to leakage and failure. Two other separate cooling water circuits supplied water to the copper stage and to the electrical power feedthroughs which typically experienced considerably higher heat loads than the chamber walls. Because there was no way to directly control the degree of cooling to the stage, the substrate was often overcooled, depending on the filament geometry and the resultant heat load. In those cases, alumina disks of various sizes (Aesar-Alfa) as well as a copper tripod were used as spacers between the wafer and the stage to reduce the degree of cooling.

The chamber was evacuated with a dual-stage rotary vane pump (Leybold, Trivac D16A) that is capable of displacing 14.1 cfm. The reactor pressure was measured with a differential pressure transducer (MKS, 223BD-01000AAB) for the higher pressure experiments (>~10 torr) while an absolute transducer (MKS, 622A11TAE) was used for

the lower pressure ones. To control the pressure, a flow regulating needle valve (Whitey, B-1RS4) was used between the reactor and the pump. At higher operating pressures where the valve only needs to be open a small fraction of a turn, the control of the pressure required a delicate touch and/or constant adjustment. At lower operating pressures (<~1 torr) such as used in the silicone deposition experiments, the pressure was controlled by adjusting the butterfly throttle valve on the larger 1" port on the base of the reactor.

Gas flow into the reactor was controlled by several thermal-type mass flow controllers (MKS, 1259C). Hydrogen was regulated by a specially calibrated 500 sccm MFC while other process gases were regulated by N_2 calibrated MFC's. To flow other gases, gas-dependent calibration factors had to be used. In the case of acetone, $f_{acetone} = 0.34*f_{nitrogren}$. The gas correction factors were entered into a 4-channel readout / controller / power supply (MKS, 247C) so that the actual gas flowrates could be read directly. In addition, because acetone attacks standard Viton o-rings, special solvent-resistant (butyl) seals had to installed at the factory for the acetone MFC. When a low vapor pressure, thermally-sensitive material such as the octamethylcyclotetrasiloxane used in the silicone deposition was flowed into the reactor, the mass flow controller was replaced with two large bore valves, one to regulate the flow and the other to act as a positive shutoff. In normal, daily operation, only the shutoff valve would be opened and closed while the regulating valve would be adjusted to give an approximate flowrate at a certain pressure based on a pressure rise calibration. The MFC was replaced in this case because its narrow orifice reduced the flow to some degree even when fully opened. There was also a potential for clogging in the capillary tube used in the thermal flow measurement method

of the MFC. Once correctly metered, the gases were mixed in a t-connection before being split off again to enter the reactor.

References

1. K. M. McNamara, Ph. D. Thesis, Massachusetts Institute of Technology, 1992.

3. DIAMOND NUCLEATION ON ZEOLITES

As discussed in Chapter 1, one of the key technological hurdles in the field of diamond CVD is the inability to nucleate and grow a thin film of single crystal diamond over a large area. The impracticality of homoepitaxy over a large diamond substrate and the problems associated with heteroepitaxial growth on non-diamond substrates such as lattice and thermal expansion coefficient mismatches have motivated researchers to search out other techniques. Mosaic films produced by nucleating growth on (111) faceted diamond crystals sitting in a square array of 90^2 μm^2 pits on 100 μm centers suggest a possible alternative approach.[1] When such films are grown out to several hundred microns in thickness, the grain boundaries between the separately nucleated crystals begin to grow together. If this idea could be shrunk down in size, it would be possible to deposit films which grow together at considerably thinner film thickness. Polycrystalline film deposition on randomly distributed sites with a nominal spacing of 5-200 nm has already been shown on porous silicon.[2] When compared with porous silicon substrates, the nucleation site spacing on a zeolite crystal is potentially another two orders of magnitude smaller thereby reducing the mosaic film concept down to its smallest limit.

3.1 Description of zeolites

Zeolites, also known as molecular sieves, are a general class of nanoporous, crystalline materials that are widely used in the chemical industry as catalysts and adsorbents. Most zeolites are aluminosilicates and have a general composition of $H_mAl_mSi_{m-n}O_{2m}$. Some also incorporate low molecular weight, singly charged cations

such as sodium and magnesium. At the other end of the spectrum, materials such as silicalite are composed solely of Si and O. Since zeolites become more thermally stable as their Si/Al ratio increases, silicalite, which is stable to 1200 °C was selected as a substrate for diamond deposition. Because of their crystallinity, zeolite surfaces display a distinct, regular structure composed of pore openings that range from 2-15 Å separated by interpore spacings which range from 5-31 Å.[3] In particular, silicalite, which has a ZSM-5 crystal structure, has two distinct, intersecting sets of channels. Running in the [010] direction are a set of straight, elliptical channels with a free cross-section of 5.2 Å x 5.8 Å; perpendicular to these are a set of near-circular sinusoidal channels with a free cross-section of 5.4 Å.[3] Figure 3-1 is a schematic of the ZSM-5 channel system. Because of its regular three dimensional structure, the surface of ZSM-5 has openings that are spaced 12 Å to 20 Å apart, depending on the particular direction and crystal face.

In this study, the silicalite crystals used are uniformly 60 x 15 x15 μm in size. Examples are shown in the SEM in Figure 3-2.

3.2 Experimental setup

All of the experiments were performed with the hot filament chemical vapor deposition (HFCVD) system detailed in Chapter 2 with hydrogen and acetone as the feed gases. The gases were activated with a planar, S-shaped tantalum filament. Typical deposition conditions were gas feeds of 150 sccm of H_2, 1.5 sccm of acetone, and a substrate temperature of 780 °C. The reactor pressure was 100 torr during the first ½ hour of deposition and was changed to 20 torr for the remaining 2 hours. When silicon wafers seeded with 0.5 μm diamond grit were used as substrates for this process, well faceted,

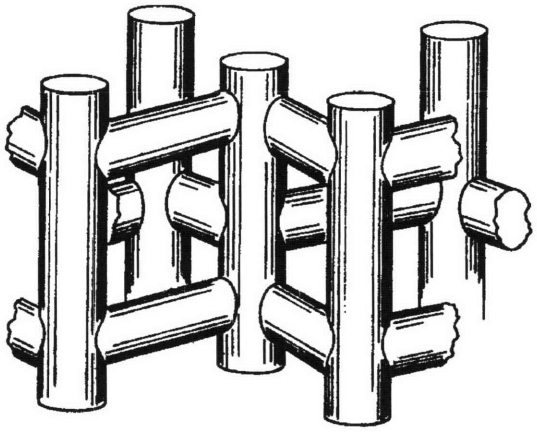

Figure 3-1: ZSM-5 channel system

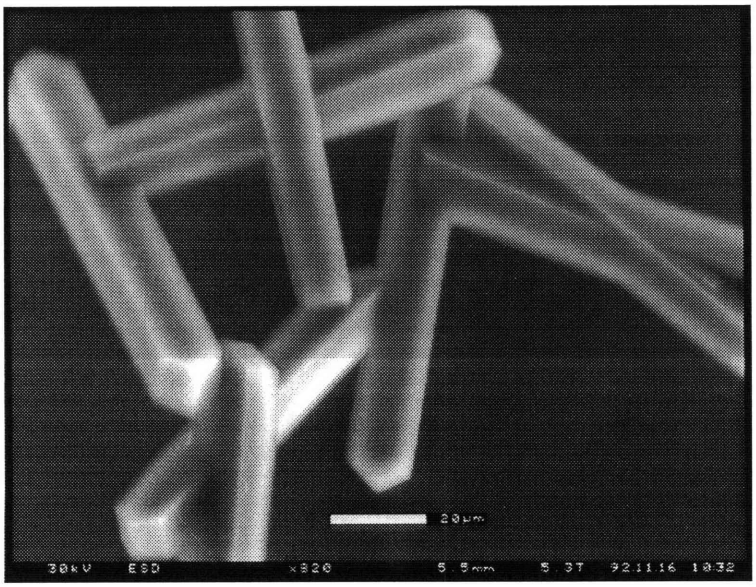

Figure 3-2: Scanning electron micrograph of high Si ZSM-5 zeolite crystals

~7 μm thick polycrystalline diamond films resulted. Runs without the initial high pressure period resulted in etching of the silicalite crystals, probably due to the flux of H-atoms.

3.2.1 sp^3 bonded hydrocarbon seed

Matsumoto and Matsui have previously suggested that adamantane ($C_{10}H_{16}$; see Figure 3-3) and similar hydrocarbon cage compounds may act as "embryos" for diamond nucleation.[4] Working from the hypothesis that some form of sp^3-bonded carbon acts as the nuclei for diamond formation, we used adamantane as our model compound. In addition, adamantane has an diameter of approximately 4 Å which should allow it to diffuse through the silicalite pores easily. Seeding was accomplished by placing the calcined zeolite powder into a solution of adamantane in methylene chloride for several days.

Scanning electron microscopy (SEM; ElectroScan Environmental Scanning Electron Microscope) and transmission electron microscopy (TEM) were used to analyze the post-deposition samples. The SEM's required no special sample preparation because of the nature of the instrument. TEM films were prepared by subjecting the as-deposited samples to a hydrogen-only feed in the HFCVD reactor for half an hour; any remaining silicalite crystals or non-diamond carbon films were etched away. The residual material was then scraped onto a number of carbon film coated TEM grids for analysis.

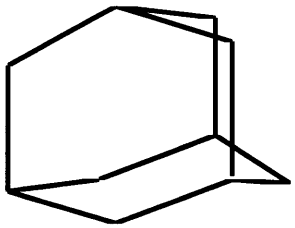

Figure 3-3: Structure of adamantane

3.2.2 sp^2 bonded hydrocarbon seed

It has also been proposed that diamond nucleation begins at the "edges" of sp^2-bonded carbon compounds. In particular, Angus has reported the growth of diamond particles from the edges of the basal planes of highly oriented pyrolitic graphite (HOPG) and from perylene tetracarboxylic acid dianhydride.[5] To investigate this possibility, a homologous series of linear polyaromatic hydrocarbons was also used as hydrocarbon seeds. They were naphthalene, anthracene, 2,3-benzanthracene, and 1,2:5,6-dibenzanthracene (see Figure 3-4). In addition, experiments were performed with acetone feeds of 0 and 1.0 sccm during the initial high pressure period to test the hypothesis that the local C-concentration at the zeolite surface may have been overly high and led to amorphous C deposition.

The analysis and characterization of samples were performed through SEM and Auger electron spectroscopy (AES). Samples for AES were prepared by manually moving and embedding the zeolite crystals into indium foil.

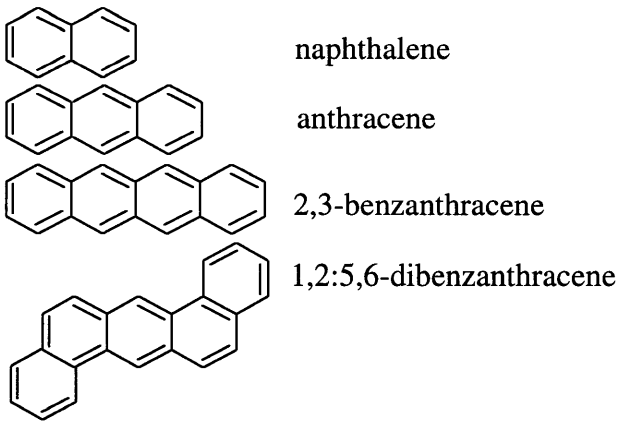

Figure 3-4: Series of linear polyaromatic hydrocarbons used as seed molecules

3.3 Results

3.3.1 sp^3 bonded hydrocarbon seed

The SEM result is displayed in Figure 3-5 and shows a shattered silicalite shaped shell. This translucent film is also accompanied by secondary nucleation of diamond on the film and on the silicon wafer.

The TEM image from an approximately 1 μm^2 film is shown in Figure 3-6. Note that it is composed of crystalline regions of roughly 10 Å diameter within an otherwise amorphous matrix. The electron diffraction pattern is shown in Figure 3-7 and graphically in Figure 3-8; it identifies the crystalline component as ß-SiC.

3.3.2 sp^2 bonded hydrocarbon seed

Figures 3-9 and 3-10 show the SEM results from the anthracene seeded experiments in which 1.0 sccm of acetone was used initially; Figure 3-11 shows the result from the 0 sccm experiment. The smooth coating on the zeolite in Fig. 3-9 is most likely an amorphous carbon coating. Figure 3-10 is a higher magnification image of one of the point nucleated diamond particles shown in Fig. 3-9. Similar nucleation behavior has been observed by Li, *et al.* in the case of diamond nucleation on the edges of HOPG.[6] Because the SEM images from the experiments involving 2,3-benzanthracene and 1,2:5,6-dibenzanthracene showed that the majority of the zeolites were etched, it was concluded that the relatively large size of the seeds prevented them from diffusing into the zeolite pores and no further analysis was done upon those samples.

In addition to analyzing the experimental samples via AES, standard spectra were taken of a free-standing HFCVD diamond film and of a crystalline graphite powder; they

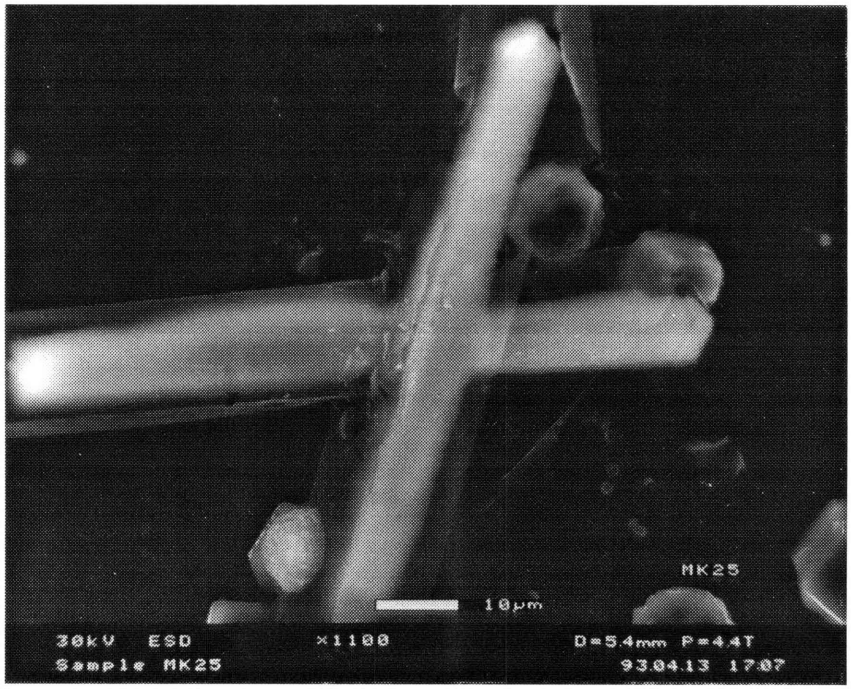

Figure 3-5: SEM of "transluscent" zeolite shaped shell with secondary diamond nucleation

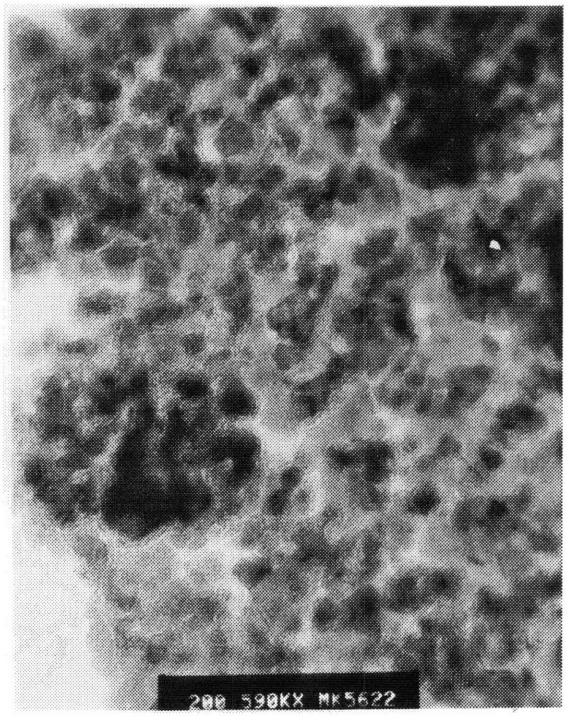

Figure 3-6: TEM of residual material from an as-deposited sample after exposure to a H_2 only feed

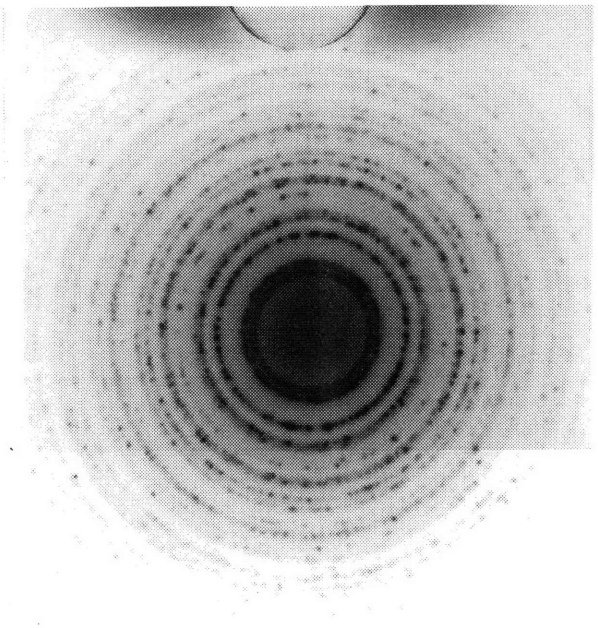

Figure 3-7: Electron diffraction pattern from the sample shown in Fig. 3-6

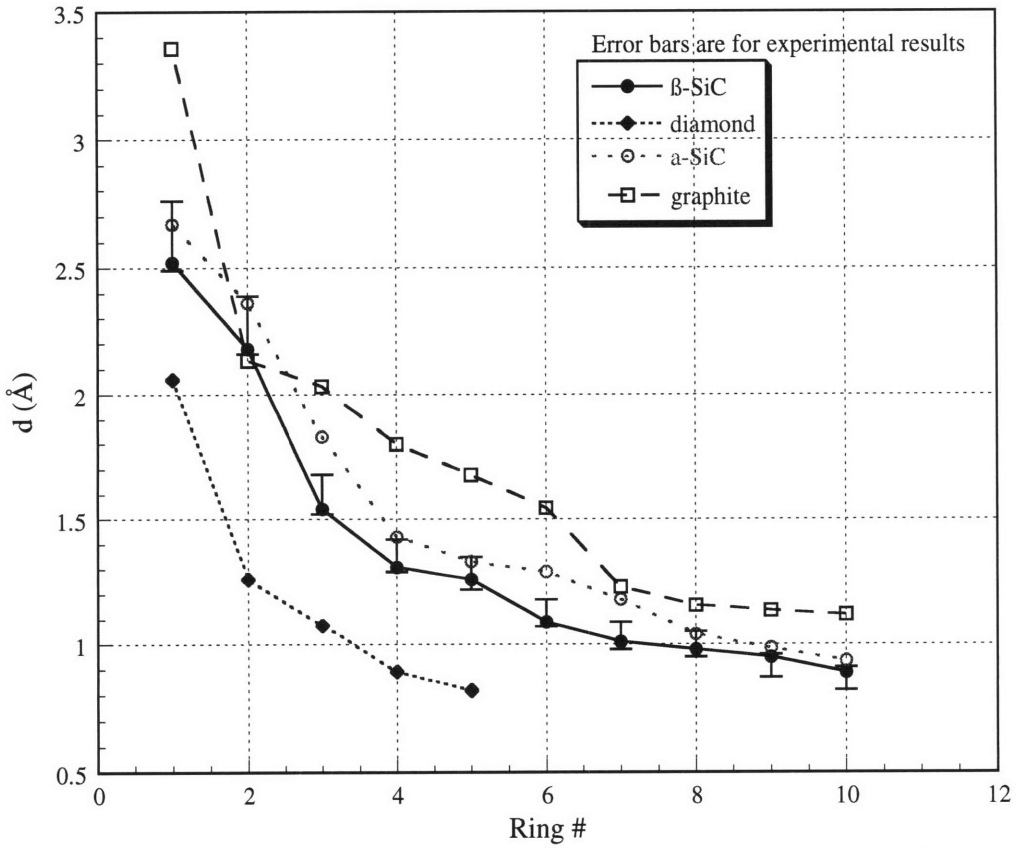

Figure 3-8: Comparison of experimental electron diffraction results with literature values for ß-SiC, a-SiC, diamond, and graphite.

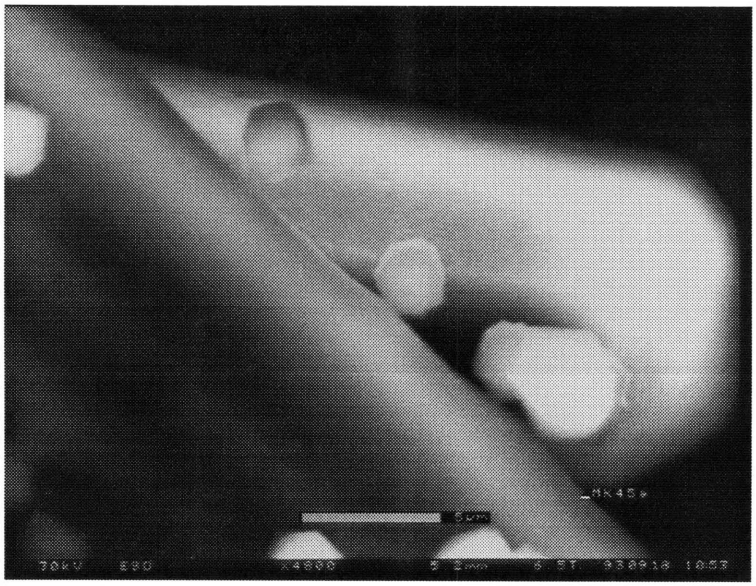

Figure 3-9: SEM of results from anthracene seeded experiments with 1.0 sccm of acetone initially

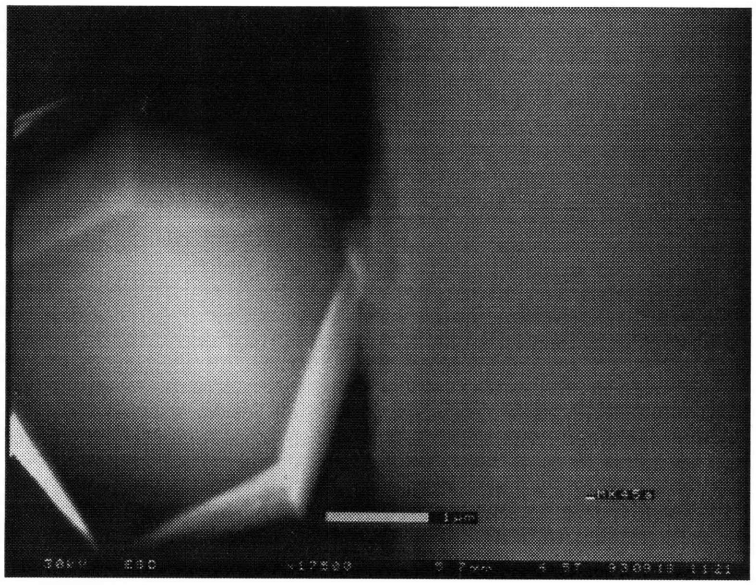

Figure 3-10: Higher magnification of the nucleation of a diamond particle from the sample shown in Fig. 3-9

are displayed in Figure 3-12 along with a spectra of ß-SiC from Kaplan.[7] The distinguishing features to note are in the region immediately preceding the 272 eV C-KLL transition. Figure 3-13 shows another silicalite crystal from the sample shown in Fig. 3-11. An AES spectrum was taken from the outlined area after sputtering with a 1.5 keV Ar^+ ion gun at a flux of $9.8x10^{18}$ cm^{-2} and is also shown in Fig. 3-12. Prior to sputtering, the sample exhibited an amorphous carbon spectra characteristic of adventitious carbon contamination. While the buckled film is clearly not diamond nor graphite, a careful comparison of the Auger spectra for ß-SiC and the film on the zeolite in Fig. 3-13 indicates that the film is also not ß-SiC.

3.4 Conclusions

A novel method for controlling the nucleation of CVD diamond films at the molecular level has been proposed using zeolites as potential substrates. By saturating the pore channels of a silicalite crystal with hydrocarbon seeds to induce and control nucleation, films were grown in a HFCVD system. The hydrocarbons used were adamantane, naphthalene, anthracene, 2,3-benzanthracene, and 1,2:5,6-dibenzanthracene.

Characterization of the film from the adamantane seeded silicalites was through electron diffraction and indicated that it was polycrystalline ß-SiC imbedded in an amorphous matrix. Auger electron spectroscopy was performed on a film from an anthracene seeded silicalite. While a surface carbide layer was clearly indicated, it was not possible to identify the film as any single phase. Most likely, the film was again a mixture of crystalline and amorphous phases.

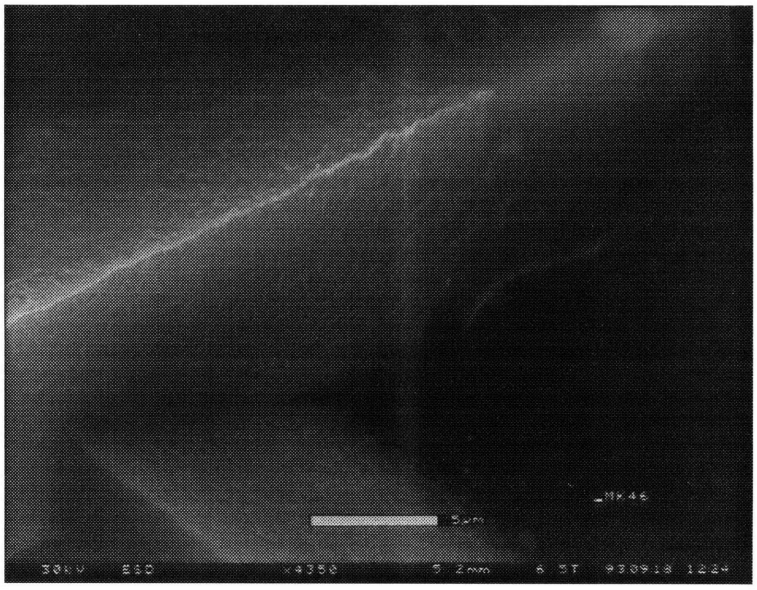

Figure 3-11: SEM of results from anthracene seeded experiments with 0 sccm of acetone initially

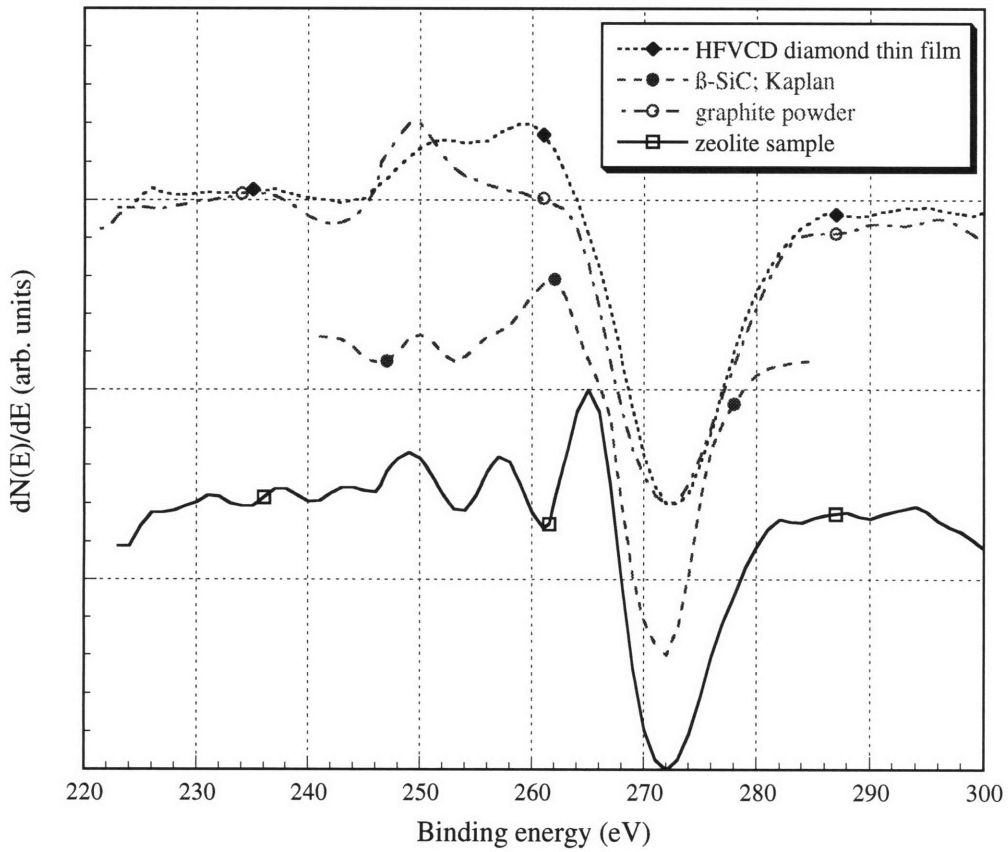

Figure 3-12: Comparison of Auger electron spectra from a HFVCD diamond film, ß-SiC, graphite powder, and the sample in Fig. 3-13

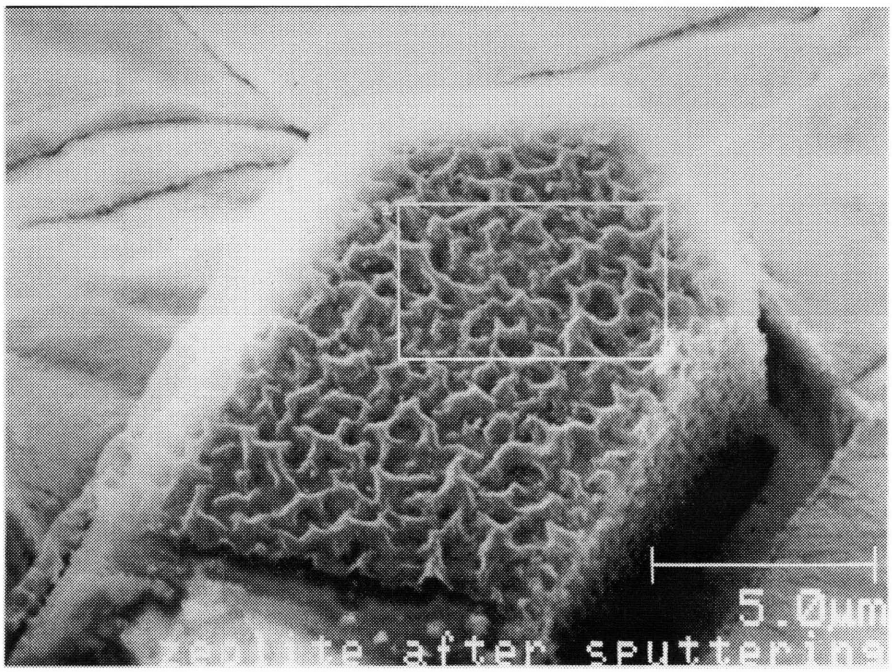

Figure 3-13: Sample whose Auger spectrum is shown in Fig. 3-12.

(Spectrum taken from raster over outlined area.)

In conclusion, the concept of using a molecular scale patterned substrate to control the nucleation of a CVD generated diamond film is still potentially interesting process but would require either a crystalline, nanoporous, non-carbide former as the substrate or the use of a low temperature deposition process to avoid the carbide formation problem in the zeolites.

References:

1. M. W. Geis, H. I. Smith, A. Argoitia, J. Angus, G.-H. M. Ma, J. T. Glass, J. Butler, C. J. Robinson, and R. Pryor, *Appl. Phys. Lett.*, **58** (22), 2485-2487 (1991).
2. R. Spitzl, V. Raiko, R. Heiderhoff, H. Gnaser, and J. Engemann, *Diamond Relat. Mater.*, **4**, 563-568 (1995).
3. W. M. Meir, and D. H. Olson, *Atlas of Zeolite Structure Types*; 2nd ed. Butterworths: London. 1988.
4. S. Matsumoto, and Y. Matsui, *J. Mater. Sci.*, **18**, 1785-1793 (1983).
5. J. C. Angus, Z. Li, M. Sundara, R. Gat, A. B. Anderson, S. P. Mehandru, and M. W. Geis in *2nd International Symposium on Diamond and Diamond Materials*, **vol. 91-8**, 125-141, (1991).
6. Z. Li, L. Wang, T. Suzuki, A. Argoitia, P. Pirouz, and J. C. Angus, *J. Appl. Phys.*, **73** (2), 711-715 (1993).
7. R. Kaplan, *J. Appl. Phys.*, **56** (6), 1636-1641 (1984).

4. SELECTIVE DIAMOND DEPOSITION

Diamond films are technologically interesting because of their high piezoresistivity,[1] thermal conductivity,[2] and low electron affinity.[3] In recent years, selectively deposited diamond films have been demonstrated to be potentially useful as strain sensors,[1] active electronics,[2,4] and cold cathode electron emitters.[3]

Many different researchers have proposed methods to selectively deposit CVD diamond; these can be arbitrarily classified into post-lithography and pre-lithography nucleation techniques. The former category includes methods that induce diamond nucleation by using SiO_2 or Si_3N_4 as a mask for either ultrasonic scratching with a diamond suspension [5,6] or ion implantation followed by a wet etch of the undamaged silicon overlayer.[7] A variation on this theme is to use negative bias-enhanced nucleation on an unscratched, masked/patterned substrate.[8,9] The pre-lithography category includes methods that first ultrasonically scratch the wafer to induce nucleation and then deposit diamond with a photolithographically patterned mask composed of SiO_2 [6] or yttria-stabilized zirconia [10] on top of the wafer. This category also encompasses those techniques that use a laser [11] or reactive ion etching [12] to selectively remove the effects of scratch nucleation prior to deposition. The main goal for all of these workers is to selectively deposit more highly resolved features and to improve cleanliness in the non-growth regions; i.e., achieve higher selectivity.

This letter presents a variation of the post-lithography nucleation technique that demonstrates high selectivity and good feature resolution. A post-lithography nucleation

step was chosen because of the difficulties in removing the effects of diamond scratching or ion implantation on a silicon wafer when using a pre-lithography technique.

4.1 Experimental description

The selective deposition process is schematically shown in Figure 4-1. To begin, a resist pattern was placed onto four inch silicon (100) wafers using a 0.6 μm photolithographic process. The die pattern, shown schematically in Figure 4-2, measured 11 mm x 11 mm and was composed of a series of 3000 μm long parallel lines spaced from 7 to 290 μm apart, a set of concentric rings with radii from 5 to 2800 μm, and several square arrays of dots on 10 to 200 μm centers. Chromium metal was then deposited onto the patterned wafer to a thickness of 1300 Å via electron beam evaporation; thicker films can not be used because of cracking and delamination problems. The chrome was completely lifted off in acetone with ultrasonic agitation, leaving a chrome mask with openings to the silicon substrate underneath. Nucleation was preferentially induced by scratching the wafer in an acetone suspension of 0-0.5 μm natural diamond powder in an ultrasonic cleaner. After rinsing in a high pressure stream of high purity de-ionized water, the chrome is chemically removed by spraying with a $(NH_4)_2Ce(NO_3)_6$ / HNO_3 solution for 2 minutes. The wafer is then rinsed again in de-ionized water and dried with nitrogen. The repeated de-ionized water rinsings are critical to ensure that there is a minimal of residual diamond transferred to the areas where diamond growth is not desired. Scanning electron microscopy shows that prior to deposition there are no traces of the diamond scratching or the chrome mask down to 0.1 μm resolution.

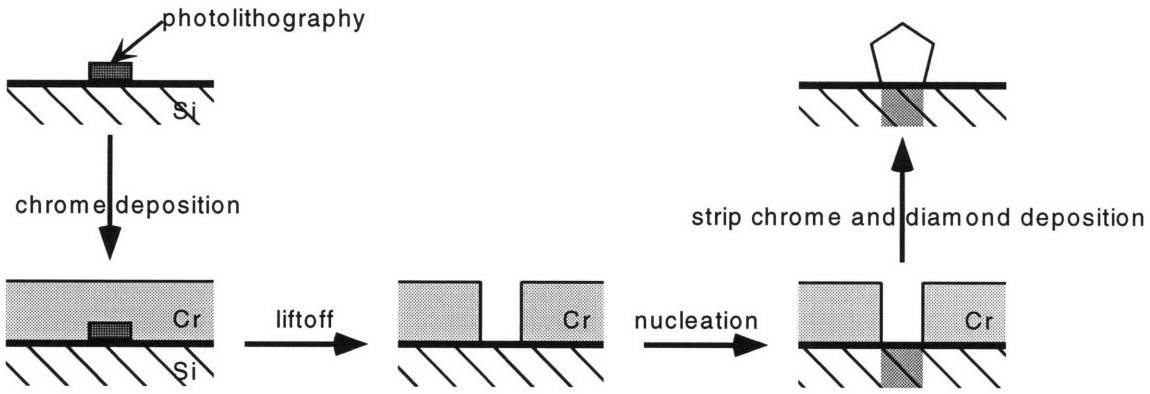

Figure 4-1: Schematic of selective diamond nucleation process

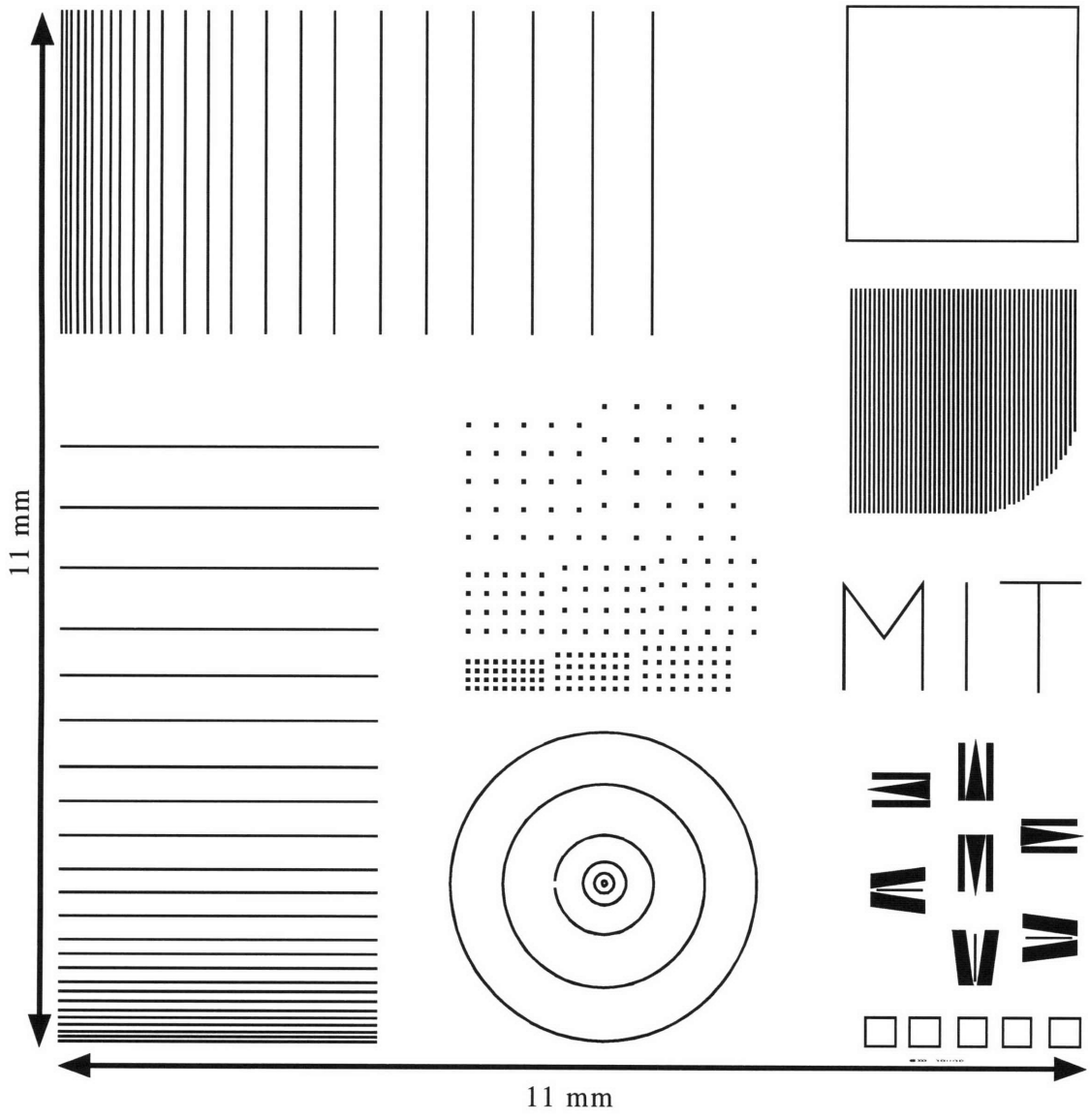

Figure 4-2: Schematic of mask for selective diamond nucleation

Finally, diamond is deposited on the selectively nucleated substrate using a single hot tantalum filament, chemical vapor deposition technique. The reactor pressure is 20 Torr, and typical gas flowrates are 150 sccm of H_2 and 1.7 sccm of acetone. The substrate temperature is monitored through a chromel-alumel thermocouple contacting the backside of the wafer and is typically between 650 - 700 °C.

4.2 Results and discussion

Figure 4-3 shows a low magnification scanning electron micrograph of a selectively deposited diamond pattern after 30 minutes of deposition, demonstrating the high degree of selectivity. The nucleation density on the masked areas where deposition is undesired is on the order of 10^5 cm^{-2} versus 10^8 cm^{-2} on the scratch nucleated areas; a pristine wafer will have a nucleation density of approximately 10^3 cm^{-2}. Figures 4-4 through 4-6 demonstrate the resolution of this method. The set of concentric circles are all about 2 μm wide with the smallest edge-to-edge separation between the central dot and the first circle being about 2.5 μm. The break in the third ring from the center was actually due to a mask defect which transfered in the nucleation process. The line of diamond particles is roughly 3000 μm long by 1 μm wide with the smallest edge-to-edge separation between lines being 5 μm while the square array of 1 μm crystals is on 10 μm centers and covers approximately 900 μm by 400 μm.

One possible application for such a well-ordered array of diamond crystals is in the control of the final morphology / texture of polycrystalline films. Large-area mosaic films that approach single crystal quality have been grown from a regular array of 100 μm diamond seeds sitting in Si etch pits [13]. By selectively depositing on a much more closely

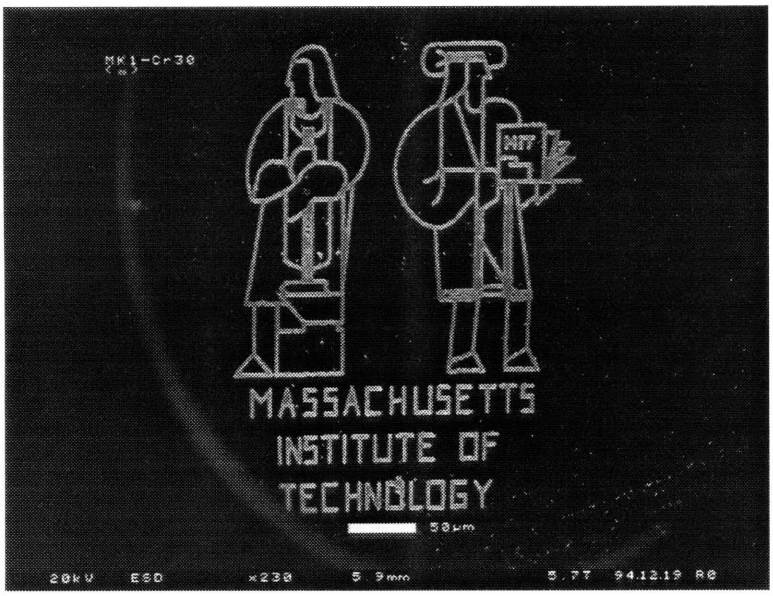

Figure 4-3: Example of diamond nucleation selectivity

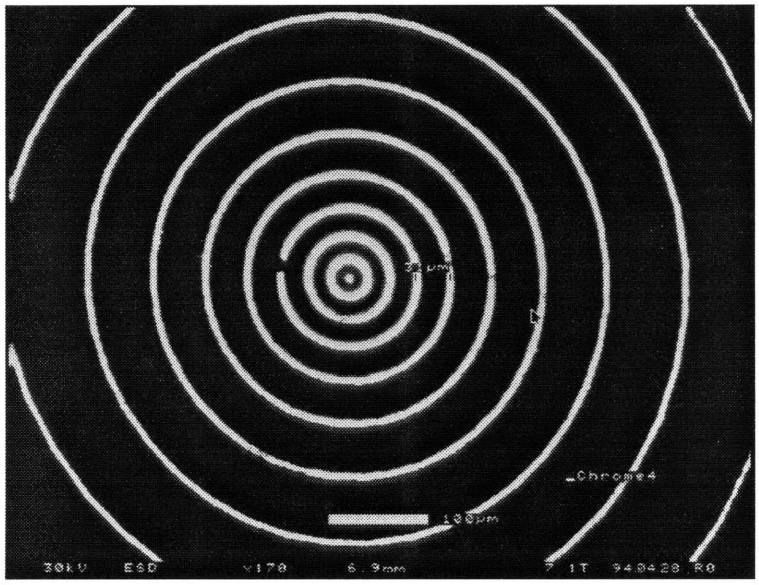

Figure 4-4: Selectively deposited concentric circles of diamond crystals

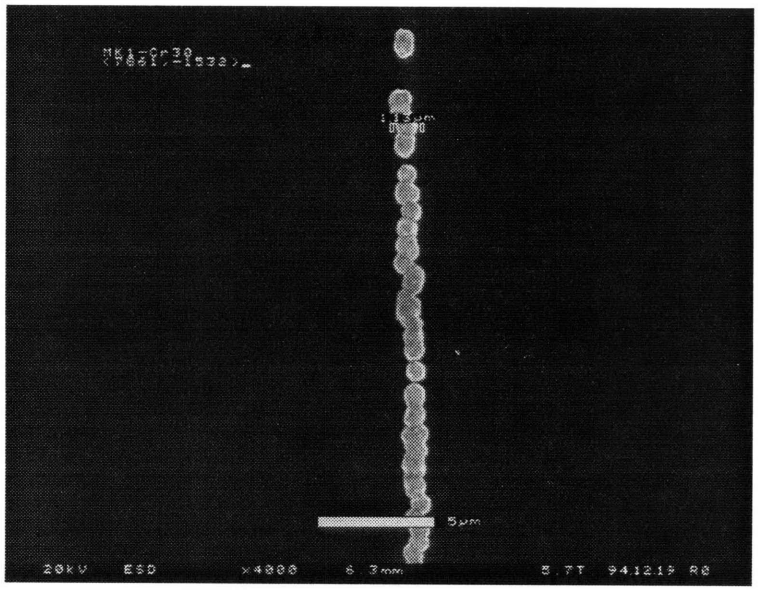

Figure 4-5: Selectively deposited row of diamond particles

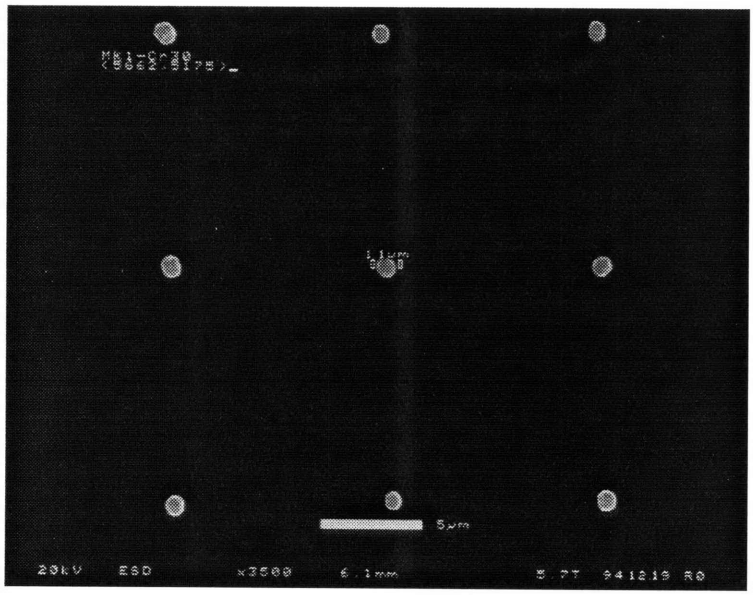

Figure 4-6: Selectively deposited square array of diamond particles

spaced array under growth conditions that lead to a preferred growth orientation, it may be possible to form a mosaic-type film which coalesces more quickly into a smooth film whose surface layer approaches single crystal quality.

In closing, the good resolution of this selective deposition method can be attributed to the use of a relatively thin masking layer and small diamond particles while the high selectivity is likely due to the higher fracture toughness of chromium as compared to SiO_2 and Si_3N_4. (Metals typically have fracture toughnesses that are 1-2 orders of magnitude higher than Si_3N_4 at 4.5 MPa$\bullet\sqrt{m}$.) The higher fracture toughness of chromium coupled with its hardness makes for a wear resistant coating that is not worn away or fractured by ultrasonic scratching as other materials are [6] and therefore excellent as a mask for use in selective diamond deposition.

References:

1. M. Aslam, I. Taher, A. Masood, M. A. Tamor, and T. J. Potter, *Appl. Phys. Lett.*, **60** (23), 2923 (1992).
2. M. W. Geis, N. N. Efremow, and D. D. Rathman, *J. Vac. Sci. Technol. A*, **6** (3), 1953-1954 (1988).
3. K. Okano, K. Hoshina, and M. Iida, *Appl. Phys. Lett.*, **64** (20), 2742-2744 (1994).
4. S. A. Grot, G. S. Gildenblat, and A. R. Badzian, *IEEE Electron Device Lett.*, **13** (9), 462-464 (1992).
5. C. F. Chen, S. H. Chen, T. M. Hong, and M. H. Tsai, *J. Appl. Phys.*, **77** (2), 940-942 (1995).
6. A. Masood, M. Aslam, M. A. Tamor, and T. J. Potter, *J. Electrochem. Soc.*, **138** (11), L67-L68 (1991).
7. S. J. Lin, S. L. Lee, J. Hwang, and T. S. Lin, *J. Electrochem. Soc.*, **139** (11), 3255-3258 (1992).
8. S. Katsumata, and S. Yugo, *Diamond Relat. Mater.*, **2** (12), 1490-1492 (1993).
9. O. Auciello, R. Spitzl, and J. Engemann in *Third International Conference on Applications of Diamond Films and Related Materials*, ed. by A. Feldman, Y. Tzeng, W. A. Yarbrough, M. Yoshikawa, and M. Murakawa, 65-68, (1995).
10. T. Maki, G. L. Hou, and T. Kobayashi, *Jpn. J. Appl. Phys.*, **32**, 3227-3230 (1993).
11. J. Narayan, and X. Chen, *J. Appl. Phys.*, **71** (8), 3795-3801 (1992).
12. T. Inoue, H. Tachibana, K. Kumagai, K. Miyata, K. Nishimura, K. Kobashi, and A. Nakaue, *J. Appl. Phys.*, **67** (12), 7329-7336 (1990).
13. M. W. Geis, H. I. Smith, A. Argoitia, J. Angus, G.-H. M. Ma, J. T. Glass, J. Butler, C. J. Robinson, and R. Pryor, *Appl. Phys. Lett.*, **58** (22), 2485-2487 (1991).

5. MODELING OF SELECTIVE DIAMOND DEPOSITION

A thin film chemical vapor deposition (CVD) process can be generally thought of as being composed of several underlying, coupled processes; namely, growth species generation, gas phase diffusion, homogeneous gas phase chemistry, and heterogeneous chemistry at the growing surface. In diamond CVD, considerable effort has been devoted to studying these processes in the hope of achieving faster growth rates of high quality diamond. Since the gas phase phenomena can be addressed through the large body of literature on hydrocarbon combustion,[1] many researchers have concentrated on understanding the surface kinetics of diamond growth. The proposed mechanisms typically postulate that atomic hydrogen,[2] methyl radical,[3] and/or acetylene[4] are the growth limiting species. However, the coupled behavior of these processes, particularly the interaction of gas phase transport and surface reaction, has not been extensively studied. Goodwin and Gavillet included homogeneous reactions and diffusion in their model of the HFCVD environment.[5] However, because of the computational complexity of the gas phase chemistry and fluid mechanics, they were forced to use a one-dimensional model with a simple fitted carbon incorporation fraction at the surface. Frenklach and Wang modeled diamond deposition in a similar one dimensional fashion but with highly detailed kinetics, including surface reactions that were treated similarly to gas phase analogs.[1] In addition, they assumed that the gas phase concentrations of chemical species were unaffected by their consumption or production in the surface reactions, thereby decoupling the gas phase and the surface reactions. While these approaches may give insight into the nature of the

gas phase, they do not focus on the full dimensionality of the diffusion problem nor its relationship to the surface kinetics.

Recognizing the importance of the surface kinetics, work using time-of-flight ion scattering and recoil spectroscopy[6] and photoionization mass spectrometry[7] have measured the surface kinetics for H-atom adsorption, desorption, and abstraction. However, these surface kinetics studies were not done in an actual diamond CVD system. Recently, Connell *et al.* measured the hydrogen atom concentration in a hot filament deposition system with an optical technique using third-harmonic generation and showed that the observed gas phase concentration can be explained by including the loss of H-atoms at the diamond surface, demonstrating the coupled nature of the system.[8] Likewise, Chen *et al.* have also measured H-atom concentrations in a HFCVD system by coherent anti-Stokes Raman scattering,[9] but like the work of Connell *et al.*, they made no attempt to correlate their growth rate with the spectroscopic results to see if changes in the H-atom concentration had a directly measurable effect on the growth rate.

By studying an actual CVD reactor and, specifically, how the coupling of surface kinetic and transport processes affect the growth rates, we aim to quantify their relative importance in a setting directly relevant to our goal of faster deposition rates. This quantitation will hopefully allow others to intelligently target processing or design changes to debottleneck the diamond deposition process. We will also attempt to distinguish between the dominance of hydrogen atoms versus methyl radicals in the growth of CVD diamond.

Building on the spectroscopic data of others, we will measure and model the effect of continuously varying local substrate loading on the growth rate. It has been pointed out

that diamond HFCVD is a diffusion-controlled system;[2,9] such an effect should therefore be observable. The selectively deposited diamond films discussed in the last chapter provide an excellent starting point because the density of growth already varies spatially across the substrate and hence could exhibit differences in growth rate as a function of substrate loading.

5.1 Small length scale selective deposition

Based on scanning electron microscopy of the selectively deposited lines of diamond in Chapter 4, it was generally observed that the growth rates of adjacent lines did not vary as the spacing between the lines was changed from 2 μm to 250 μm. (See Fig. 4-2 for mask schematic.) In order to gain some insight into the physical processes that were occuring, a simple two dimensional mass transport plus reaction model was developed. To start with, the hot-filament was assumed to provide a steady source of growth precursors. This assumption would require that the heterogeneous reactions at the filament surface which generate the precursors be fast relative to the lost mechanisms; i.e., reaction and transport. Meier, *et al.* have measured H-atom concentration of $3x10^{15}$ cm^{-3} around a hot Ta filament in 30 mbar of H_2 by laser induced fluorescence.[10] The addition of methane reduced this by more than 30%.[11] Yet others have measured the mole fraction of CH_3 to be from 10^{-3} to 10^{-4} or approximately 10^{14} to 10^{13} cm^{-3} at 20 Torr. Following generation, the precursor molecules are transported away from the filament by three dimensional Fickian diffusion. If the molar density of the gas is constant and there is a zero net velocity, then the diffusion equation can be written

$$\frac{\partial C_A}{\partial t} = D_{AB} \nabla^2 C_A \qquad (5\text{-}1)$$

Therefore at steady state, $\nabla^2 C_A = 0$. When a molecule diffuses to the surface, it can react in a number of ways. For atomic hydrogen, the dominant reactions are surface hydrogen abstraction and surface site termination;[12] i.e.,

$$CH_{surf} + H \xrightarrow{k_1} C^*_{surf} + H_2 \qquad (5\text{-}2)$$

$$C^*_{surf} + H \xrightarrow{k_2} CH_{surf} \qquad (5\text{-}3)$$

Following the development of Dandy *et al.*,[12] a mass balance at the surface between the flux of H to the surface and its rate of disappearance due to reaction gives:

$$-D \frac{d[H]}{dz} = -k_1 [CH_{surf}][H] - k_2 [C^*_{surf}][H] \qquad (5\text{-}4)$$

where $[CH_{surf}]$ is the density of hydrogen terminated diamond surface sites
$[C^*_{surf}]$ is the density of open surface sites

Assuming that the surface is at steady state, the concentration of the two surface species can be related to one another by:

$$[C^*_{surf}] = \frac{k_1}{k_2} [CH_{surf}] \qquad (5\text{-}5)$$

and to the total site density, Γ, by

$$\Gamma = [C^*_{surf}] + [CH_{surf}] \qquad (5\text{-}6)$$

Wolden has shown using a steady state analysis with sixteen reactions instead of the two used here that 99.9% of the surface sites are indeed tied up in our two species.[13] Combining Eqn 5-4, 5-5, and 5-6, we arrive at a first order rate expression in [H]

$$-D \frac{d[H]}{dz} = -\frac{2 k_1 k_2}{k_1 + k_2} \Gamma [H] = -k_s [H] \qquad (5\text{-}7)$$

where $k_s = \frac{2 k_1 k_2}{k_1 + k_2} \Gamma$ is a pseudo first order rate constant

Note that for, $k_2 >> k_1$, $k_s \approx 2 k_1 \Gamma$.

Figure 5-1 defines the geometry and boundary conditions of the model. To simulate the deposition over a surface with an infinite number of very long, evenly spaced lines, the x-direction boundary conditions were periodic. Following our assumptions, the concentration at $z=d_{fs}$ (filament level) is constant while the boundary at z=0 (wafer surface) is a no-flux one off of the diamond line and a first order reaction on it.

The diffusion equation was solved by the finite-difference method. (For details, see section 5.3.2) The result for $k_m = k_s/D = 100$ cm^{-1} was that the concentration was not a function of x; as D increased, smaller values of k_m would give the same results. In fact, for $k_m = 100$ cm^{-1}, the surface of the wafer could be changed from an infinite number of lines of width *w* μm on *S* μm centers to lines of width *w*/4 μm on *S*/4 μm centers without affecting the simulation result at all. In trying to extend this idea to the limit of infinitesimally small lines separated by infinitesimally small spacings, the finite difference model was compared with the one-dimensional analytical model with a surface coverage weighted reaction coefficient. Figure 5-2 shows a diagram of the 1D analog to our 2D problem. The equations which relate C_0, the constant concentration outside of the concentration boundary layer; C_s, the surface concentration; k_s, the first order surface reaction coefficient; D, the gas phase diffusion coefficient; and L, the boundary layer thickness, in this case are

$$r = k_s C_s \text{ [=] cm}^{-2}\text{ s}^{-1} \tag{5-8}$$

$$r = D \left.\frac{dC}{dx}\right|_{x=0} = \frac{D}{L}(C_0 - C_s) \tag{5-9}$$

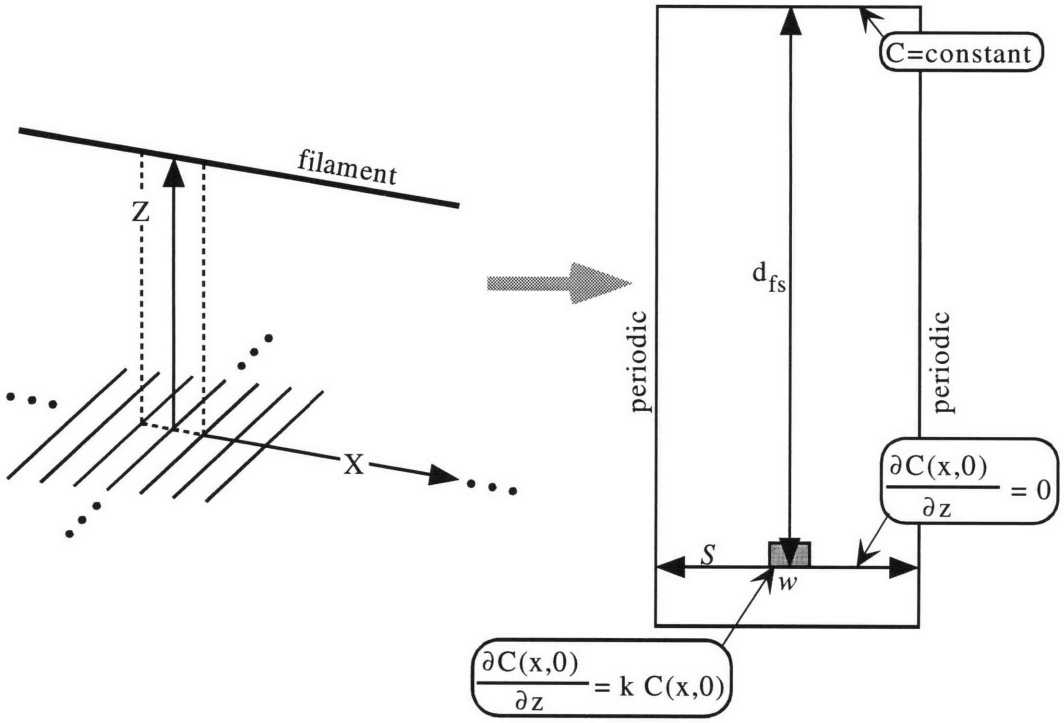

Figure 5-1: Problem definition and boundary conditions for the short length scale, 2-D diamond growth modeling on an infinite array of lines

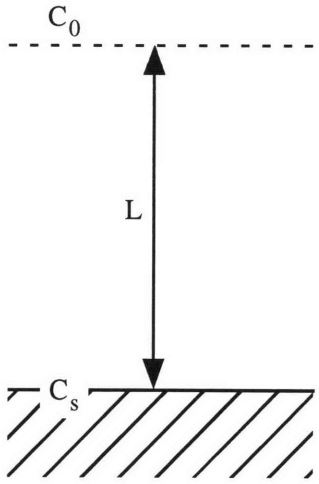

Figure 5-2: 1-D analogy to the 2-D diffusion/surface reaction model

Rearranging Eqn. 5-8 and 5-9 to eliminate C_s, we arrive at

$$r = \frac{D}{L}\left(C_0 - \frac{r}{k_s}\right) \tag{5-10}$$

$$r\left(1 + \frac{D}{L\,k_s}\right) = \frac{DC_0}{L} \tag{5-11}$$

$$r = \frac{k_s\,D\,C_0}{L\,k_s + D} = \frac{k_s\,C_0}{Da + 1} \tag{5-12}$$

where $Da = \frac{L\,ks}{D}$ = Damköhler number

Stated another way, Eqn. 5-8 and 5-12 tell us that $\frac{C_s}{C_0} = \frac{1}{\frac{d_{fs}\,k'}{D} + 1}$ where $L = d_{fs}$ (diffusion boundary layer thickness is filament-to-substrate spacing) and $k' = (w/S)k_s$ is the surface coverage weighted reaction coefficient. The model results for a variety of line width to spacing ratios of *w/S* are compared with the modified analytical solution for k_m = 100 cm^{-1} in Figure 5-3. The match between the finite difference result and the modified analytical solution implies that over several hundred microns, diffusion acts to average out the effect of any selectively nucleated deposits; therefore, for simulation purposes, the array of lines from the mask in Chapter 4 can be represented by a relatively small number of elements, each with a different surface coverage averaged reaction coefficient. One such possible representation is shown schematically in Figure 5-4.

5.2 Large length scale selective deposition process

Since the analysis at short length scales indicated that changes to the substrate loading at up to several hundred microns were averaged out, we moved on to study diamond growth on larger scale, selectively nucleated deposition.

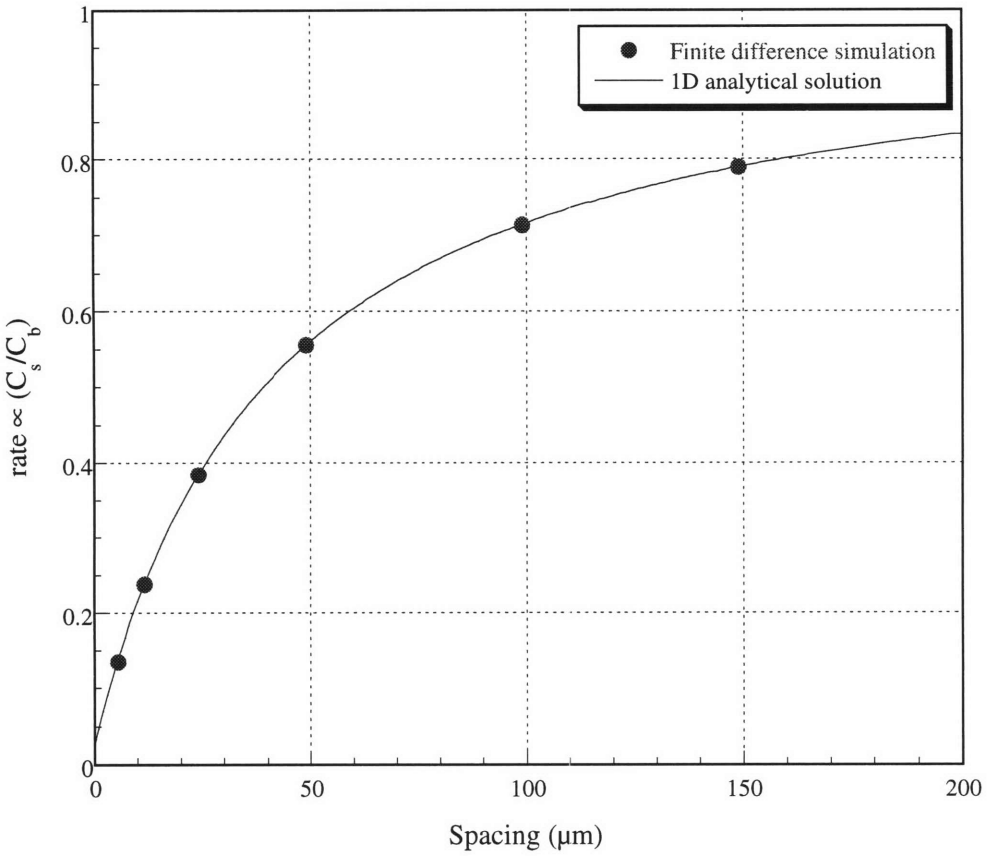

Figure 5-3: Comparison of the 1-D analytical model (Fig. 5-2) with a modified reaction coefficient to the finite difference model for a range of line spacings

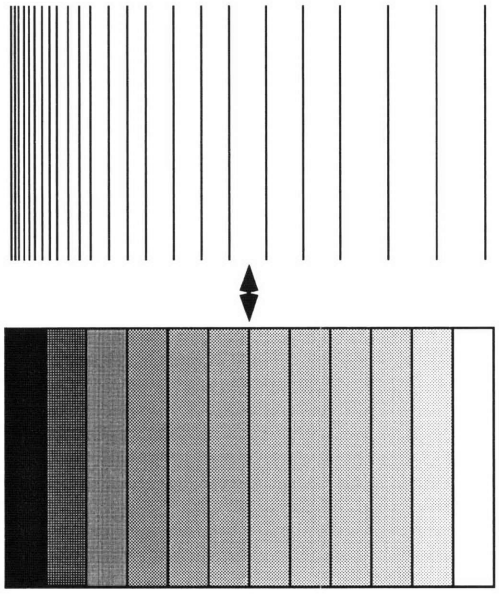

Figure 5-4: Grayscale representation of a selectively deposited diamond film

Figure 5-5 shows a schematic of a typical patterned deposition. Deposition occurs along a band under the single straight filament except for a 25 mm by 12.5 mm diamond shaped region which was exposed to the O_2 plasma. In addition, there is a 100 μm wide line of deposition along the long axis of the diamond-shaped window that was masked from the plasma. This pattern is similar to one used to study tapered structures in InP/InGaAs growth.[14] The idea is that nuclei at the two ends of the 100 μm wide median line will experience a different local gas-phase environment from nuclei in the center of the line and that this difference will yield information on the relative importance of diffusion in controlling the growth rate.

The selective depositions were performed with the hot filament chemical vapor deposition (HFCVD) system described in Chapter 2 with hydrogen and acetone as the feed gases. The gases were activated with a single straight tantalum filament. Typical depositions were carried out at 20 torr of pressure and a substrate temperature of 680 °C with gas feeds of 150 sccm of H_2 and 1.5 sccm of acetone. The substrates were 2 inch (100) p-type silicon wafers that had been pre-nucleated by ultrasonic scratching in a suspension of 0.5 μm diamond powder. In order to deposit diamond selectively, the wafers were masked with a copper template and then etched in a parallel plate plasma asher for 10 minutes (100 mtorr O_2, 100 W). Because the oxygen plasma etches away the diamond nuclei in those areas not masked by the template, nucleation densities in the exposed regions are several orders of magnitude below that in the covered regions.

Figure 5-6 is a scanning electron micrograph from a typical 1 hour deposition. By digitizing such pictures which cover about 50 x 38 μm^2 with a desktop scanner or a CCD camera, we can use image analysis software to electronically measure the area covered by

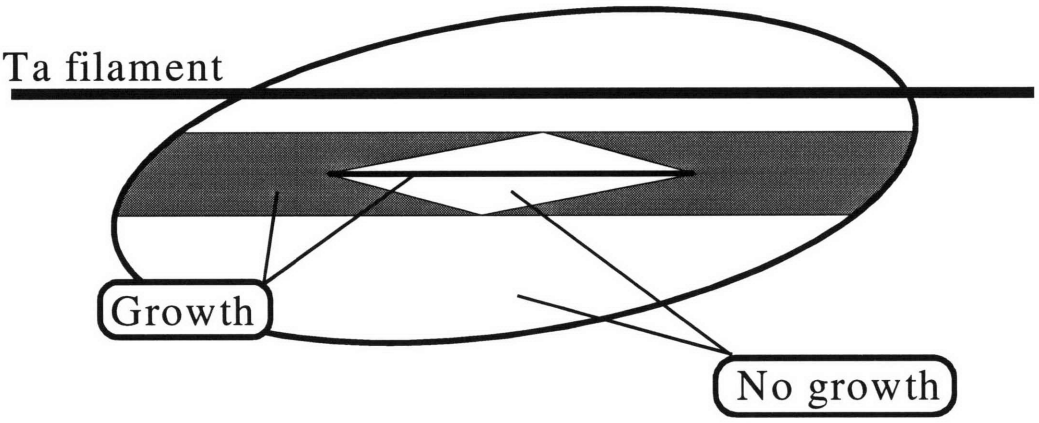

Figure 5-5: Typical patterned deposition

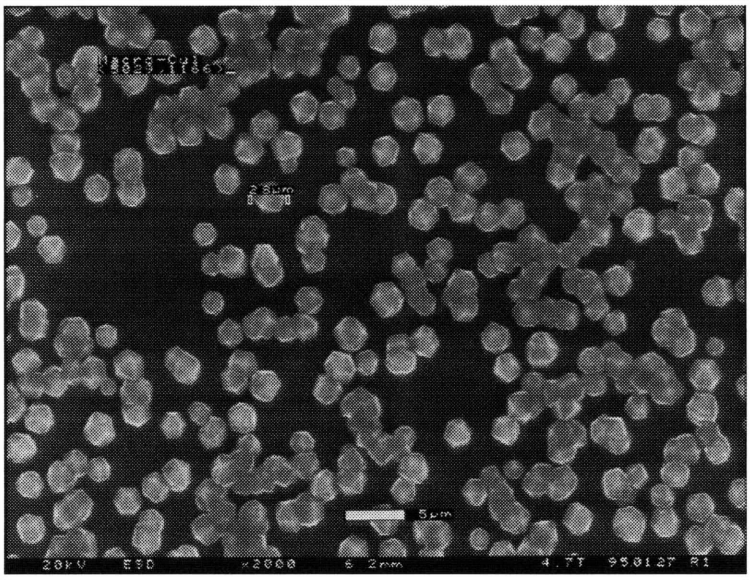

Figure 5-6: SEM of a typical 1 hr deposition

diamond growth and hence calculate the relative growth rate between various regions on the substrate. This approach is valid since our results from the short length scale experiments showed that the growth rate of a several hundred micron region can be taken as an aggregrate. It is also preferred to bulk thickness measurements on thick films grown over 24 hours because of the innate instability of the filament; a 1 mm sag in the filament would make modeling and analysis impossible.

The image analysis process begins by calibrating the size of a pixel based on the bar on the micrograph. The digital images are then run through a thresholding process so that all of the pixels above or below a certain threshold gray level are set to black. If done correctly to a picture with a not overly high level of contrast, this will give a partially filled black outline of all the diamond particles. After some manipulation to fill in the unfilled outlines and remove extraneous noise, the image analysis software can then measure the total area that is black. A typical particle or clump of particles will be made of at least several hundred pixels and have an error of about 10% from the thresholding and filling process. The resulting data set will usually have a number of small "dust flecks" with $< 0.5\%$ of the area of the actual particles that are discarded.

Four electron micrographs were taken from each of the three areas on a selectively deposited wafer as shown schematically in Figure 5-7. The points sampled were at the two ends of the line running through the center of the diamond shaped window (points A and C) and in the center of the line (point B). For reference, a similar set of micrographs were taken from the same three spots on an unpatterned control wafer. The image analysis results of the amount of diamond growth in each region for both samples are listed in Table 5-1. A statistical analysis of the data with a t-test showed that, at a 99.9% confidence level,

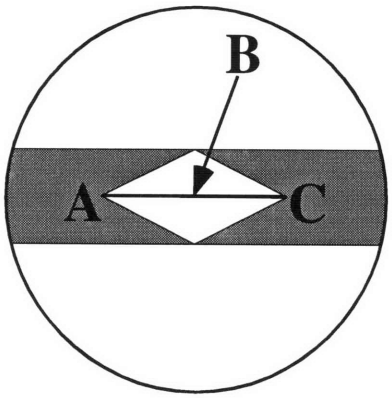

Figure 5-7: Points sampled for diamond growth rate variation analysis (Tab. 5-1)

the difference in the mean diamond coverage fraction across the unpatterned wafer was statistically insignificant. The differences in mean coverage fraction between the center and the ends of the pattern on the selectively deposited wafer, however, were significant. If one assumes that the linear growth rate is proportional to the square root of the area fraction, then the growth rate in the center of the patterned wafer is 2 ± 0.3 times faster than at the two ends of the diamond pattern.

Table 5-1: Variation in diamond coverage fraction at several locations on an unpatterned and a patterned Si wafer. See Fig.5-7.

Sample region	Diamond fraction	stnd dev.	$\sqrt{\text{diamond fraction}}$	stnd dev.
A, unpatterned	0.051	0.014	0.227	0.031
B, unpatterned	0.059	0.014	0.243	0.029
C, unpatterned	0.074	0.021	0.272	0.039
A, patterned	0.049	0.011	0.221	0.025
B, patterned	0.204	0.038	0.452	0.042
C, patterned	0.045	0.004	0.213	0.009

5.3 Diffusion/surface reaction model

5.3.1 Model description

To model the variation in growth rate along the center line directly beneath the filament, we again used a version of the mass transport plus reaction model that was described in section 5.1. The assumptions and general model description remain the same.

5.3.2 Finite difference approach

In order to solve the diffusion and growth model, the finite difference method was used because it was relatively simple to implement but yet could capture the complex geometries and discontinuous boundary conditions in our system. The method discretizes the region of interest and solves the linear, finite difference representation of the governing equation at each point. In one dimension f "(x) can be approximated by truncating the Taylor series expansion of f about x; i.e.,

$$f(x+h) = f(x) + h\,f'(x) + \frac{h^2}{2} f''(x) + \frac{h^3}{6} f'''(x) + \ldots \qquad (5\text{-}13)$$

$$f(x-h) = f(x) - h\,f'(x) + \frac{h^2}{2} f''(x) - \frac{h^3}{6} f'''(x) + \ldots \qquad (5\text{-}14)$$

$$f''(x) = \frac{1}{h^2}\{f(x+h) + f(x-h) - 2\,f(x)\} + O_{err}(h^4) \qquad (5\text{-}15)$$

If we represent f(x) at each point of our discretized region by f_{ijk}, where i, j, & k are indices for each of the three coordinates, then in order for $\nabla^2 C_A = 0$ to be true throughout the region, $\nabla^2 C_{ijk} = 0$ must also be true for all i, j, k. Using the three dimensional analog to Eqn. 5-15, the diffusion equation at a particular grid point becomes

$$\frac{1}{h_i^2}(C_{i+1,j,k} - 2\,C_{ijk} + C_{i-1,j,k}) + \frac{1}{h_j^2}(C_{i,j+1,k} - 2\,C_{ijk} + C_{i,j-1,k}) + \frac{1}{h_k^2}(C_{i,j,k+1} - 2\,C_{ijk} + C_{i,j,k-1}) \qquad (5\text{-}16)$$

where h_m = grid spacing in the m-direction, where m = i, j, k (see Fig. 5-8)

The three possible boundary conditions are constant concentration, no-flux ($\frac{\partial C}{\partial x} = 0$) and a first order reaction ($\frac{\partial C}{\partial x} = k_s C$). The constant concentration boundary condition was simply accounted for by fixing the relevant C_{ijk}. The no-flux and first order reaction boundary conditions were again approximated by a truncation of the Taylor series expansion; the two-sided difference equation is give by:

$$f'(x) = \frac{f(x + h) - f(x - h)}{2h} + O_{err}(h^3) \tag{5-17}$$

The no-flux condition was therefore expressed by

$$\frac{C(x + h) - C(x - h)}{2h} = 0 \tag{5-18}$$

while the first order reaction was represented by

$$\frac{C(x + h) - C(x - h)}{2h} = k\,C(x) \tag{5-19}$$

As a specific example, if C_{ijk} is a point on the +i-coordinate boundary, then the diffusion equation at C_{ijk} is given by Eqn. 5-16. Because we are at the +i-boundary, $C_{i+1,j,k}$ is a phantom point outside of our simulation region. For a no-flux boundary condition in the i-direction, $C_{i+1,j,k} = C_{i-1,j,k}$ and the diffusion equation becomes

$$\frac{1}{h_i^2}(2\,C_{i-1,j,k} - 2\,C_{ijk}) + \frac{1}{h_j^2}(C_{i,j+1,k} - 2\,C_{ijk} + C_{i,j-1,k}) + \frac{1}{h_k^2}(C_{i,j,k+1} - 2\,C_{ijk} + C_{i,j,k-1}) \tag{5-20}$$

For a first order reaction to occur at C_{ijk}, $C_{i+1,j,k} = C_{i-1,j,k} + 2\,h_i\,k\,C_{ijk}$. In which case, the diffusion equation becomes

$$\frac{1}{h_i^2}(2\,C_{i-1,j,k} - 2(1 - h_i\,k)C_{ijk}) + \frac{1}{h_j^2}(C_{i,j+1,k} - 2\,C_{ijk} + C_{i,j-1,k}) + \frac{1}{h_k^2}(C_{i,j,k+1} - 2\,C_{ijk} + C_{i,j,k-1}) \tag{5-21}$$

For a region that has been discretized into n x m x l points, there will be nml linear equations in nml variables that must be solved simultaneously. The equations in matrix form, $\underline{\mathbf{A}}\mathbf{x} = \mathbf{b}$, can be solved by inverting $\underline{\mathbf{A}}$ to give $\mathbf{x}$, the concentration at all the points in the modeled volume. Because Eqns. 5-16, 5-20, and 5-21 have, at most, seven terms in them each, $\underline{\mathbf{A}}$ will be a sparse matrix; i.e., composed of mostly zeros. In particular, $\underline{\mathbf{A}}$ will be a band diagonal matrix with a main diagonal of smaller sub-matrices plus two off-diagonal bands and zeros everywhere else. We can use indexing techniques to take advantage of $\underline{\mathbf{A}}$'s sparseness and reduce the amount of memory needed to store a given problem which, in turn, will allow us to increase the grid fineness (number of grid points) and the computational speed. Without such an insight, the problem would quickly become untractable. A 50 x 50 x 50 spatial grid has 125,000 elements which would consume $8*(1.25x10^5)^2$ = 125 gigabytes of computer memory just to store, an amount which is currently unfeasible. In a sparse indexed format, $\underline{\mathbf{A}}$ for a 50^3 element problem would require about $13*(7*1.25x10^5)$ = 11.4 megabytes of memory to store - four orders of magnitude less than the full matrix.

5.3.3 Results

Figure 5-9 displays a schematic of the discretization of a quarter of the volume between the filament and the substrate surface along with the appropriate boundary conditions. The remaining three-fourths were obtained by symmetry; the boundary conditions at the two mirror planes were no-flux ones. As discussed in the model description section, the concentration at the filament was fixed at C_f and as a rough approximation, set equal to $3x10^{15}$ cm^{-3}. The remainder of the points at the z=L (filament

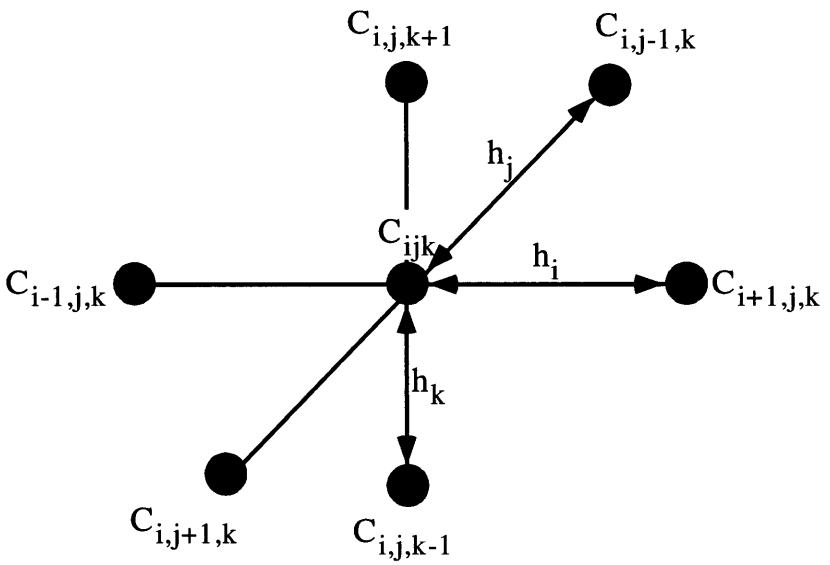

Figure 5-8: Definition of terms used in the 3-dimensional finite difference diffusion/reaction model

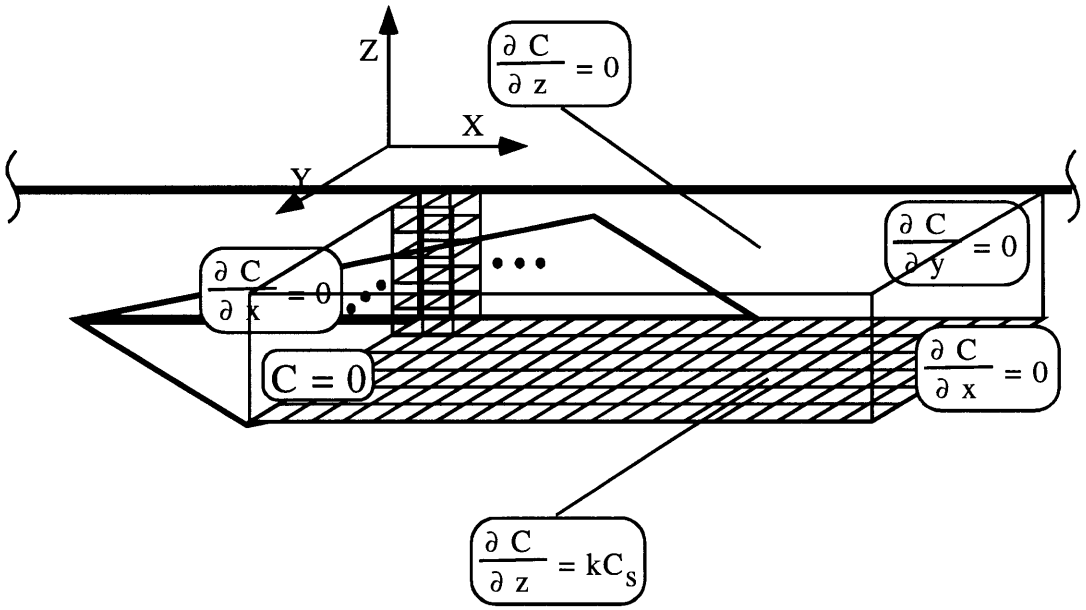

Figure 5-9: Schematic of the discretization of the simulation volume.

A typical volume includes 3240 grid points and encompasses 22.5x6x3 mm^3.

height) boundary have no-flux conditions on them because of symmetry while the boundary at z=0 (wafer surface) varies depending on whether or not a reaction is occurring at that point. Based on the short length scale simulation results, we will apply a grayscale averaging to smooth the transition between regions of high and low nucleation, eliminating discontinuous boundaries. If the entire area represented by a grid point is covered by a high density of diamond growth ($>10^8$ cm^{-2}), then the boundary condition at that point is simply $\frac{\partial C}{\partial z} = k_s C_s$. A no-flux condition is imposed (i.e., no reaction) if only a nearly background level of diamond growth is seen ($<10^4$ cm^{-2}). If only part of the area represented by a grid point has a high level of diamond nucleation, then the flux at that point is linearly scaled by the fraction of the area covered by diamond; i.e., if half the area represented by grid point is heavily nucleated then the reaction at that point is represented by $\frac{\partial C}{\partial z} = ½ * k_s C_s$. The filament and wafer were considered to extend for a long distance in the x-direction past the ends of the simulation. For this reason, the x-direction boundary condition was a no-flux one. The y-direction boundary condition was set to zero. In this case it was because the experimentally measured growth rate drops off at these boundaries. To check the sensitivity of the simulation to this proposed boundary condition, an analysis was conducted by moving the y-direction boundaries further out and examining the effect on the simulation results.

A plot of C_s, the simulated gas phase concentration at the wafer surface, for P = 20 torr, k_m = 10 cm^{-1}, $C_f = 3x10^{15}$ cm^{-3}, d_{fs} = 3 mm over a 22.5 mm long by 6 mm wide by 3 mm high volume which has been discretized at a grid spacing of 0.5 mm is shown in Figure 5-10. Since the growth rate was assumed to proportional to C_s, the graph in Figure

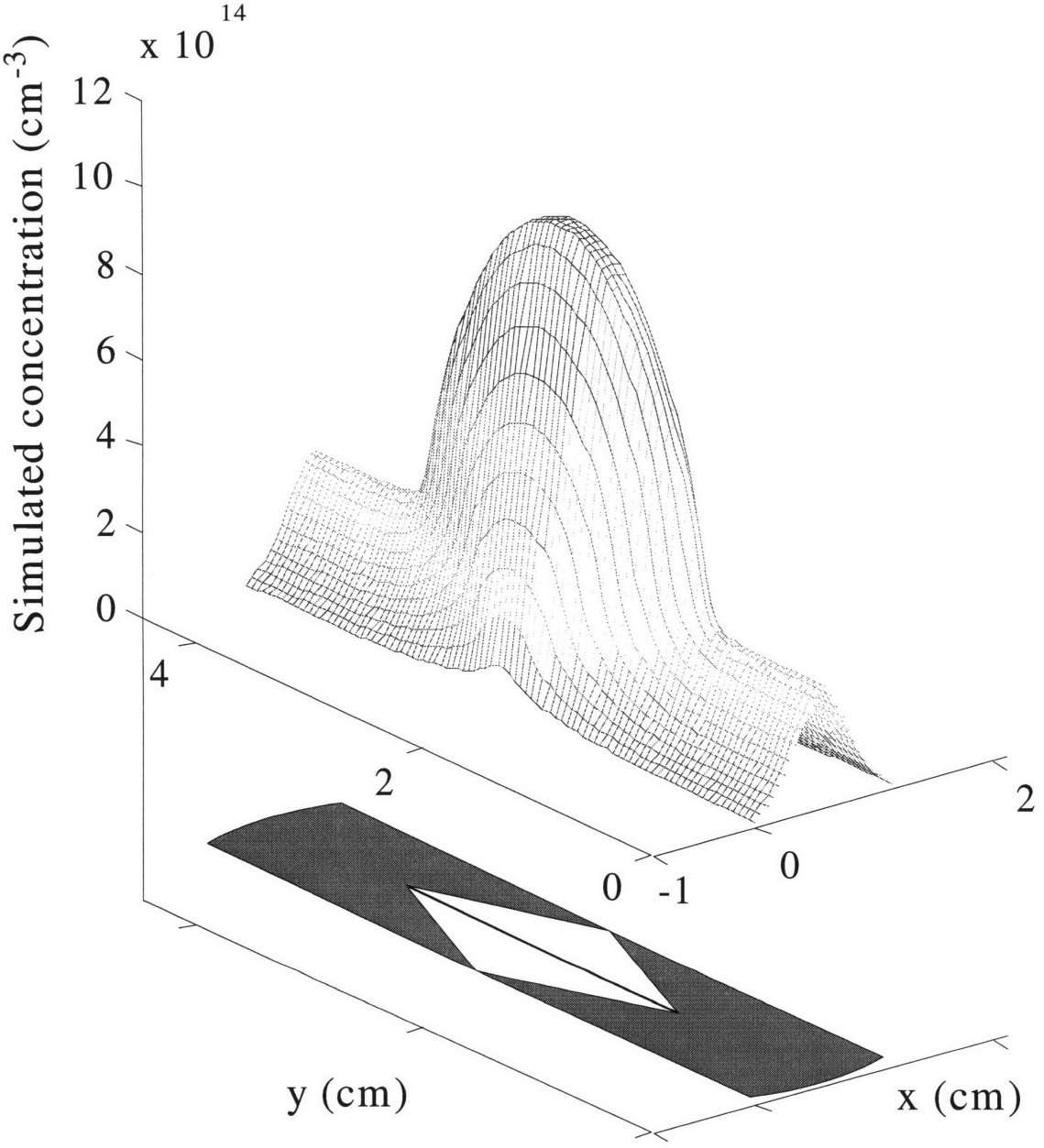

Figure 5-10: An example of the simulated gas-phase concentration just above the substrate surface.

(Model parameters: P=20 torr, C_f=3x10^{15} cm^{-3}, k_m=10 cm^{-1}.)

5-11 of the simulated C_s directly beneath the filament is also proportional to the predicted growth rate along that line.

The normalized concentrations directly beneath the filament for k_m = 0.5, 1, 4, and 8 cm^{-1} are presented in Figure 5-12. The factor of 2, with a standard deviation of 0.3, difference in experimental end-to-center linear growth rates is most similar to the concentration difference predicted for $k_m = 4 \pm 1$ cm^{-1}.

When we increase the extent of the simulation in the positive y-direction by 6 mm as shown in Figure 5-13 while keeping the grid spacing and boundary conditions the same, the resulting simulated C_s for k_m = 100 cm^{-1} differs from the base case result by at most 30%. Most of this difference, however, occurs at the +y-direction boundary. Beneath the filament, the simulated concentration changes by less than 2% when compared with the original result. For k_m = 10 cm^{-1} this changes to a maximum of 7% while for k_m = 1 cm^{-1}, the difference in the predicted near-surface concentrations below the filament between the original simulation volume and the extended volume increases to 24%. The change in the extent of the boundary condition for the case of k_m = 10 cm^{-1} also changes the end-to-center concentration ratio by 7%.

Since our estimated value for k_m from the growth rate variation data is between 1 and 10 cm^{-1}, we can reasonably estimate that our choice of boundary condition will introduce a roughly 15% error in our estimate of k_m. This result implies that the experimentally observed drop off in growth rate as we move away from the filament in a perpendicular direction can be primarily explained by gas diffusion and loss to surface reaction. The other likely cause of the observed lack of deposition is a decrease in the substrate temperature. Wolden has modeled the temperature gradient across a 4" Si wafer

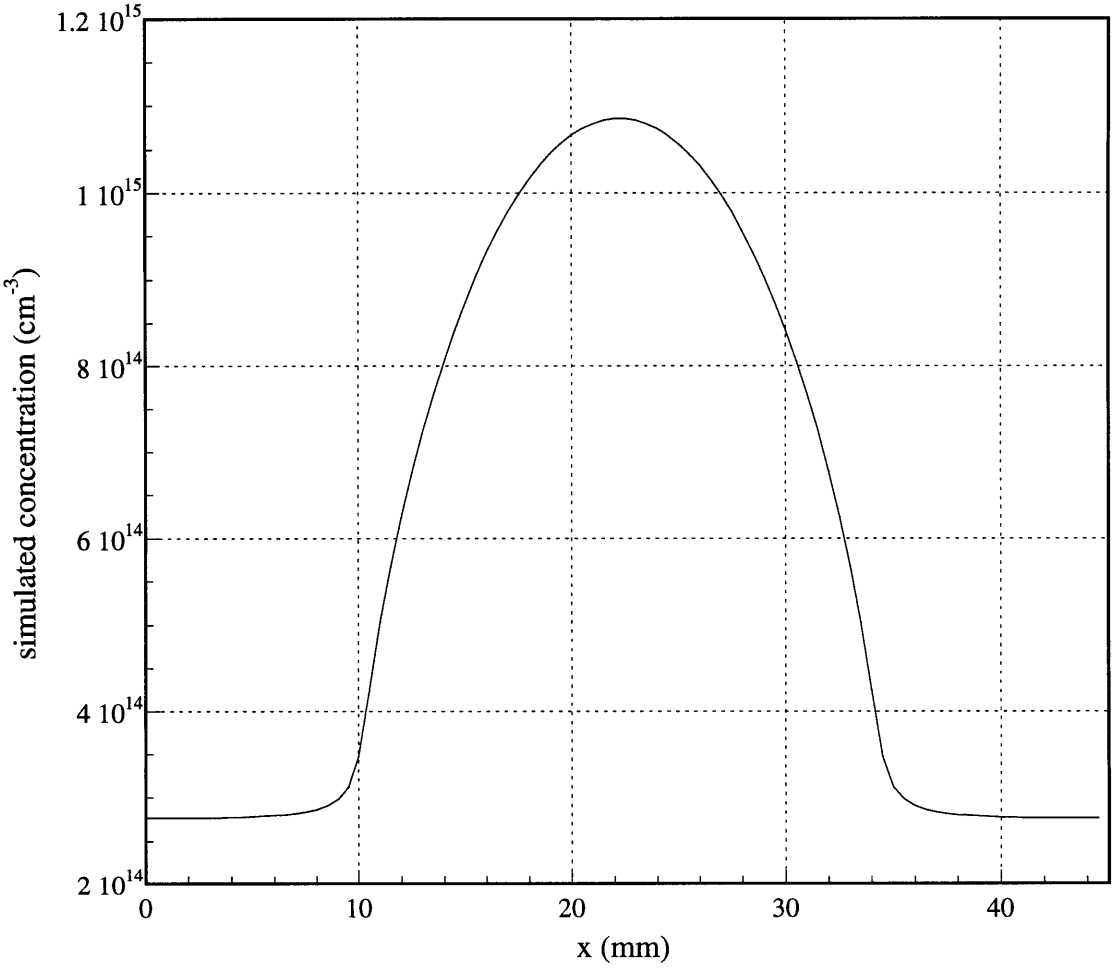

Figure 5-11: Modeled C_s beneath the filament from the simulation result shown in Fig. 5-10.

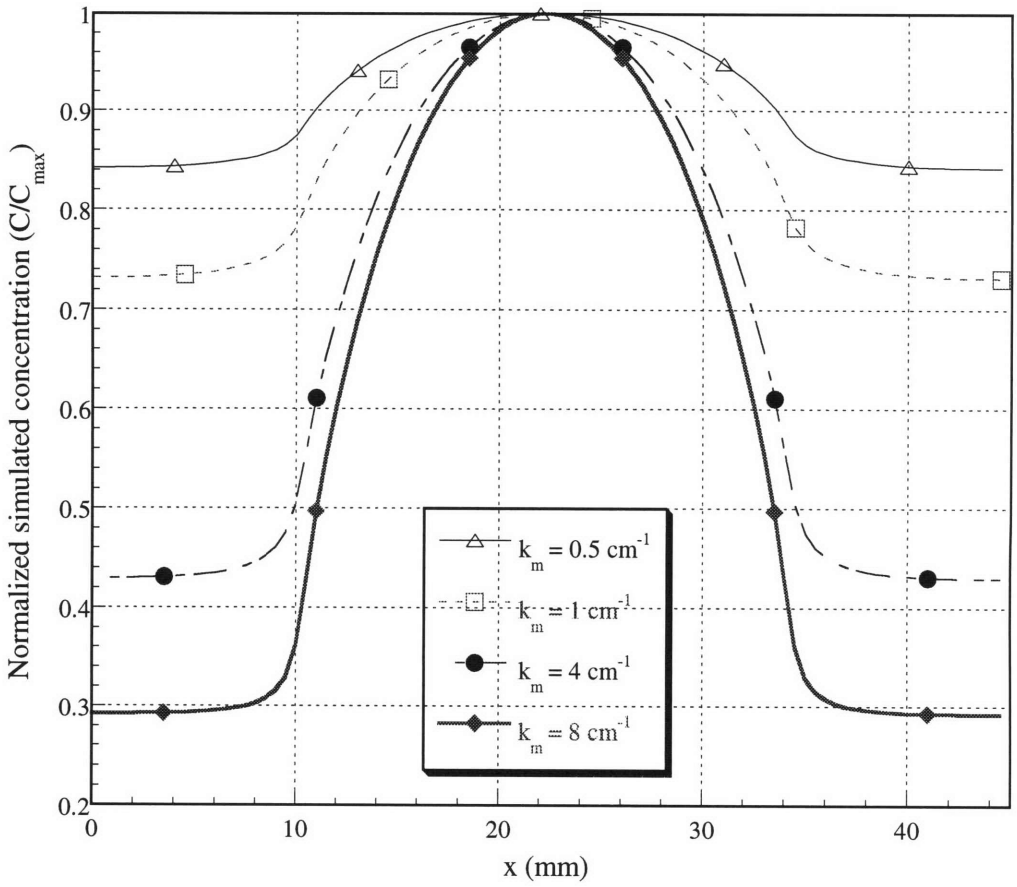

Figure 5-12: Normalized, simulated concentrations along the central, selectively deposited line beneath the filament for k_m=0.5, 1, 4, 8 cm^{-1}

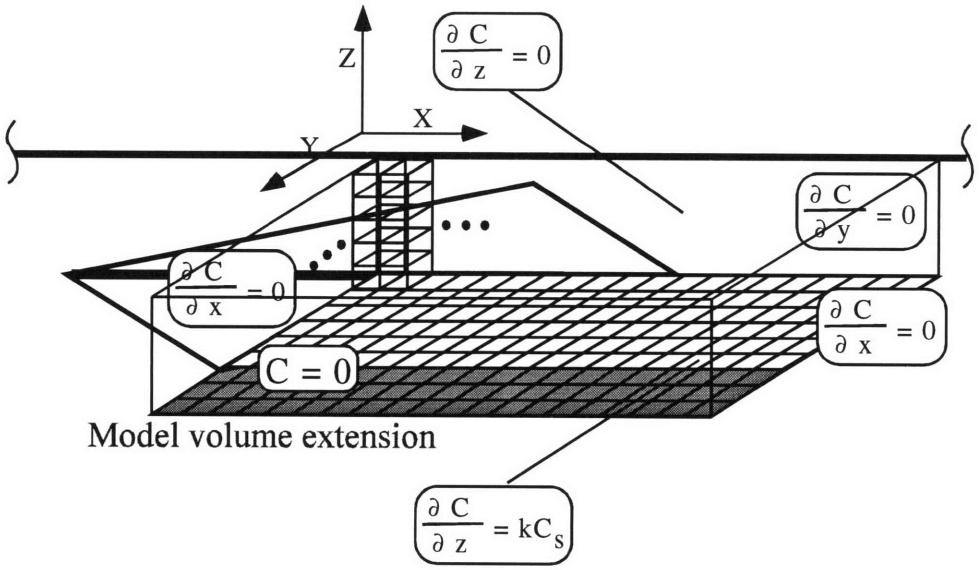

Figure 5-13: Schematic of the discretization of the simulation volume with the +y-direction boundary condition extended by 3 mm

in a hot-filament diamond deposition system with a single filament due to radiative heating and loss.[13] A temperature difference of 150 K was estimated between the center of the wafer and a point 2 cm away in a direction perpendicular to the filament axis. Parallel to the filament axis, the substrate temperature drops less than 25 K within 2 cm. Because our system has the added complication of heat loss by conduction and a filament which extends past the edge of the wafer, the gradients parallel to the filament axis in the radiation-only model provide only an upper bound since the temperature uniformity of a cooled substrate will be improved over an uncooled substrate. The statistically insignificant variations in diamond density directly below the filament as measured in the control sample (Tab. 5-1) demonstrates that the temperature related effects in our region of interest are indeed small.

5.4 Discussion

By supposing that surface H-atom abstraction by gas phase H-atoms is the rate limiting step responsible for the observed growth rate variations, the first order rate coefficient can be calculated. The gas diffusion coefficient for H in a bath gas of H_2 can be estimated by[15]

$$D_{ab} = 0.0018583 \frac{\sqrt{T^3 \left[\frac{1}{M_a} + \frac{1}{M_b}\right]}}{p\, \sigma_{ab}^2\, \Omega_{ab}} \qquad (5\text{-}22)$$

where T is the temperature [=] K
M_a and M_b are the molecular weights of species *a* and *b* [=] $\frac{gm}{mol}$
p is the pressure [=] atm
σ is the Lennard-Jones collisional parameter
Ω_{ab} is a dimensionless function of T and of the intermolecular potential field for a molecule of *a* and a molecule of *b*
{The values of σ and Ω_{ab} are from Dandy *et al.*.[12]}

The temperature profile in a hot-filament reactor have been measured.[9] For T_f = 2820 K and P = 20 torr, the gas temperature varied in a roughly linear fashion over 7 mm, dropping from 2650 K at 0.25 mm away from the filament to 1650 K above the substrate which was at 1120 K. Using an average gas phase temperature of 2000 K for our system which was operated at cooler temperatures, the diffusion coefficient calculated by Eqn. 5-22 is 2000 $\frac{cm^2}{s}$. From the definition of k_m and our estimated value of 4 ± 1 cm^{-1}, k_s is estimated to be from 4800 - 12000 $\frac{cm}{s}$, based on a 20% error in the calculation of D. From the definition of k_s in Eqn 5-7 and assuming that k_2, the rate coefficient for H-atom addition to an open site, is much greater than k_1, the rate coeffient for H-atom abstraction, $k_1 \approx \frac{k_s}{2\Gamma}$. Using a total site density of $\Gamma = 1.8 \times 10^{15}$ cm^{-2} on the diamond (111) surface, k_1 is from 1.3×10^{-12} - 3.3×10^{-12} $\frac{cm^3}{s}$.

Krasnoperov *et al.* measured the H-atom surface loss coefficient, γ, which is defined as the ratio of H-atoms lost to surface reactions to the flux of H-atoms to the surface.[7] Based on a value of $\gamma = 10^{-3.4\pm0.3} + 10^{0.29\pm0.15} \exp\left(\frac{-6020 \pm 470 \text{ cal}}{RT}\right)$, they calculated a rate constant for H-atom abstraction. At a surface temperature of 1000 K, the rate constant is in the range from 1.7×10^{-12} - 5.4×10^{-12} $\frac{cm^3}{s}$. Koleske *et al.* measured the kinetics of hydrogen abstraction by atomic deuterium more directly. Using their estimate of 1% deuterium dissociation, k_s at a surface temperature of 1000 K is calculated to be 2.8×10^{-12} - 4.6×10^{-12} $\frac{cm^3}{s}$.[6] Furthermore, recent work to directly measure the atomic hydrogen concentration in a hot filament deposition system during growth has shown γ to be from

0.013 to 0.05.[8] A rate constant can be calculated from γ by assuming a first order reaction and using the definition of γ,

$$\gamma = \frac{k_1 \Gamma C_s}{\text{(flux from kinetic gas theory)}} = k_1 \Gamma \sqrt{\frac{2 \pi M_H}{R T}} \qquad (5\text{-}23)$$

Rearranging, we find that k_1 at 1000 K is 0.8×10^{-12} - $3.2 \times 10^{-12} \frac{cm^3}{s}$.

If, on the other hand, we assume that, instead of hydrogen abstraction by a H-atom, a surface reaction involving methyl radicals is the growth limiting step, then k'_s from our value for k_m would be 1610 - 4020 $\frac{cm}{s}$ based on a diffusion coefficient of 670 $\frac{cm^2}{s}$ for CH_3 from Eqn. 5-22. If we add the methyl radical addition to an active surface site; i.e.,

$$CH_3 + C^*_{surf} \xrightarrow{k_3} H_3C\text{-}C_{surf} \qquad (5\text{-}24)$$

to our pair of surface reactions {Eqn (5-2) & (5-3)}, we can write down a mass balance for methyl:

$$-D \frac{d[CH_3]}{dz} = -k_3 [CH_3][C^*_{surf}] \qquad (5\text{-}25)$$

The steady state expression for $[C^*_{surf}]$ then becomes

$$k_1 [CH_{surf}][H] = [C^*_{surf}] (k_2 [H] + k_3 [CH_3]) \qquad (5\text{-}26)$$

Harris has estimated that k_2 is an order of magnitude larger than k_3 [3] which when coupled with the fact that [H] is about two orders of magnitude greater than $[CH_3]$ implies that the the surface site equilibrium is not perturbed by the methyl addition reaction. Substituting the steady state expression from Eqn (5-5) plus the definition of Γ from Eqn (5-6) gives us

$$-D \frac{d[CH_3]}{dz} = -\frac{k_1 k_3}{k_1 + k_2} \Gamma [CH_3] = -k'_s [CH_3] \qquad (5\text{-}7)$$

Using estimates of $1x10^{-12}$ cm^3/s and $1x10^{-10}$ cm^3/s for k_1 and k_2, respectively,[3] we can calculate a value of $1x10^{-10}$ cm^3/s for k_3 which is an order of magnitude larger than the value proposed by Harris of $1x10^{-11}$ cm^3/s.[3]

Finally, in addition to measuring the rate constant for H-abstraction from a diamond surface by an H-atom, Krasnoperov *et al.* also estimated the rate constant for H-abstraction from a diamond surface by a methyl radical as being $0.02x10^{-12}$ - $1.3x10^{-12}$ $\frac{cm}{s}$.

These results are summarized in Table 5-2.

Table 5-2: Comparison of various rate constants for H-atom abstraction

Method	Rate constant ($x10^{12}$)
for $H\bullet_{gas} + H\text{-}C_{surface} \rightarrow H_2 + \bullet C_{surface}$	
this work	2.3 ± 1.0 cm^3/s
TOF-SARS[6]	3.7 ± 0.9 cm^3/s
photoionization mass spectrometry[7]	3.5 ± 1.9 cm^3/s
fit to $[H]_{gas}$ measurement using THG[8]	2.0 ± 1.2 cm^3/s
for $CH_3\bullet_{gas} + H\text{-}C_{surface} \rightarrow CH_4 + \bullet C_{surface}$	
photoionization mass spectrometry[7]	0.02 -1.3 cm^3/s
$CH_3\bullet + \bullet C_{surf} \rightarrow H_3C\text{-}C_{surf}$	
this work	100 cm^3/s
estimated from hydrocarbon analogy[3]	10 cm^3/s

5.5 Conclusions

Diamond growth rate variations were observed on a selectively patterned, pre-nucleated substrate. By modeling the gas phase diffusion in the volume between the hot filament and the substrate with a three dimensional finite difference model, similar

differences in the gas phase concentration above the substrate surface were predicted for a Damköhler number of 2.4.

By assuming that hydrogen atoms are the primary growth limiting species, a first order surface reaction coefficient was calculated from estimates of the H-atom gas phase diffusion coefficient. Using an average gas temperature, k_1, the rate coefficient for hydrogen abstraction from a hydrogen terminated diamond surface by an H-atom, was calculated to be $(2.3\pm1.0)\text{x}10^{-12}\ \frac{cm^3}{s}$ which is slightly lower than the values of $(3.5\pm1.9)\text{x}10^{-12}\ \frac{cm^3}{s}$ as determined from photoionization mass spectrometry measurements for the kinetics of H-atom abstracting an H-atom from diamond and $(3.7\pm0.9)\text{x}10^{-12}\ \frac{cm^3}{s}$ from time-of-flight ion scattering and recoil spectroscopy, but close to $(2.0\pm1.2)\text{x}10^{-12}\ \frac{cm^3}{s}$ as determined by a fit to the gas phase H-atom concentration measured by an optical THG method. Considering the assumptions of the model, however, it is fair to say that this result is reasonably close to all three literature values.

If we had instead supposed that methyl radical addition to an open surface site is the growth limiting reaction, the first order reaction coefficient from our observed growth variation would be $1\text{x}10^{-10}\ \frac{cm^3}{s}$. This is an order of magnitude larger than the estimated rate constant of $1\text{x}10^{-11}\ \frac{cm^3}{s}$ which is based on an analogy with similar hydrocarbon reactions.

The correspondence between the calculated rate constant from assuming that H-abstraction by a gas-phase hydrogen atom is the growth limiting reaction and the published values lends support to the theory that H-atom's are the main growth limiting

species in CVD diamond growth. A similar analysis assuming methyl radicals as the growth limiting species shows no such correspondence.

References:

1. M. Frenklach, and H. Wang, *Phys. Rev. B*, **43** (2), 1520-1545 (1991).
2. J. E. Butler, and R. L. Woodin, *Phil. Trans. R. Soc. Lond. A*, **342**, 209-224 (1993).
3. S. J. Harris, *J. Appl. Phys.*, **56**, 2298 (1990).
4. M. Frenklach, and K. E. Spear, *J. Mater. Res.*, **3** (1), 133-140 (1988).
5. D. G. Goodwin, and G. G. Gavillet, *J. Appl. Phys.*, **68** (12), 6393-6400 (1990).
6. D. D. Koleske, S. M. Gates, B. D. Thoms, J. N. Russell, Jr., and J. E. Butler, *J. Chem. Phys.*, **102** (2), 992-1002 (1995).
7. L. N. Krasnoperov, I. J. Kalinovski, H.-N. Chu, and D. Gutman, *J. Phys. Chem.*, **97**, 11787-11796 (1993).
8. L. L. Connell, J. W. Fleming, H.-N. Chu, D. J. Vestyck Jr., E. Jensen, and J. E. Butler, *J. Appl. Phys.*, **78** (6), 3622-3634 (1995).
9. K.-H. Chen, M.-C. Chuang, C. M. Penney, and W. F. Banholzer, *J. Appl. Phys.*, **71** (3), 1485-1493 (1992).
10. U. Meier, K. Kohse-Höinghaus, L. Schäfer, and C.-P. Klages, *Appl. Opt.*, **29** (33), 4993-4999 (1990).
11. L. Schäfer, C.-P. Klages, U. Meier, and K. Kohse-Höinghaus, *Appl. Phys. Lett.*, **58** (6), 571-573 (1991).
12. D. S. Dandy, and M. E. Coltrin, *J. Mater. Res.*, **10** (8), 1993-2010 (1995).
13. C. A. Wolden, Ph. D. Thesis, Massachusetts Institute of Technology, 1995.
14. E. Colas, C. Caneau, M. Frei, E. M. Clausen Jr., W. E. Quinn, and M. S. Kim, *Appl. Phys. Lett.*, **59** (16), 2019-2021 (1991).
15. R. B. Bird, W. E. Stewart, and E. N. Lightfoot, *Transport Phenomena*. John Wiley & Sons: New York. 1960.

6. SILICONE DEPOSITION

Silicone is a generic name for the class of polymers which consist of a repeating Si-O backbone with organic functional groups attached to the Si via Si-C bonds. The most common of these functional groups is methyl, resulting in the silicone, poly(dimethylsiloxane) or PDMS. Because of its excellent combination of properties, conventional crosslinked PDMS is used in a wide range of applications from the potting and encapsulation of electronics and electrical connections to medical implants such as heart valve poppets and intraocular lenses.[1] There has been considerable interest in extending these applications through the chemical vapor deposition of silicone thin films. Potential applications include biocompatible coatings for medical implants,[2] permselective membranes,[3] integrated optical devices,[4] dielectric films,[5] and abrasion and corrosion resistant coatings.[6] To date, all such efforts have focused on plasma polymerized (PP) films from a large variety of monomers such as hexamethyldisiloxane, tetramethylsilane, and octamethylcyclotetrasiloxane; these have all been extensively reviewed by Wróbel and Wertheimer.[7] A potential problem in the application of these films as dielectric layers, however, arises due to the high dielectric loss when compared to the conventional polymer as well as an aging effect upon exposure to the atmosphere. Both of these effects can be related to the high density of trapped radicals that originate from the plasma induced ion bombardment of the surface.[8] A pyrolytic process, on the other hand, in which the growth precursor are thermally produced does not suffer from ion bombardment and has been shown in the case of fluorocarbon polymer CVD to result in a lower density of dangling bonds.[9]

We have developed a pyrolytic process for the deposition of silicone thin films from the low-pressure pyrolysis of octamethylcyclotetrasiloxane (D_4); see Figure 6-1 for the structure. D_4 is a monomer which is commonly used in the base catalyzed, liquid phase ring-opening polymerization to PDMS, making it a candidate for a similar thermally mediated, ring-opening gas-phase reaction. Such a hypothetical reaction would lead to polymer film growth from the resulting straight chain diradical. D_4 was also chosen as a feed gas for this process because it melts at 17 °C and hence is a liquid at standard conditions with a reasonable vapor pressure.

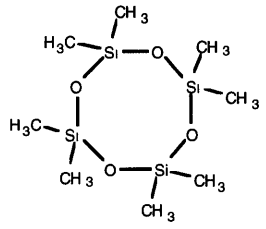

Figure 6-1: Structure of octamethylcyclotetrasiloxane

6.1 Experimental setup

The deposition system is essentially the same as the acetone based HFCVD diamond system. Approximately 2 sccm of D_4 was vaporized through the reactor chamber by mildly heating a Pyrex test tube attached to a large diameter throttle valve on the chamber. The flow of feed was not precisely controlled with a mass flow controller because the narrow orifice in an MFC would have further reduced the already low flow of a low vapor pressure material. Furthermore, it was believed that the flow measurement

method of a standard thermal MFC would lead to clogging problems similar to that of a previous experiment with another thermally sensitive monomer. Heating was accomplished by wrapping heating tape around the test tube and feed tubing up to the point that it entered into the reactor and controlling the AC power with a variable transformer. While no exact measurements of the feedline temperature were taken, it is estimated to not have gone above 40 °C. Pressure in the reactor was maintained at 0.6 Torr by adjusting a butterfly throttle valve on the reactor outlet.

About 6" of a 1 mm diameter tantalum wire (Alfa Aesar 99.95%) was shaped into a serpentine configuration; it is schematically shown in Figure 6-2. This serpentine geometry has the advantage of a relatively large area of uniform deposition plus good structural stability after repeated thermal cycling. The filament was resistively heated to a filament temperature, T_f, between 260 and 530 °C for these experiments. T_f was measured by extending a K-type thermocouple, that usually measures the substrate backside temperature, until it contacted the filament. A small, thin (~10 cm^2, 0.02 cm thick) ceramic sheet was placed between the filament and the thermocouple for insulation. A plot of the filament temperature versus the DC input power is shown in Figure 6-3.

Typically, the substrate was a 2" Si wafer sitting on a water cooled stage located approximately 11 mm away from the filament; the temperature as measured by a thermocouple on the backside of the wafer was 20 ± 3 °C. The film thickness in the center of the substrate was measured by a combination of ellipsometry and profilometry. Films thicker than approximately 1 μm were measured by scratching the film with a razor blade and taking multiple measurements with a Sloan Dektak 3 profilometer. For thinner films, a

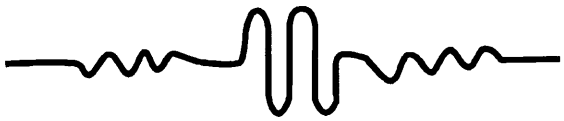

Figure 6-2: Full scale representation of the serpentine filament geometry

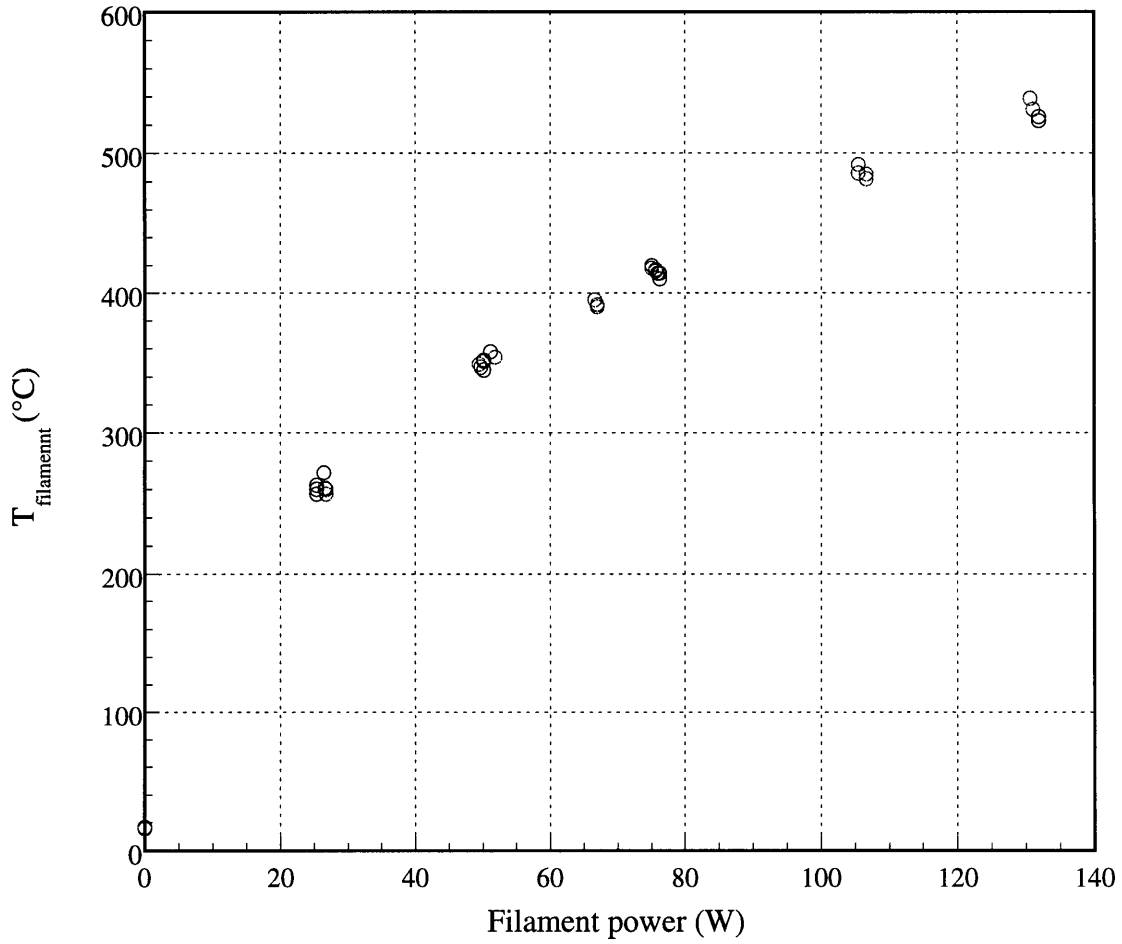

Figure 6-3: Filament power/temperature correlation for PDMS HFCVD (serpentine filament configuration)

nulling type ellipsometer (Rudolph Research AutoEl II) was used, with the profilometer providing an approximate measurement from which to gauge which thickness cycle to use.

A total of nine films were deposited at a pressure of 0.6 Torr and a variety of filament temperatures. The deposition rates are listed in Table 6-1 and shown graphically in Figure 6-4. The first set of films were deposited consecutively at a filament to substrate distance of 10.5 mm. The second set were also deposited as a set but at a later time at a filament to substrate distance of 11 mm. The growth rates varied from $2.7x10^4$ to 5 Å/min depending on the filament temperature. By comparison, the maximum deposition rates reported for the plasma polymerization of hexamethyldisiloxane varied from 0.5 $\mu g\, cm^{-2}\, s^{-1}$ for capacitively coupled discharges[10] to 2.6 $\mu g\, cm^{-2}\, s^{-1}$ for microwave discharges,[11] which translate to linear growth rates of about $3x10^3$ and $1.6x10^4$ Å/min, respectively.

Table 6-1: Deposition rates for HFCVD PDMS films at various filament temperatures

Film	Filament power	T_f	Film thickness	Dep. time	Deposition rate
A	26 W	270 °C	0.015 μm	30 min	5.0 Å/min
B	50 W	350 °C	0.51 μm	20 min	260 Å/min
C	75 W	410 °C	6.9 μm	15 min	$4.6x10^3$ Å/min
D	130 W	520 °C	40 μm	15 min	$2.7x10^4$ Å/min
1	50 W	350 °C	0.070 μm	30 min	23 Å/min
2	65 W	390 °C	0.705 μm	30 min	235 Å/min
3	75 W	430 °C	0.853 μm	15 min	570 Å/min
4	105 W	490 °C	6.4 μm	10 min	$6.4x10^3$ Å/min
5	130 W	530 °C	18.7 μm	10 min	$1.9x10^4$ Å/min

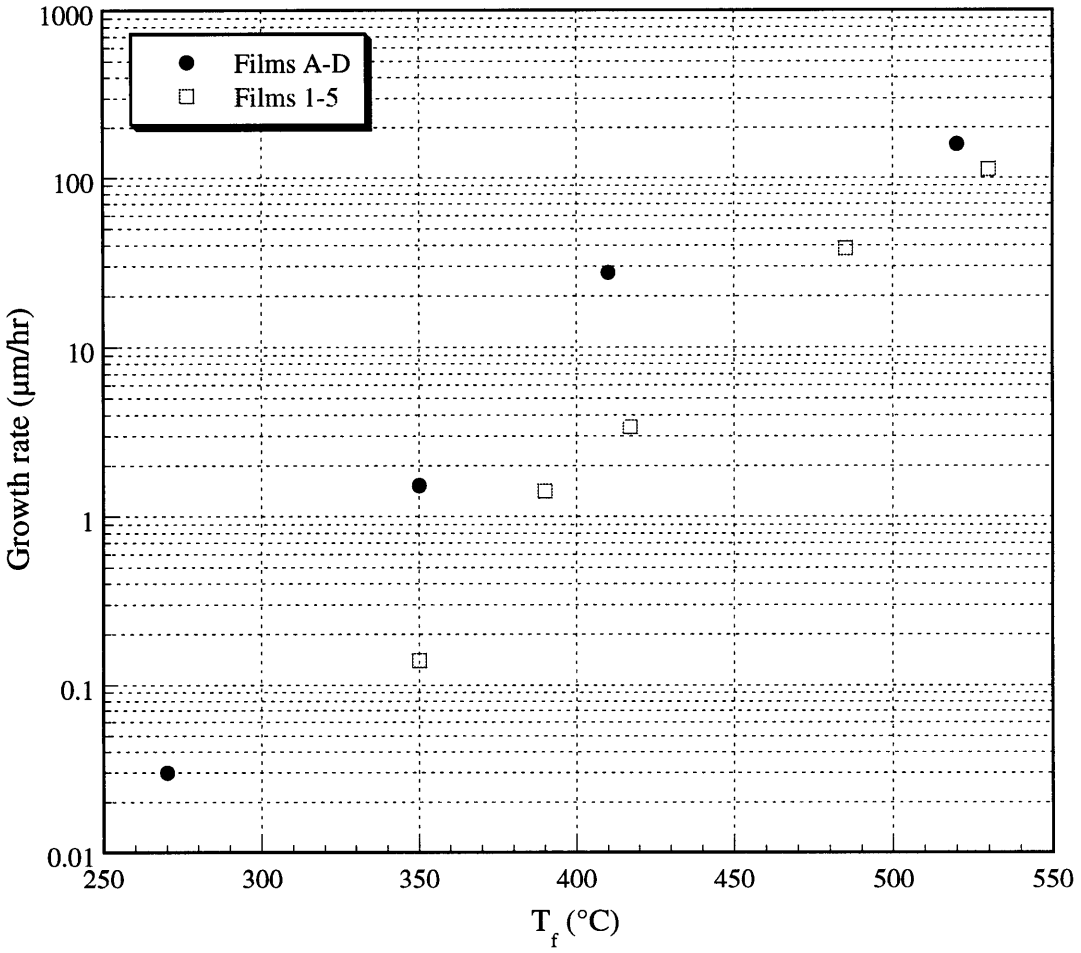

Figure 6-4: PDMS deposition rate as a function of filament temperature (Center of wafer, serpentine filament configuration)

6.2 Characterization

6.2.1 Fourier transform infrared spectroscopy (FTIR)

The first set of CVD thin films from Tab. 6-1 were analyzed by a Fourier transform infrared spectrometer (Nicolet Magna-IR 860) operating in transmission mode. The coated wafers were mounted in a holding bracket and the spectra taken by analyzing the radiation transmitted through the center of the wafer.

A comparison of the FTIR spectra of films B and C from Tab. 6-1 versus that for a viscous liquid PDMS standard (Aldrich Chemical, secondary standard) is shown in Figure 6-5. Films A and D were too thin and too thick, respectively, to generate meaningful results; film A showed less than 2% absorbance while film D went off scale. A qualitative analysis of the spectra indicates that the samples and the standard have

Table 6-2: FTIR peak assignments for PDMS

Wavenumber	Functional group	Reference
2960 cm^{-1}	asym. C-H stretch in sp^3-CH_3	McNamara, et al.[12]
2920 cm^{-1}	asym. C-H stretch in sp^3-CH_2	McNamara, et al.[12]
2880 cm^{-1}	sym. C-H stretch in sp^3-CH_3	McNamara, et al.[12]
2850 cm^{-1}	sym C-H stretch in sp^3-CH_2	McNamara, et al.[12]
2200 cm^{-1}	Si-H stretch	Tajima and Yamamoto[13]
1410 cm^{-1}	C-H bending in SiC-H_3	Wright and Hunter[14]
1258 cm^{-1}	methyl rocking about Si-CH_3	Wright and Hunter[14]
~1049 cm^{-1}	asym. Si-O-Si stretch	Tajima and Yamamoto[13]
842 cm^{-1}	Si-C stretch in -OSi-$(CH_3)_3$	Wright and Hunter[14]
800 cm^{-1}	Si-C stretch in -OSi-$(CH_3)_2$-	Wright and Hunter[14]
702 cm^{-1}	Si-C stretch	Ebsworth, et al.[15]

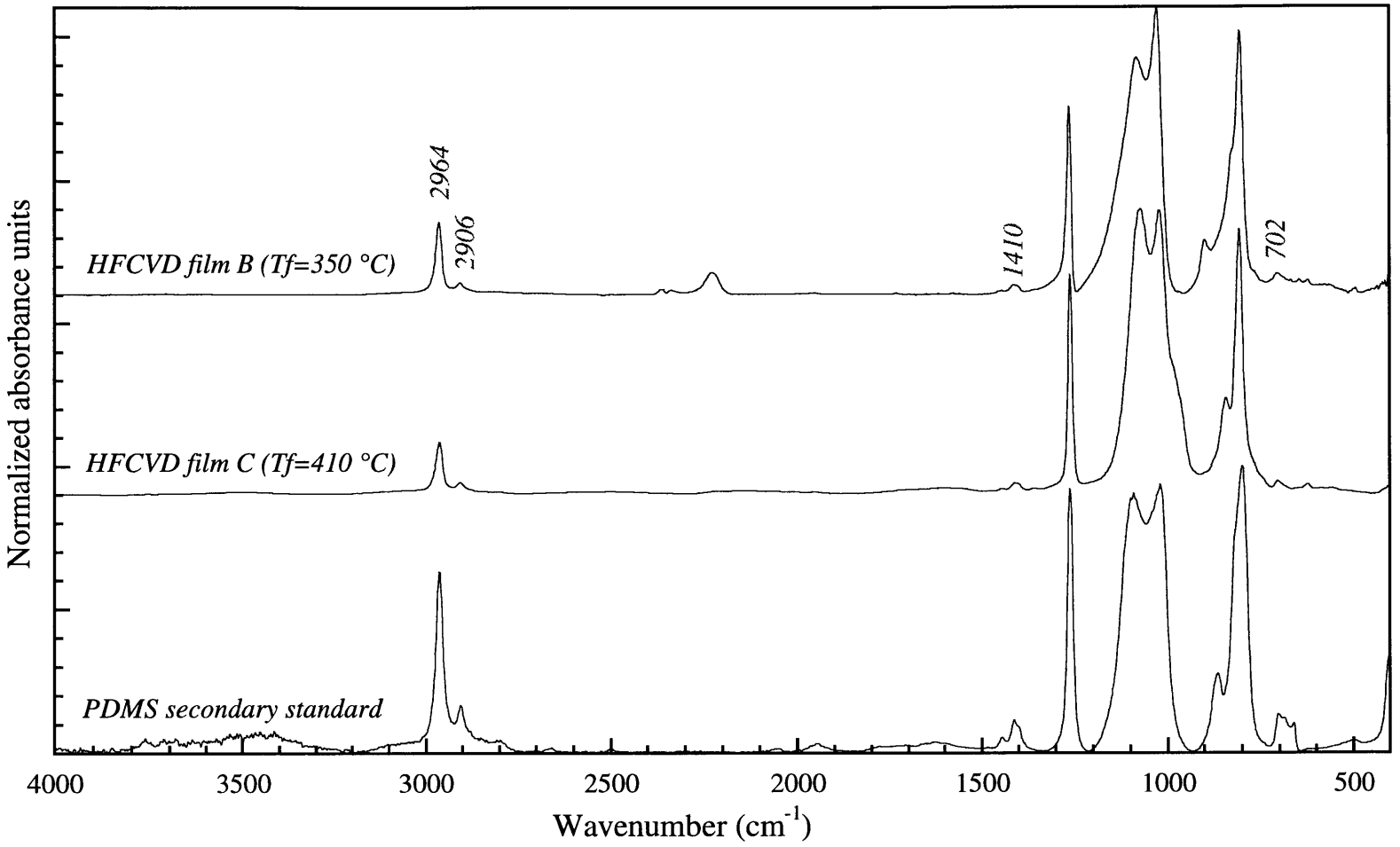

Figure 6-5: Comparison of normalized FTIR absorbance spectra for PDMS HFCVD thin films B & C (see Tab. 6-1) and the PDMS secondary standard

absorbance peaks at identical wavelengths and hence identical IR active functional groups; Table 6-2 is a listing of all the peak assignments.

In order to permit semi-quantitative analysis, the spectra are shown in normalized absorbance units. The first feature to note is the marked difference in relative intensity between the CVD film and the standard at 2964 cm^{-1}, 2906 cm^{-1}, 1410 cm^{-1}, and 702 cm^{-1}. The peaks at 2964 cm^{-1} and 2906 cm^{-1} are due to the asymmetric and symmetric C-H methyl stretches, respectively, while the peak at 1410 cm^{-1} is the result of the C-H methyl bending modes.[14] This suggests that the CVD film is deficient in methyl substituents as compared to the PDMS standard. However, variations in oscillator strengths in the different materials could also give rise to the observed differences in relative intensity. We can also rule out the loss of sp^3-CH_3 absorption intensity due to any C-C crosslinking since such a rearrangement would result in the appearance of new peaks in the C-H stretch region at a lower wavenumber corresponding to sp^3-CH_2.

The other important feature to note is the broad split doublet between 1000 cm^{-1} and 1100 cm^{-1} that is present in all the spectra. It has been noted that this broad doublet indicates the presence of long siloxane chains or large cyclic compounds with greater than approximately 10 siloxane units.[16] The IR spectrum for D_4, our cyclic tetramer feed gas, is shown in Figure 6-6 as an example of a short chain compound which lacks this signature. Rau and Kulisch have analyzed plasma polymerized films of D_4 and used the relative intensities of the two peaks in this characteristic band to argue that increased r.f. power leads to longer chains and/or larger rings; see Figure 6-7.[17]

Since they presented their data in absorption units, we can semi-quantitatively compare the siloxane chain length in the pyrolytic CVD films versus the PP films by

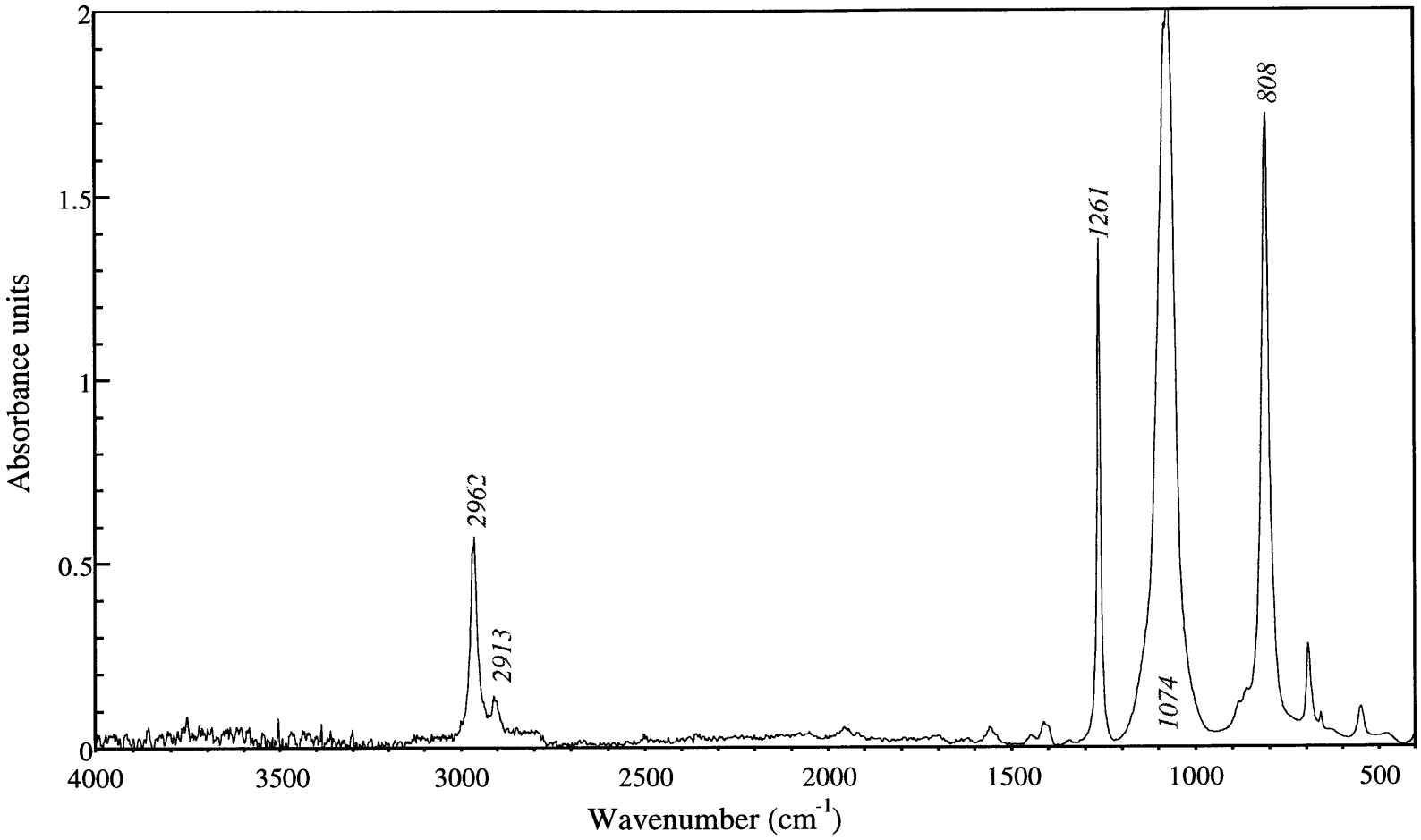

Figure 6-6: FTIR absorbance spectra for octamethylcyclotetrasiloxane (D_4)

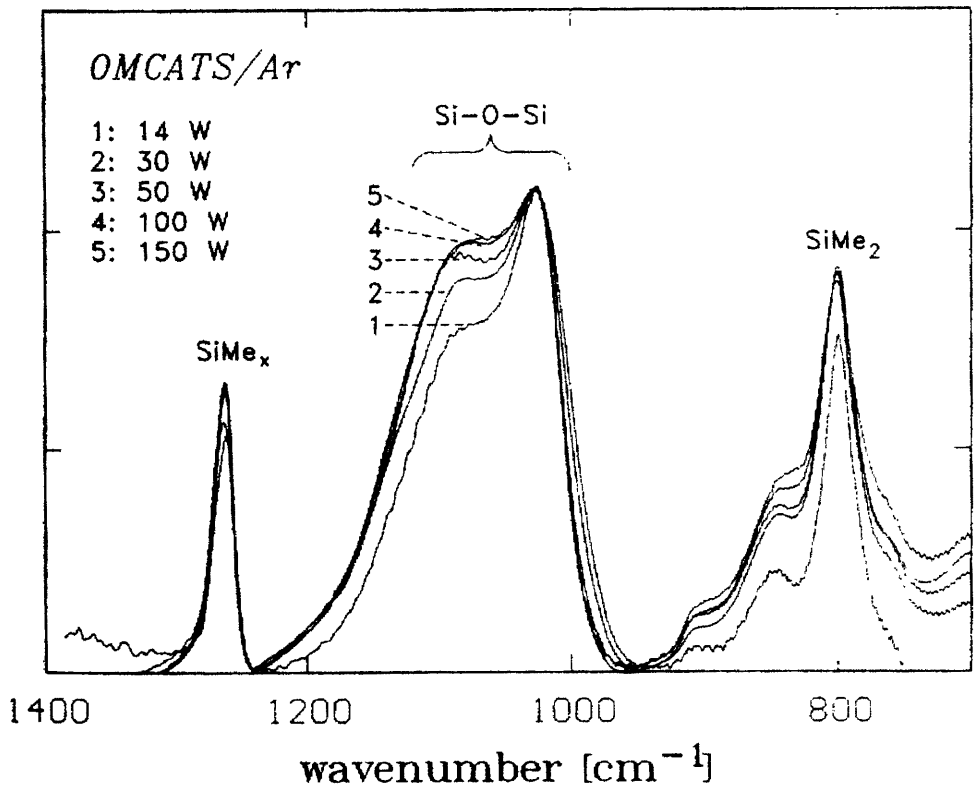

Figure 6-7: FTIR absorbance spectra for plasma polymerized D_4 film at various r.f. power levels

From C. Rau, and W. Kulisch, *Thin Solid Films*, **249**, 28-37 (1994).

looking at the "extent of splitting" of the asymmetric stretch peak. Looking at Fig. 6-5 and 6-7, the pyrolytic film clearly resembles the PDMS standard more than the PP film does in this respect. A comparison of the spectra in other regions shows the same general trend; i.e., a loss of intensity in the peaks associated with hydrocarbon groups. There is also evidence of a Si-H peak in the PP film spectra at 2140 cm^{-1} similar to the one at 2220 cm^{-1} in the spectrum for film B (Fig. 6-5). Since the Si-H stretching vibration typically has a high oscillator strength[16] but only occurs as a small peak in some of the pyrolytic films, it was concluded to be only present in small amounts.

6.2.2 X-ray photoelectron spectroscopy (XPS)

X-ray photoelectron spectroscopy was used to determine the relative elemental composition of the CVD films, keeping in mind that hydrogen can not be detected via XPS. Survey scans were conducted on CVD films B, C, D, and 4 from Tab. 6-1 as well as the PDMS secondary standard and a 100,000 centiStoke PDMS fluid (Aldrich Chemical). An example of such a spectra, taken for sample B, is shown in Figure 6-8. By assuming that the PDMS standard has the ideal elemental composition of C_2SiO and adjusting the instrument sensitivity factors for the O 1s (SF=2.48), C 1s (SF=1), and Si 2p (SF=0.91) peaks to reflect this, the composition of the various samples were determined. These results are given in Table 6-3 and provide additional evidence of the loss of methyl substituents suggested by FTIR spectroscopy. Also listed in Tab. 6-3 are the ideal C:Si ratios for the loss of **n** methyl groups from a long PDMS chain for comparison. This result further shows that the Si-O backbone is left intact by the deposition process because all of the films have a O/Si ratio of 1.05 ± 0.05.

Table 6-3: XPS elemental analysis and comparison to ideal values (Ref. to a PDMS secondary standard; sensitivity factors: SF(O 1s)=2.48, SF(C 1s)=1, SF(Si 2p)=0.91)

Film	O 1s	C 1s	Si 2p
PDMS secondary stnd	1	2	1
PDMS 100kcSt fluid	0.89	1.86	1
B (350 °C)	1.03	1.42	1
C (410 °C)	1.00	1.53	1
4 (490 °C)	1.03	1.6	1
D (520 °C)	1.04	1.59	1
loss of 1 CH_3/D_4	1	1.75	1
loss of 2 CH_3/D_4	1	1.5	1
loss of 4 CH_3/D_4	1	1	1

Figure 6-9 illustrates a high resolution scan of sample B about the Si 2p transition. While it has been reported that it is possible to resolve the Si 2p peak into multiple peaks which correspond to the various Si oxidation states,[3] our spectra can not be quantitatively resolved due to the width of the peaks. For example, the peak in Fig. 6-9 can possibly be argued to have a shoulder on its left side and hence fitted with a large peak at 102.2 eV due to Si^{2+} and a smaller one at 103.1 eV due to Si^{3+}, a 0.9 eV shift. This fact would be consistent with the observation that Si^{4+} has a chemical shift of ~4 eV relative to the zero-valent state at 99.4 eV.[18] However, such a fit would be suspect because of the large amount of overlap between the two peaks. An attempted fit gave constituent peaks with a full width at half maximum of 1.4 eV, half an eV larger than the separation of the peaks. Therefore, the only conclusion which can be drawn from the Si 2p spectrum is the lack of a significant concentration of silicon oxidation states other than Si^{2+}.

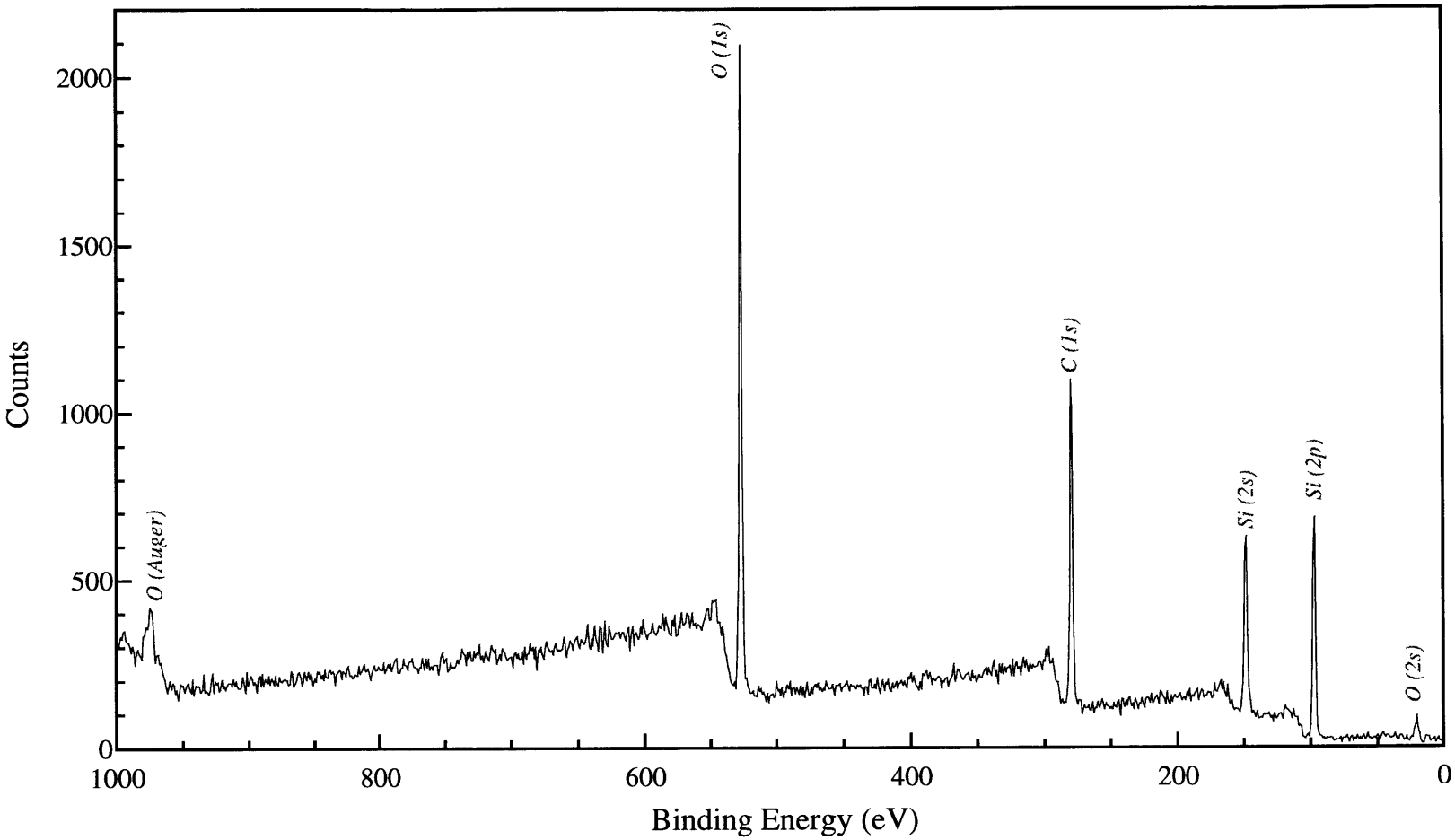

Figure 6-8: XPS survey scan of PDMS sample B (see Tab. 6-1)

(Spectrum has been charged corrected by +5.7 eV with reference to the C 1s peak at 285.6 eV)

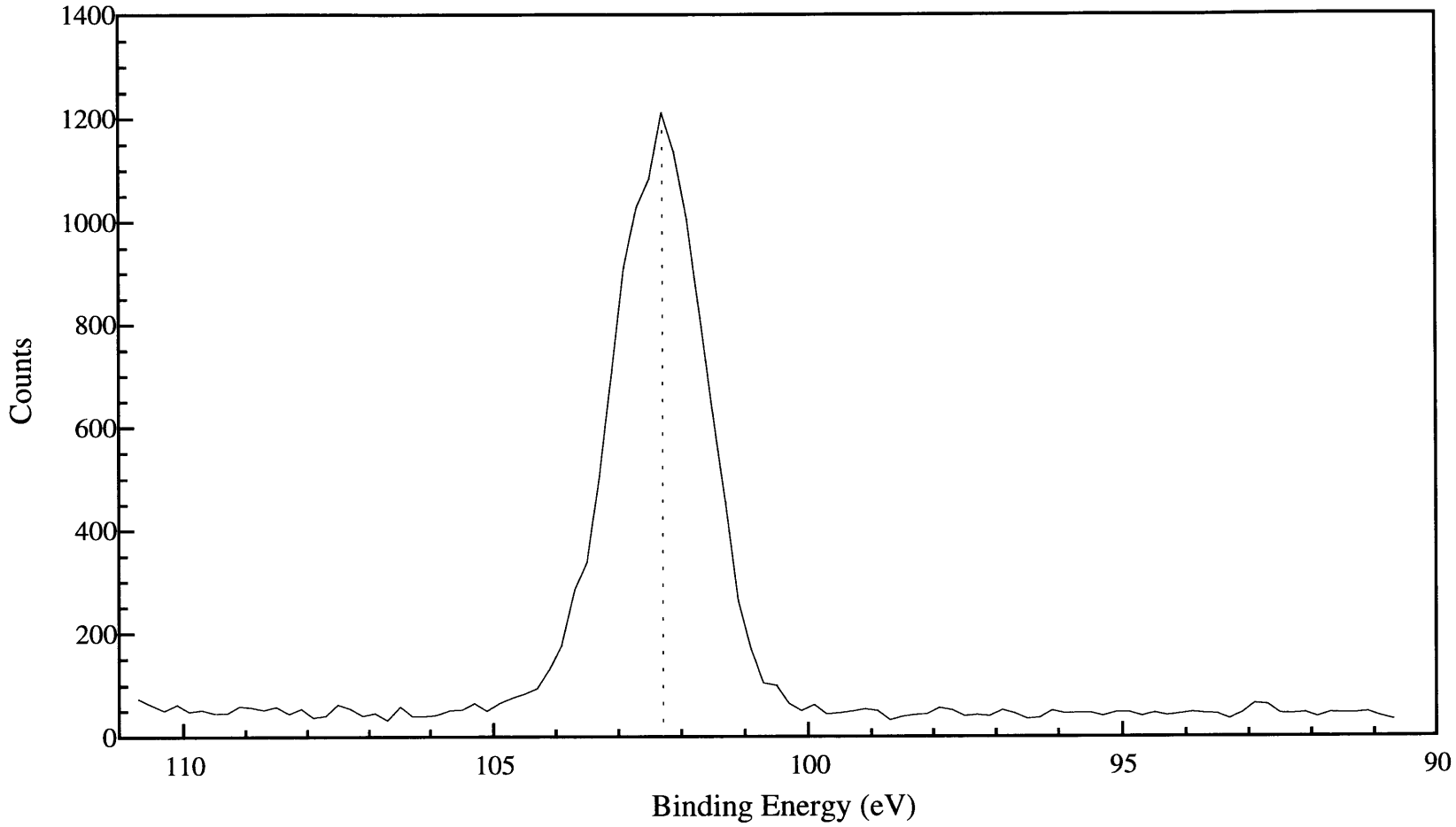

Figure 6-9: High resolution Si 2p XPS spectrum of PDMS sample B (see Tab. 6-1)

(Spectrum has been charged corrected by +5.7 eV with reference to the C 1s peak at 285.6 eV)

6.2.3 Elemental analysis

Additional elemental analysis was done by Galbraith Laboratories, an outside testing lab, to check the XPS results and to test for the H content. Approximately 19 mg of material deposited at P = 0.6 Torr, T_f = 520 °C, and d_{fs} = 10.5 mm along with a quantity of the PDMS secondary standard were sent for Si analysis by inductively coupled plasma emission spectroscopy (ASTM E1479-92) and C plus H analysis by combustion (ASTM D5291-92). The remaining material in a sample was assumed to be O. While the results shown in Table 6-4 appear to be quite different from those in Tab. 6-3, it can be explained by a systematic error in the measurement of the Si content. If the %Si for the PDMS secondary standard is adjusted so that the Si:O molar ratio is 1:1, then the composition of the standard is correct at $SiOC_2H_{6.1}$. Doing the same for the HFCVD sample gives a composition of $SiOC_{1.2}H_{3.8}$ which is lower than any of the XPS result. The general trend of these results, however, are consistent with the FTIR results which imply that complete methyl groups were lost off of the Si-O backbone.

Table 6-4: Elemental analysis of HFCVD sample and PDMS standard (Si by ICPES, C & H by combustion plus CO_2 and H_2O detection, O assumed to be remainder)

Sample	H	C	Si	O
PDMS secondary stnd	7.04	2.27	1	1.43
HFCVD material	4.63	1.42	1	1.60

6.2.4 ^{29}Si nuclear magnetic resonance (NMR) spectroscopy

A home built nuclear magnetic resonance spectrometer[19] with a ^{29}Si resonance frequency of 53.64 MHz was used to probe the chemical nature of the silicon nuclei in the pyrolytic films through cross-polarization / magic-angle spinning (CP / MAS) solid state

^{29}Si NMR. Two films were deposited at a pressure of 0.6 torr, a filament power of 120W, and a filament-to-substrate distance of 10.5 mm for two hours each in order to accumulate enough material for analysis. Approximately 60 milligrams were scraped off of the silicon substrates, mixed with alumina as a filler, and packed into a rotor which was spun at 3.5 kHz. The spectrum shown in Figure 6-10 was collected in a Chemagnetics 7.5 mm, double resonance, MAS probe using a 7 μs 90° pulse followed by 3 ms cross polarization contact time. A total of 512 signal averages with a 20 μs dwell time and a 20 s recycle delay were used. Note that unlike direct excitation NMR, the area under the peaks in CP spectra cannot be directly compared to give quantitative relative concentration information.

A listing of some of the many possible functional groups and their chemical shifts from the literature is shown in Table 6-5. The two main peaks in our spectrum occur at -8 and -19 ppm. The peak at -19 ppm corresponds to the Si in a dimethylsiloxane unit. As

Table 6-5: Literature values for various functional groups and their ^{29}Si NMR chemical shifts relative to TMS

Chemical group	Chemical shift (ppm)	References
$(CH_3)_3Si–O–$	+6 to +11	Assink *et al.*,[20] Engelhardt *et al.*[21]
$(CH_3)_4Si$	0	zero reference
$–O–(CH_3)_2Si–O–$	-18 to -23	Assink *et al.*,[20] Engelhardt *et al.*[21]
$–O–(CH_3)\underset{\displaystyle O}{\overset{\displaystyle |}{Si}}–O–$	-55 to -68	Assink *et al.*,[20] Horn *et al.*[22]
$–O–\underset{\displaystyle O}{\overset{\displaystyle |}{\overset{\displaystyle |}{\overset{\displaystyle O}{\overset{\displaystyle |}{Si}}}}}–O–$	-99 to -109	Assink *et al.*,[20] Tajima *et al.*[23]
$(CH_3)_2HSi–O–$	-5	Assink *et al.*,[20] Mileshkevich *et al.*[24]
$–O–(CH_3)HSi–O–$	-33 to -39	Assink *et al.*,[20] Horn *et al.*[25]

one can see from the spectra for pure D_4 and the PDMS secondary standard in Figures 6-11 and 6-12, respectively, this peak can shift from -18 ppm to -23 ppm. Like in the published spectra for PP films, this peak is the most prominent. In PP films from D_4, there are two other significant peaks at ~10 ppm and ~ -60 ppm corresponding to $(CH_3)_3Si–O–$ and $(CH_3)Si–(O)_3–$ groups, respectively; see Figure 6-13.[13] Both of these types of Si are present in our films as well but at barely detectable levels.

The peak in our spectrum at -8 ppm is in the range typically assigned to a terminal $(CH_3)_2HSi–O–$ group or a siloxane unit with a vinyl group attached. The latter has been ruled out by the lack of CH_2 absorptions in the IR spectra while the former was checked by a CP contact time experiment in which the effect of varying the contact time on the relative intensity of the two main peaks was monitored. Because the peaks did not display different responses as the contact time was increased, the -8 ppm peak is not likely to be from any functional groups with Si-H bonds. Also, considering the loss of methyl groups indicated by the IR and XPS spectroscopies, it seems unlikely that a significant concentration of $(CH_3)_2HSi–$ groups could be present without some detectable levels of $–O–(CH_3)HSi–O–$ (~ -36 ppm) as well.

Another possible source of a chemical shift in the range between 0 and -10 ppm is from D_3, the solid cyclic trimer, which we determined has a shift of -9 ppm. The spectrum for D_3 dissolved in acetone is shown in Figure 6-14. To check for the presence of D_3, the pyrolytic sample was heated to 135 °C in air for 30 minutes. Since D_3 has a boiling point of ~134 °C, such a heat treatment should remove most if not all traces of the trimer. Because the sample was mixed with alumina to pack the rotor, no significance could be

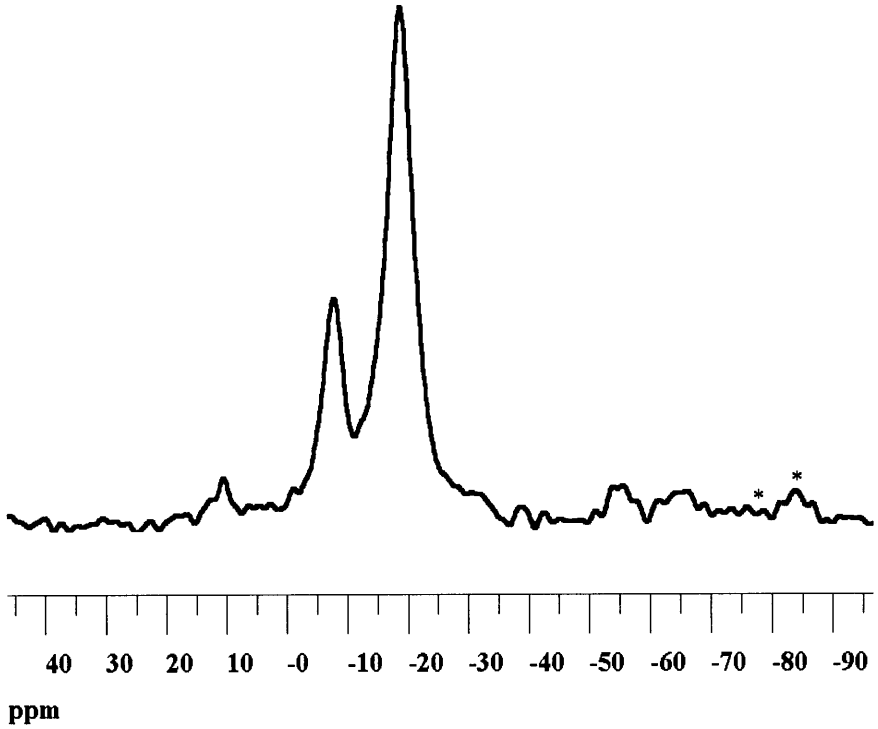

Figure 6-10: ^{29}Si NMR spectrum of an as deposited pyrolytic PDMS film
(* = spinning side bands)

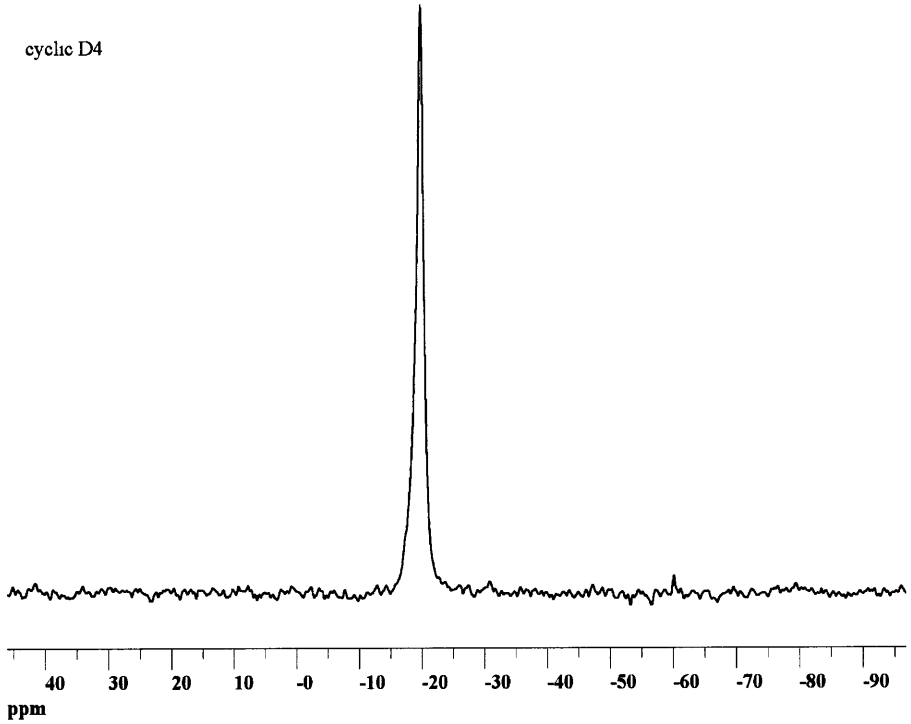

Figure 6-11: ^{29}Si NMR of octamethylcyclotetrasiloxane (D_4)

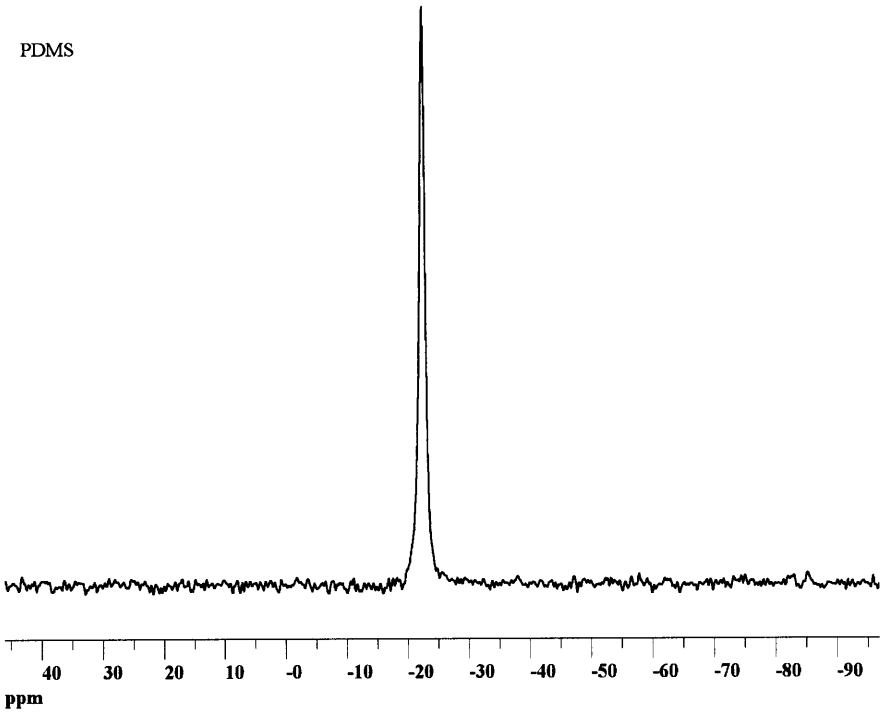

Figure 6-12: ^{29}Si NMR of polydimethylsiloxane (PDMS) secondary standard

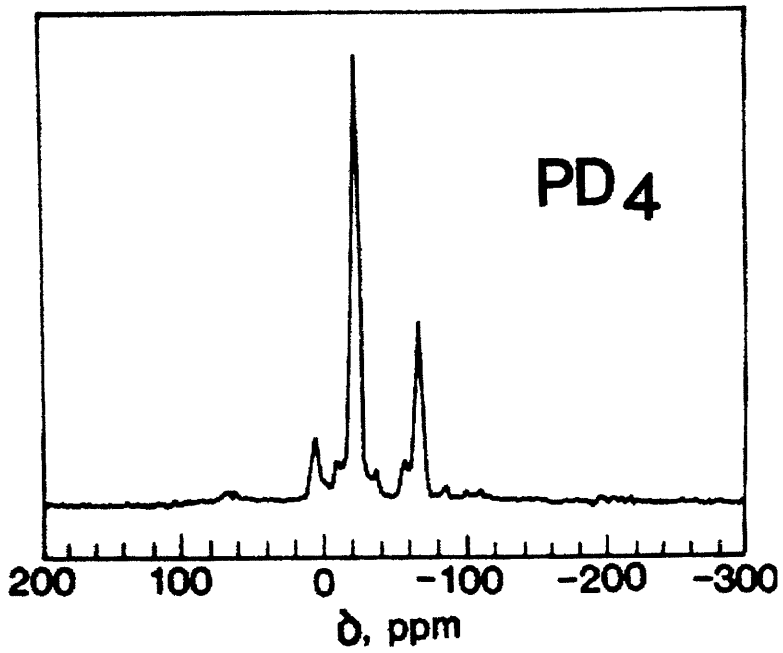

Figure 6-13: ^{29}Si NMR spectrum for plasma polymerized D_4 film

From I. Tajima, and M. Yamamoto, *J. Polym. Sci. Polym. Chem.*, **25**, 1737-1744 (1987)

attributed to the slight weight loss in the sample upon cooling. The NMR spectrum in Figure 6-15 shows that the heat treatment had no effect on the sample.

Yet another possible source for the signal at -8 ppm is the presence of **(1)** $-O-(CH_3)_2Si-Si(CH_3)_2-O-$ or **(2)** $-(O)_2-(CH_3)Si-Si(CH_3)-(O)_2-$ groups. The existence of such Si-Si crosslinks is in agreement with the methyl loss shown by FTIR and XPS and does not contradict the ^{29}Si NMR data. Furthermore, because the high resolution Si 2p XPS spectra have indicated that no significant concentration of any oxidation states besides Si^{2+} are present, we can very likely rule out **(1)**, the head-to-tail dimethylsiloxane unit, which only has single oxidation state Si's. However, since no literature references for the chemical shift of **(2)** have been found, this assignment is tentative.

6.3 Discussion

6.3.1 Film structure

The general picture of the film structure which develops from the IR, XPS, and NMR results is of "long" siloxane chains or rings of more than about 10 units. The lack of a significant concentration of terminal Si groups in the NMR also supports this conclusion. The hardness of the films imply that they are crosslinked in some fashion. The absence of vinyl absorptions in the IR, however, seem to indicate that there are no C-C crosslinks such as in conventional, peroxide crosslinked silicones while the lack of $-O-(CH_3)Si-(O)_2-$ groups in the NMR eliminates that functionality as a possible crosslinker. The proposed Si-Si crosslink is one possible answer to this puzzle which also explains the observed loss of methyl groups.

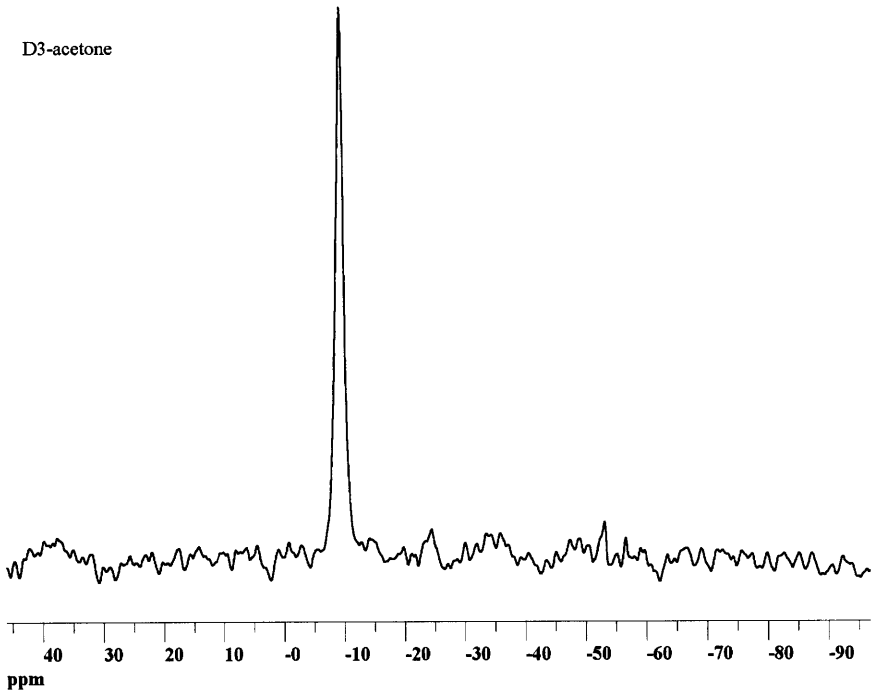

Figure 6-14: ^{29}Si NMR of hexamethylcyclotrisiloxane (D_3)

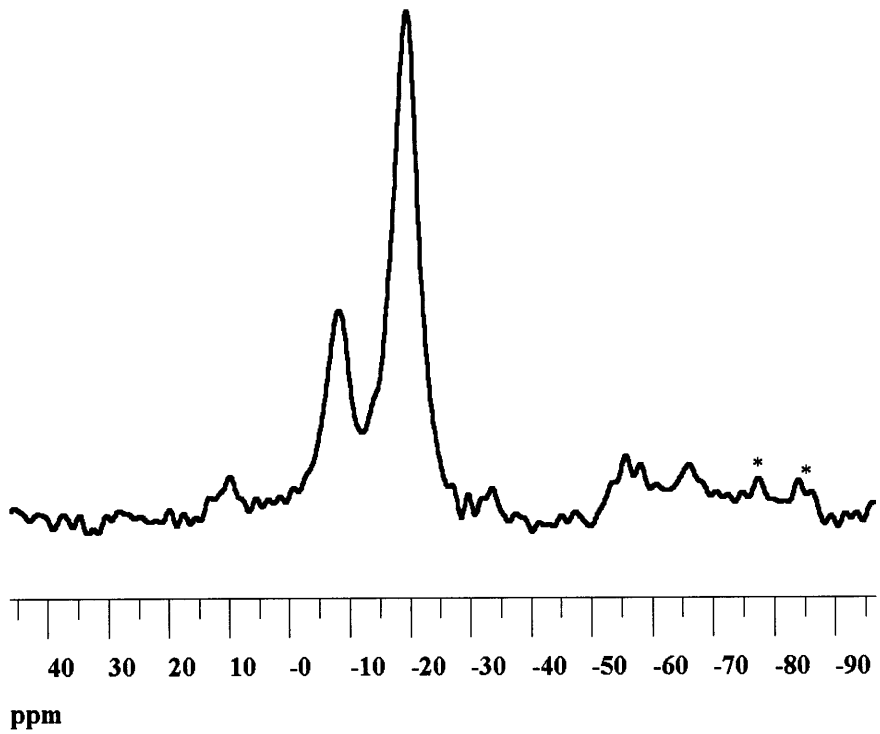

Figure 6-15: ^{29}Si NMR spectrum of the annealed pyrolytic PDMS sample
(* = spinning side bands)

6.3.2 Growth mechanism

In order to better understand the kinetics of this process, the deposition rate at several filament temperatures were plotted in Arrhenius form. Figure 6-16 is a graph of the natural log of the growth rate versus the reciprocal of the filament temperature for the two sets of films, A-D and 1-5. Separate linear fits to the data are shown. Apparent activation energies of $30.2 \pm 9.7 \frac{\text{kcal}}{\text{mole}}$ and $36.5 \pm 4.1 \frac{\text{kcal}}{\text{mole}}$ are calculated for films A-D and films 1-5, respectively.

We earlier postulated that a possible growth mechanism for the deposition process would involve a ring opening reaction analogous to that in the liquid-phase anionic polymerization followed by linear chain propagation. Such a ring opening reaction could be possible due to ring strain. From the observed temperature invariance of the equilibrium ratio of oligomers and polymers in the liquid phase polymerization of PDMS, it has been concluded that $\Delta H_{\text{liq polym}} \approx 0$.[27] If the enthalpy change for the gas phase reaction were similarly zero, then the analogous gas phase ring-opening reaction would have nearly equal activation energies for the thermal polymerization and depolymerization reactions. Thomas and Kendrick[28] have calculated an activation energy of $42 \pm 3 \frac{\text{kcal}}{\text{mole}}$ for the thermal degradation of a number of linear PDMS films in a vacuum.

Another possible reaction mechanism is based on a ring expansion mechanism postulated to explain the formation of oligomeric products in the PP of D_4.[29] A similar siloxane bond interchange mechanism has been proposed to account for the formation of large poly(dimethylsiloxane) rings (~3500 skeletal bonds) from the heat treatment under vacuum of smaller cyclic oligomers. Bannister and Semlyen heated a cyclic

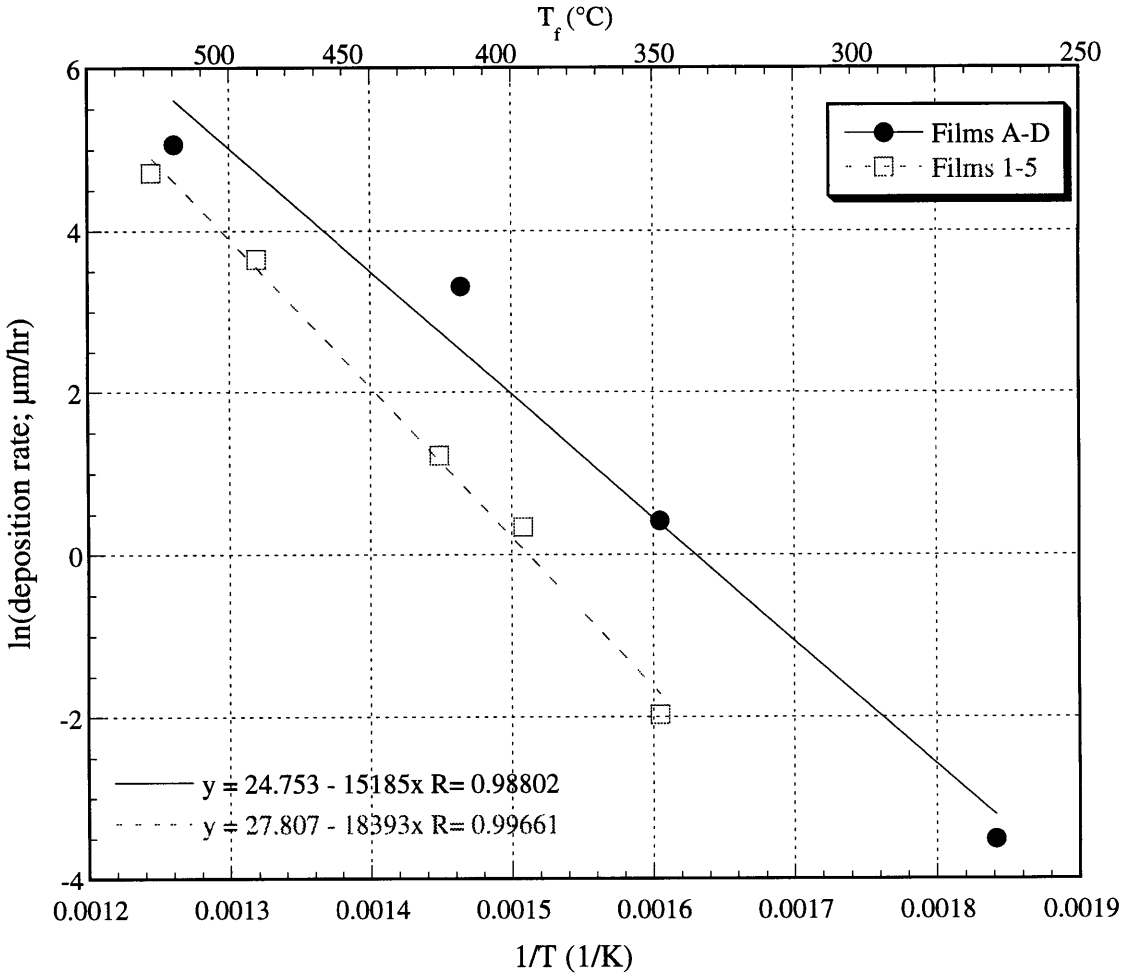

Figure 6-16: Arrhenius plot for the HFCVD PDMS deposition process

poly(dimethylsiloxane) with a nominal 145 skeletal bonds in an enclosed, evacuated Pyrex tube for three days at 668 K and found using gel permeation chromatography that the only two products were smaller cyclic oligomers and a much higher molecular weight fraction.[30] An example of the steps necessary to form a D_8 radical from D_4 radical is shown in Figure 6-17. Applied repeatedly, this mechanism would result in large rings that would have an IR signature similar to a long linear polysiloxane chain.

From work with a remote plasma deposition system, Rau and Kulisch have proposed that in the plasma polymerization of D_4, electron impact is responsible for initiating the fragmentation processes which lead to growth.[17] They base their conclusion on the linear increase in growth rate and enhanced long chain poly(dimethylsiloxane) IR signature (see Fig. 6-7) with increasing plasma power. However, unlike in a plasma deposition system where significant concentrations of ions and electrons exist, only uncharged molecular species are present in a pyrolytic process. Therefore this mode of growth is highly unlikely.

Mechanisms that call for the existence of smaller siloxane units (D_n, $n<4$) would also seem unlikely to occur at first glance because of the strength of the Si-O bond. Table 6-6 shows that many of the other bonds in the molecule would be broken before the Si-O bond breaks. However, pyrolysis studies at temperatures higher than that used in this work (766.5 to 842 K) have indicated that the stable gas phase decomposition products of D_4 at pressures of 0.5 to 13.5 torr are D_3 and D_5.[31] The suggested mechanism is the decomposition of D_4 to D_3 and an intermediate, D_1 (dimethylsilanone), followed by the reaction of D_1 with D_4 to give D_5 as the second stable product. The decomposition of D_4

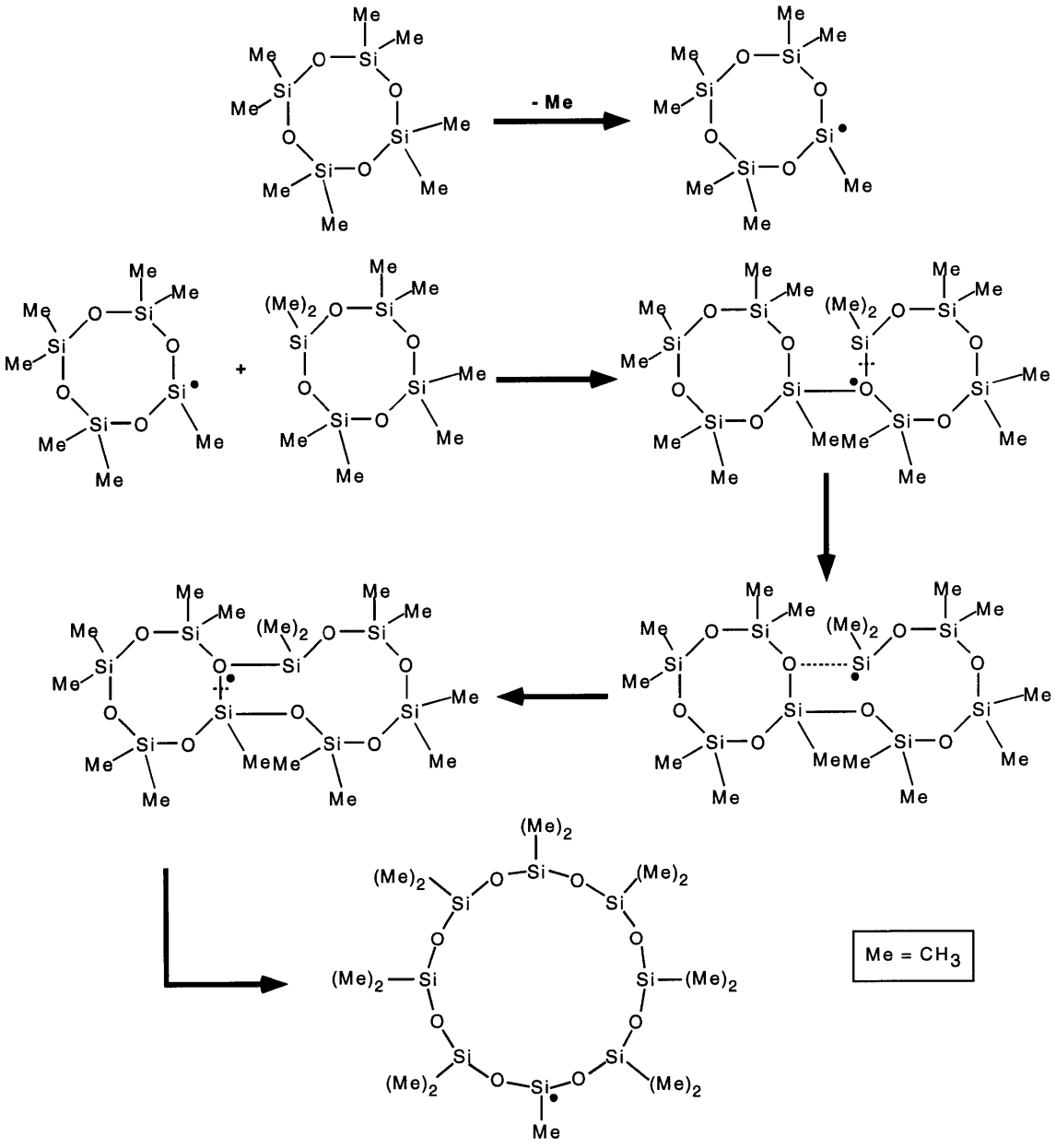

Figure 6-17: Proposed pyrolytic PDMS ring expansion growth mechanism.

Adapted from A. M. Wróbel, *et al.*, *J. Macromol. Sci.-Chem. A.*, **A20** (5-6), 583-618 (1983).

Table 6-6: Various bond strengths (Source: CRC Handbook of Chemistry and Physics)

	Si-Si	C-H	Si-C	Si-O
bond strength	78.1 kcal/mol	80.8 kcal/mol	107.9 kcal/mol	193.5 kcal/mol

may involve the formation of a bicyclic transition state (see Figure 6-18), accounting for the predominate cleavage of the Si-O bond as compared to the weaker Si-C bond.[32]

According to Davidson and Thompson, the rate constant for D_3 and D_1 formation in the early stages of D_4 pyrolysis (<4% decomposition) is:[31]

$$\log_{10}k/s^{-1} = (14.85\pm0.39) - (300.9\pm6.1)\ \text{kJ mol}^{-1}/2.303\ \mathbf{R}T$$

Even though this expression was based on higher temperature data and was found to be sensitive to trace oxygen contamination, it may still be enlightening to apply it to the HFCVD system. At a filament temperature of 550K, $k = 2.8\text{x}10^{-14}\ s^{-1}$. At 0.6 torr, the concentration of D_4 is approximately $8\text{x}10^{15}\ cm^{-3}$. The volumetric rate of D_1 formation is $kC_{D4} = 200\ cm^{-3}\ s^{-1}$. For a 10 minute deposition and a reactor volume of approximately $10^3\ cm^3$, a maximum of $1.2\text{x}10^8$ molecules of D_1 would be generated. If all of these molecules were to be incorporated into a film, it would still only result in $1.5\text{x}10^{-14}$ gm of material. While it is conceivable that the sensitivity to trace O_2 levels mentioned earlier could be a factor, the gas phase decomposition kinetics of D_4 indicate that, barring a correction factor of 10^{11}, the production of D_1 at the filament temperatures used in this work is insufficient to explain the observed growth rates by a very wide margin. In addition, the lack of evidence for $-O-(CH_3)_2Si-(O)_2-$ crosslinks and other rearrangements in the IR or ^{29}Si NMR which would result from a dimethylsilanone addition mechanism indicates that this type of reaction is unlikely to occur.

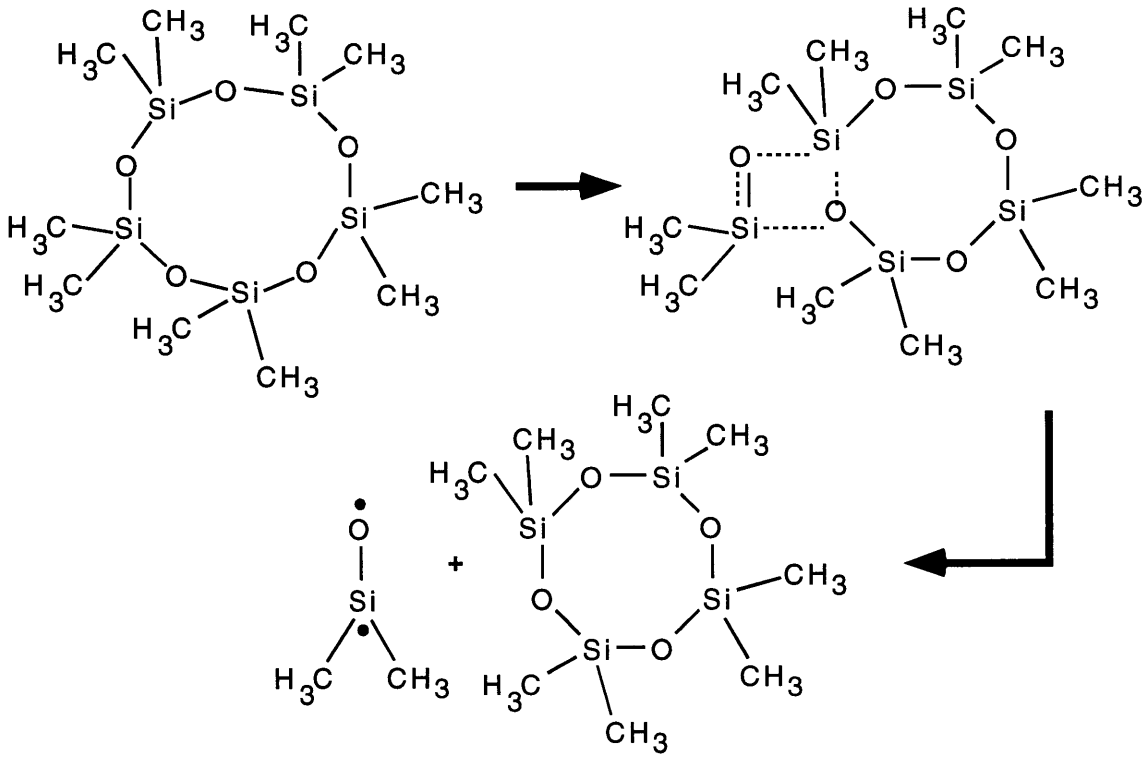

Figure 6-18: Bicyclic transition state postulated to be involved in thermal decomposition of D_5

Adapted from L. E. Gusel'nikov, N. S. Nametkin, T. K. Islamov, A. A. Sobtsov, and V. M. Vdovin, *Izvest. Akad. Nauk SSSR, Ser. Khimi.*, **1**, 84-89 (1971).

Based on the available spectroscopic data, distinguishing between the ring opening / linear chain growth and the ring expansion mechanisms is fairly difficult since such long range structural information is not probed by these techniques. One can infer, however, from the small peak at +10 ppm on the ^{29}Si NMR spectra that there is a small concentration of terminal $(CH_3)_3Si–O–$ groups. Since the ring expansion mechanism does not generate any terminal groups at all, this suggests that the long linear chain mechanism is a slightly better match to the spectroscopic data.

Finally, the loss of methyl groups from the Si-O backbone shown by the various characterization methods suggests that two chains or rings could crosslink at the radical sites opened by the breaking of Si-C bonds. The elemental composition $SiOC_{1.5}H_{4.5}$ would result if, on average, two methyl groups were lost off of every D_4 molecule. The C:Si ratio from the XPS analysis was 1.4 - 1.6. A schematic representation of the final proposed pyrolytic CVD film structure is shown in Figure 6-19.

Acknowledgements:

I would like to thank Hilton Pryce Lewis for his help in depositing some of the films used for characterization in this work and Yuan Lu of the Harvard XPS Facility for his help with the XPS spectroscopy. I would especially like to thank Kenneth Lau for his assistance in running and interpreting the ^{29}Si NMR results.

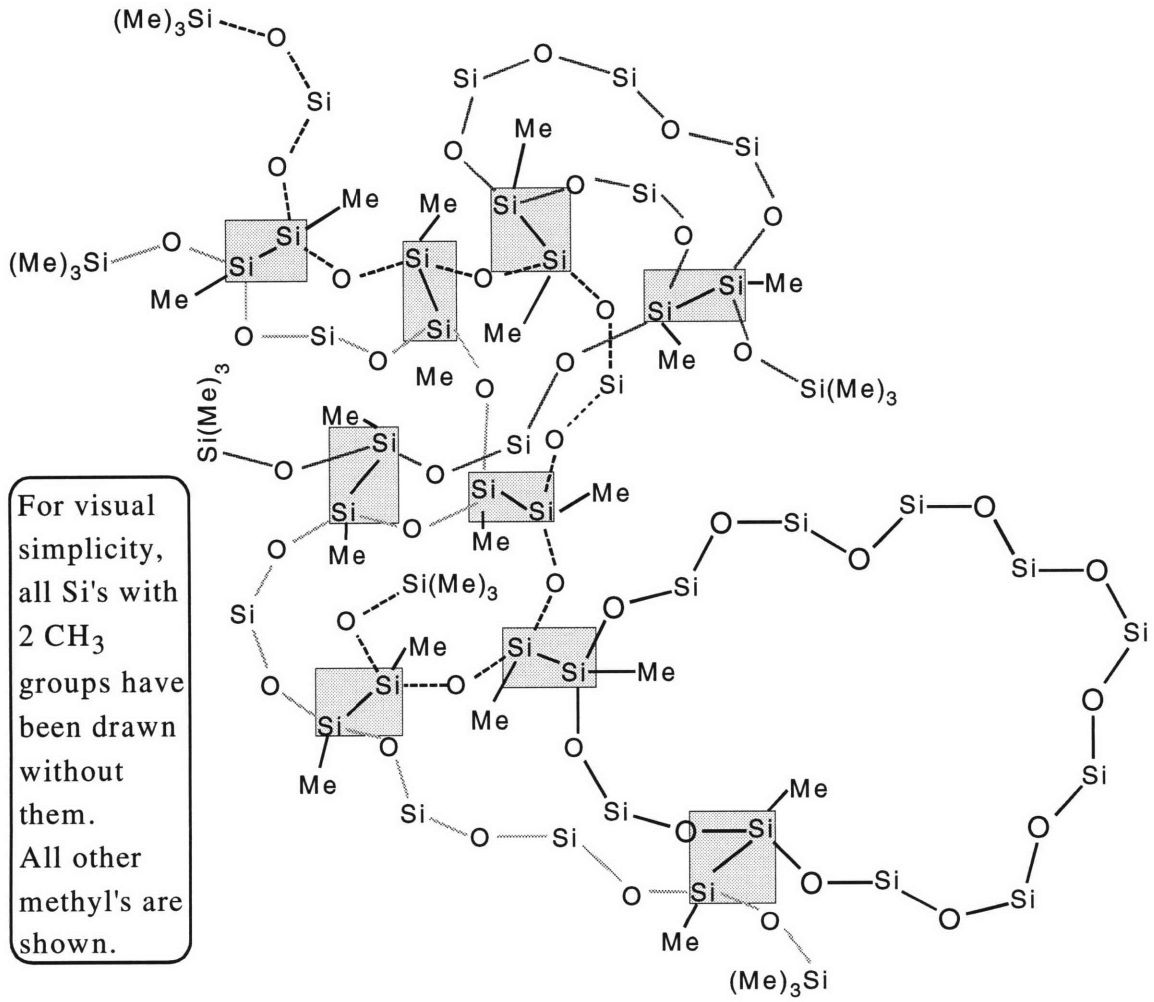

Figure 6-19: Schematic of proposed pyrolytic polyorganosiloxane film structure

(Proposed Si-Si crosslinks are highlighted)

References:

1. T. J. Gair, *Silicone Technology*, ed. by P. F. Bruins. Wiley: New York. 1970. pp 1-6.
2. A. S. Chawla, *Biomaterials*, **2**, 83-88 (1981).
3. J. Sakata, M. Yamamoto, and M. Hirai, *J. Appl. Polym. Sci.*, **31**, 1999-2006 (1986).
4. P. K. Tien, *Rev. Mod. Phys.*, **49**, 361-420 (1977).
5. M. R. Wertheimer, and T. S. Ramu, U.S. Patent No. 4,599,578 (1986).
6. T. Wydeven, *Appl. Opt.*, **16**, 717-721 (1977).
7. A. M. Wróbel, and M. R. Wertheimer, *Plasma Deposition, Treatment, and Etching of Polymers*, ed. by R. d'Agostino. Academic Press: San Diego. 1990. pp 163-268.
8. H. Yasuda, and T. Hsu, *J. Polym. Sci. Polym. Chem.*, **15**, 81-97 (1977).
9. S. J. Limb, C. B. Labelle, K. K. Gleason, D. J. Edell, and E. F. Gleason, *Appl. Phys. Lett.*, **68** (20), 2810-2812 (1996).
10. Y. Segui, and A. Bui, *J. Appl. Polym. Sci.*, **20**, 1611-1618 (1976).
11. A. M. Wróbel, M. R. Wertheimer, J. Dib, and H. P. Schreiber, *J. Macromol. Sci.-Chem. A.*, **14**, 321-337 (1980).
12. K. M. McNamara, B. E. Scruggs, and K. K. Gleason, *Thin Solid Films*, **253**, 157-161 (1994).
13. I. Tajima, and M. Yamamoto, *J. Polym. Sci. Polym. Chem.*, **25**, 1737-1744 (1987).
14. N. Wright, and M. J. Hunter, *J. Am. Chem. Soc.*, **69**, 803-809 (1947).
15. E. A. B. Ebsworth, M. Onyszchuk, and N. Sheppard, *J. Chem. Soc.*, , 1453-1460 (1958).
16. D. R. Anderson, *Analysis of Silicones*; **vol. 41**, ed. by A. L. Smith. Wiley & Sons: New York. 1974. pp 407.
17. C. Rau, and W. Kulisch, *Thin Solid Films*, **249**, 28-37 (1994).
18. C. R. Brundle, *Encyclopedia of Materials Characterization*, ed. by C. R. Brundle, J. Charles A. Evans, and S. Wilson. Butterworth-Heinemann: Boston. 1992. pp 282-299.
19. W. K. Chang, M. Y. Liao, and K. K. Gleason, *J. Phys. Chem.*, **100**, 19653-19658 (1996).
20. R. A. Assink, A. K. Hays, R. W. Bild, and B. L. Hawkins, *J. Vac. Sci. Technol. A*, **3** (6), 2629-2633 (1985).
21. G. Englehardt, H. Jancke, M. Mägi, T. Pehk, and E. Lippmaa, *J. Organometal. Chem.*, **28**, 293-300 (1971).
22. H.-G. Horn, and H. C. Marsmann, *Makromol. Chem.*, **162**, 255-267 (1972).

23. I. Tajima, and M. Yamamoto, *J. Polym. Sci. Polym. Chem.*, **23**, 615-622 (1985).

24. V. P. Mileschkevich, V. O. Reikhsfeld, A. I. Suprunenko, V. A. Pestunovich, M. R. Larin, and M. G. Voronkov, *Dokl. Akad. nauk SSSR*, **231** (5), 1134-1137 (1976).

25. H. G. Horn, and H. C. Marsmann, *Makromol. Chem.*, **46**, 1399 (1967).

26. R. W. LaRochelle, J. D. Cargioli, and E. A. Williams, *Macromolecules*, **9** (1), 85 (1976).

27. H. R. Allcock, *Heteroatom Ring Systems and Polymers*. Academic Press: New York. 1967.

28. T. H. Thomas, and T. C. Kendrick, *J. Polym. Sci., Pt. A-2: Polym. Phys.*, **7**, 537-549 (1969).

29. A. M. Wróbel, M. Kryszewski, and M. Gazicki, *J. Macromol. Sci.-Chem. A.*, **A20** (5-6), 583-618 (1983).

30. D. J. Bannister, and J. A. Semlyen, *Polymer*, **22**, 377-381 (1981).

31. I. M. T. Davidson, and J. F. Thompson, *J. Chem. Soc., Faraday Trans. 1*, **71**, 2260-2265 (1975).

32. L. E. Gusel'nikov, N. S. Nametkin, T. K. Islamov, A. A. Sobtsov, and V. M. Vdovin, *Izvest. Akad. Nauk SSSR, Ser. Khimi.*, **1**, 84-89 (1971).

7. SILICONE CVD GROWTH MODELING

In studying a new CVD process, there are several approaches that can be taken including film characterization, gas phase diagnostic / measurement, atomistic simulation, and macroscopic phenomenological modeling. This last approach can provide new insights into the nature of the deposited film as well as the deposition process through information on the reaction and transport processes involved in the film growth. Because the individual processes involved in the HFCVD of silicone are qualitatively similar to those in the HFCVD of diamond; namely, activation / dissociation of a growth species at a hot-filament followed by gas phase diffusion, and then reaction at a cooler surface, the finite difference diamond growth model from Chapter 5 was applied to the silicone deposition system.

The goal in this case is similar to the diamond CVD case; namely, to determine the extent to which either transport or kinetic processes limit growth at the surface by calculating the Damköhler number from a fit of the model to measured growth rates. Another goal of this analysis is to infer, if possible, the nature of the growth limiting species from k_s, the first order surface reaction rate constant and D, the diffusion coefficient, and C_f, the concentration of growth precursor at the filament. While it is not clear *a priori* if all three parameters can be uniquely determined, this approach should at least provide some bounds on them.

7.1 Experimental setup and deposition results

In order to reduce the geometric complexity of the model, a single straight filament was used in place of the serpentine configuration which was previously employed for the film characterization studies. Figure 7-1 shows a schematic of the new setup.

Exactly 3¾" of a 1 mm diameter tantalum wire was shaped into a straight filament with curved ends as shown in Figure 7-2. The bent sections of the filament allow for thermal expansion of the filament as it heats up without distorting the central straight section which would alter the filament to substrate standoff as well as destroy the symmetry of the setup. Polyorganolsiloxane deposition from the pyrolytic decomposition of octamethylcyclotetrasiloxane (D_4) was carried out at three different conditions with this new geometry. The first was to establish that a reasonable growth rate could be achieved with a set of baseline conditions: the filament resistively heated to approximately 280 °C with 72 W of power, the pressure held at 0.6 torr by adjusting the exit throttle valves, and the spacing between the bottom of the filament and the silicon substrate surface, d_{fs}, set to 1.00 cm. The film was deposited on a 2" Si (100) test grade wafer and growth was allowed to proceed for 15 minutes. The second condition diverged from the baseline conditions only in that the pressure was halved to 0.3 torr. The conditions for the last type of deposition varied from the baseline conditions by changing the filament-to-substrate distance from 10.0 mm to 4.9 mm. These variational runs were always immediately preceded by a baseline one to confirm that there was no drift in the reactor system.

The spatial thickness variation of all the films from these experiments were measured by a rotating polarizer ellipsometer (Gaertner L3W26C) instead of the nulling ellipsometer used in the film characterization studies because of difficulties in measuring

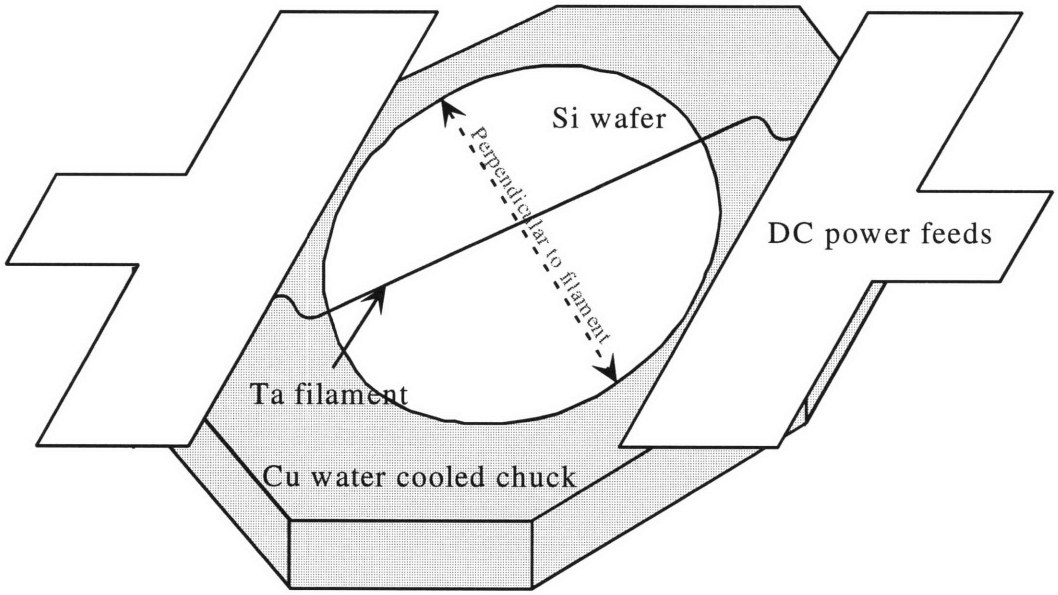

Figure 7-1: Modified straight filament geometry

Figure 7-2: Full scale representation of "straight" filament

the thick, sharply graded films with the nulling-type unit. In addition to measuring and reporting the ellipsometer parameters, Ψ and Δ, the ellipsometer also calculates the index of refraction, the film thickness, and the cycle thickness. However, because of local non-idealities in the film such as uniformity and transparency, the calculated indices of refraction tend to vary. The usual practice in such cases is to fix the index of refraction at an acceptable known value and to recalculate the now complex thickness and discard the imaginary portion so long as it is small in value relative to the real portion.[1] The thickness measurements for all these experiments have been recalculated based on an index of refraction of 1.40 at 632.5 nm and 1.39 at 830.0 nm using a Mathematica routine provided by Stephen Wasserman[2] which solves the following equations (see Appendix B for a complete listing).

$$r_{1p} = \frac{\tan\left[\phi - \sin^{-1}\left(\frac{n_0}{n_f}\sin(\phi)\right)\right]}{\tan\left[\phi + \sin^{-1}\left(\frac{n_0}{n_f}\sin(\phi)\right)\right]} \tag{7-1}$$

$$r_{1s} = -\frac{\sin\left[\phi - \sin^{-1}\left(\frac{n_0}{n_f}\sin(\phi)\right)\right]}{\sin\left[\phi + \sin^{-1}\left(\frac{n_0}{n_f}\sin(\phi)\right)\right]} \tag{7-2}$$

$$r_{2p} = \frac{\tan\left[\sin^{-1}\left(\frac{n_0}{n_f}\sin(\phi)\right) - \sin^{-1}\left(\frac{n_0}{n_m}\sin(\phi)\right)\right]}{\tan\left[\sin^{-1}\left(\frac{n_0}{n_f}\sin(\phi)\right) + \sin^{-1}\left(\frac{n_0}{n_m}\sin(\phi)\right)\right]} \tag{7-3}$$

$$r_{2s} = -\frac{\sin\left[\sin^{-1}\left(\frac{n_0}{n_f}\sin(\phi)\right) - \sin^{-1}\left(\frac{n_0}{n_m}\sin(\phi)\right)\right]}{\sin\left[\sin^{-1}\left(\frac{n_0}{n_f}\sin(\phi)\right) + \sin^{-1}\left(\frac{n_0}{n_m}\sin(\phi)\right)\right]} \tag{7-4}$$

$$\beta = \frac{2\,\pi\,d\,n_f \cos\left[\sin^{-1}\left(\frac{n_0}{n_f}\sin(\phi)\right)\right]}{\lambda} \tag{7-5}$$

$$\tan(\Psi)\, e^{i\Delta} = \left[\frac{r_{1p} + r_{2p}\, e^{-2i\beta}}{1 + r_{1p}\, r_{2p}\, e^{-2i\beta}}\right]\left[\frac{1 + r_{1s}\, r_{2s}\, e^{-2i\beta}}{r_{1s} + r_{2s}\, e^{-2i\beta}}\right] \tag{7-6}$$

where n_0 = index of refraction of surrounding medium (air)
n_f = index of refraction of film
n_m = index of refraction of reflecting substrate (Si)
ϕ = angle of incidence of light
λ = wavelength of incident light
d = film thickness
Ψ, Δ = measured ellipsometer parameters

In order to precisely determine the actual film thickness with ellipsometry, it is also necessary to determine which cycle thickness to use. The cycle thickness is calculated by:

$$t_{cycle} = \frac{\lambda}{2}\frac{1}{[n_f^2 - \sin^2\phi]^{1/2}} \tag{7-7}$$

and is a result of interference due to the periodic nature of the laser beam used in the measurement. By using more than one wavelength of light, it is possible to change the cycle thickness and, if not determine the precise cycle thickness, at least narrow down the choices. For this reason, a number of measurements were made in the same location with a red HeNe laser (632.5 nm) and an IR laser (830 nm). Furthermore, profilometry (Sloan Dektak 3) was used in the thicker areas of the film to measure the approximate film thickness so that the correct cycle could be determined.

Typically, the spatial variation of the film thickness across a 2" Si substrate was measured in small increments (either 0.1" or 2.0 mm) along a line through the center of the wafer in a direction perpendicular to the filament direction. Figure 7-3 is an example of the result of such a measurement on a trial wafer. In addition, the same sample was also measured along a line directly beneath the filament. The result of this measurement is

shown in Figure 7-4. Figure 7-5 shows the growth rate variation of the ½*P_{base} experiment along with the data from a baseline deposition for comparison while Figure 7-6 shows the data from the ½*d_{fs} experiment.

7.2 Model description and results

In order to model the spatial growth rate variations, the finite difference, diffusion-reaction diamond growth model from Chapter 4 was modified and applied. Because the measured growth rate directly beneath the filament as shown in Fig. 7-4 only varied by 10% over the central 3/5th's of the wafer, the model was simplified to two dimensions. This reduction not only facilitates calculation but also made interpretation of the result much easier.

7.2.1 Model description

Qualitatively, the diffusion-reaction model involves a constant concentration source which represents the heterogeneous reaction(s) at the hot filament coupled with simple Fickian diffusion, $\nabla^2 C=0$, and a first order reaction at the substrate surface, $\frac{\partial C}{\partial y} = k_s * Cl_{y=0}$. It is assumed that the diffusion coefficient, D, is not a function of position; i.e., that the temperature field is uniform. Assuming that the temperature profile is shaped similarly to that in diamond HFCVD, there will be sharp gradients in temperature at the filament and the cooled substrate. The remaining gas phase temperature would then range from about 500 K to 325 K and calculating D at T_{avg} would result in an error of at most 40% either way. It is further assumed that the reaction(s) at the filament are sufficiently fast to keep the gas phase concentration at the filament constant (pseudo-steady state assumption) and

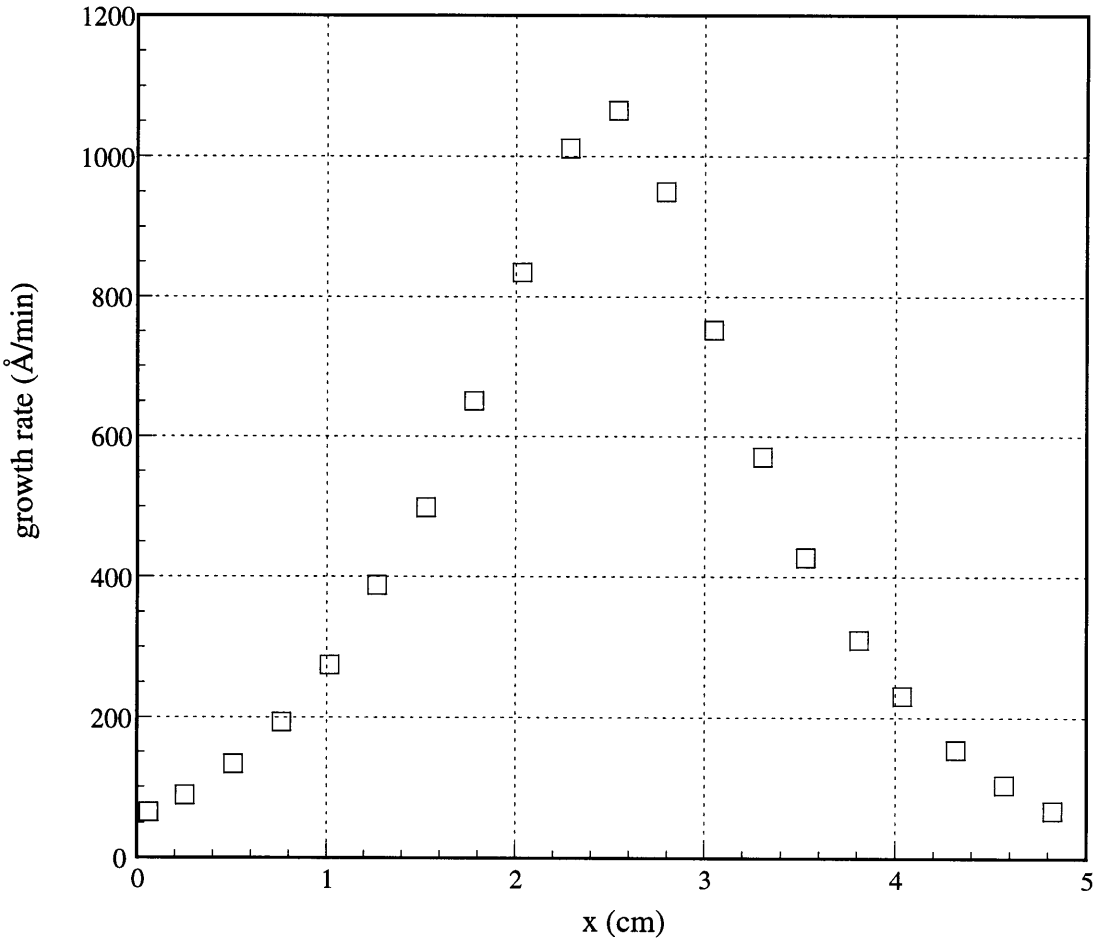

Figure 7-3: Trial case growth rate data across Si wafer through center in direction perpendicular to filament

(P=0.6 torr, d_{fs}=10.4 cm, filament power=69 W)

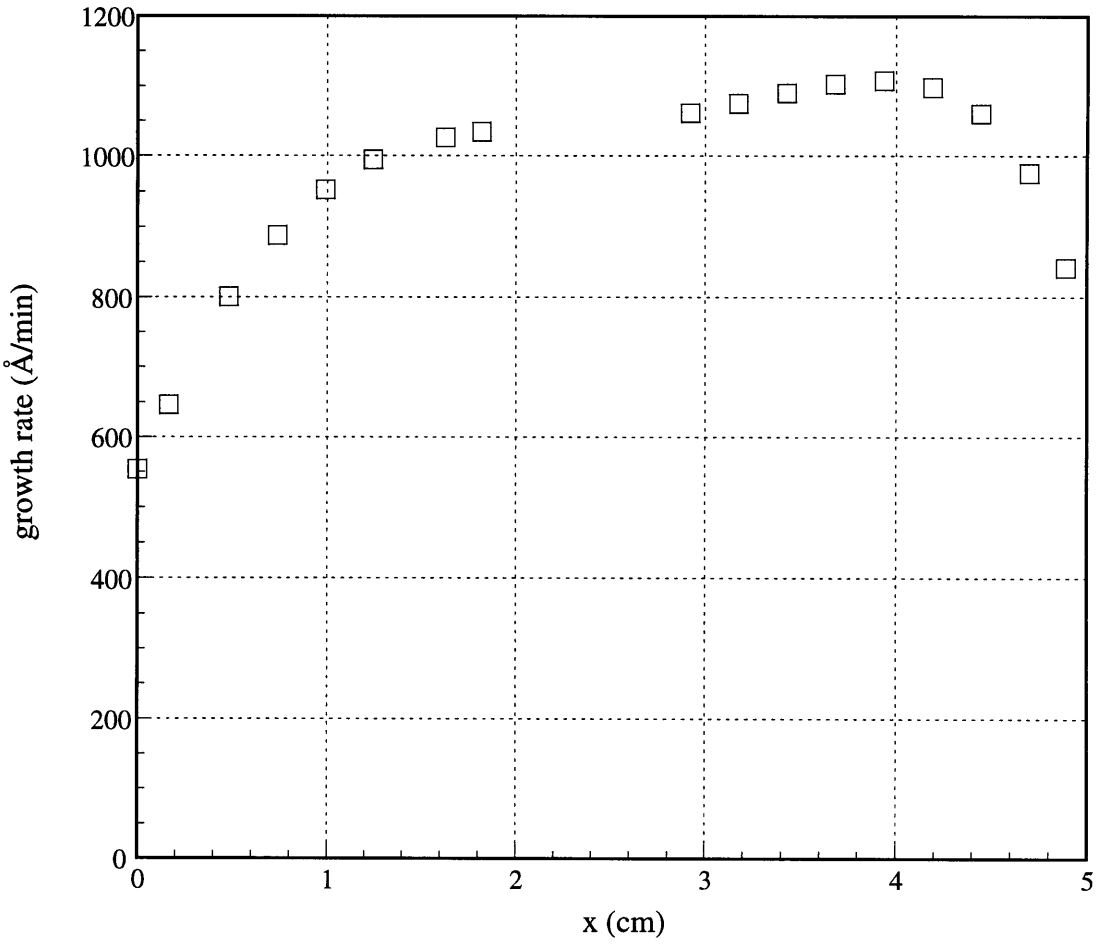

Figure 7-4: Trial case growth rate data across Si wafer through center directly beneath filament

(P=0.6 torr, d_{fs}=10.4 mm, filament power=69 W)

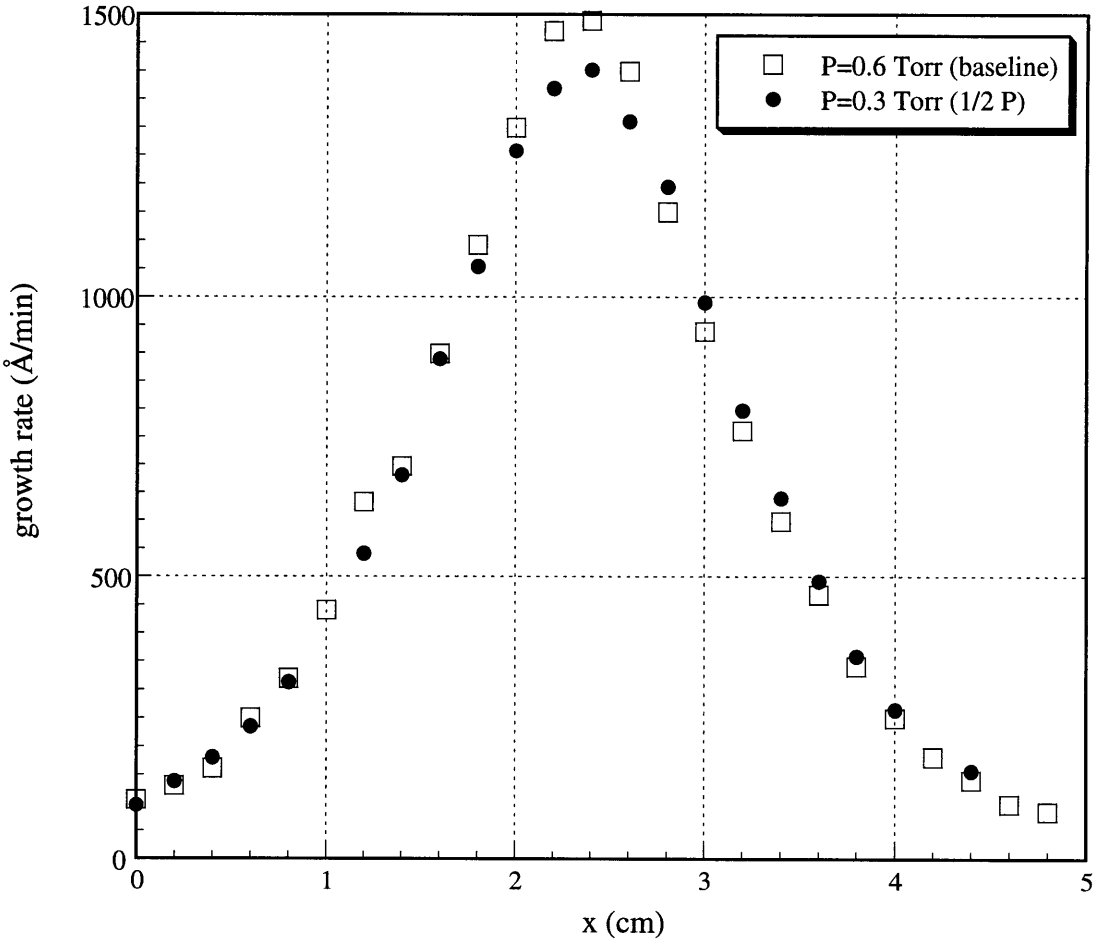

Figure 7-5: Deposition rates from a baseline experiment and a ½*P_{base} experiment

(P_{base}=0.6 torr, d_{fs}=10.0mm, filament power=72 W)

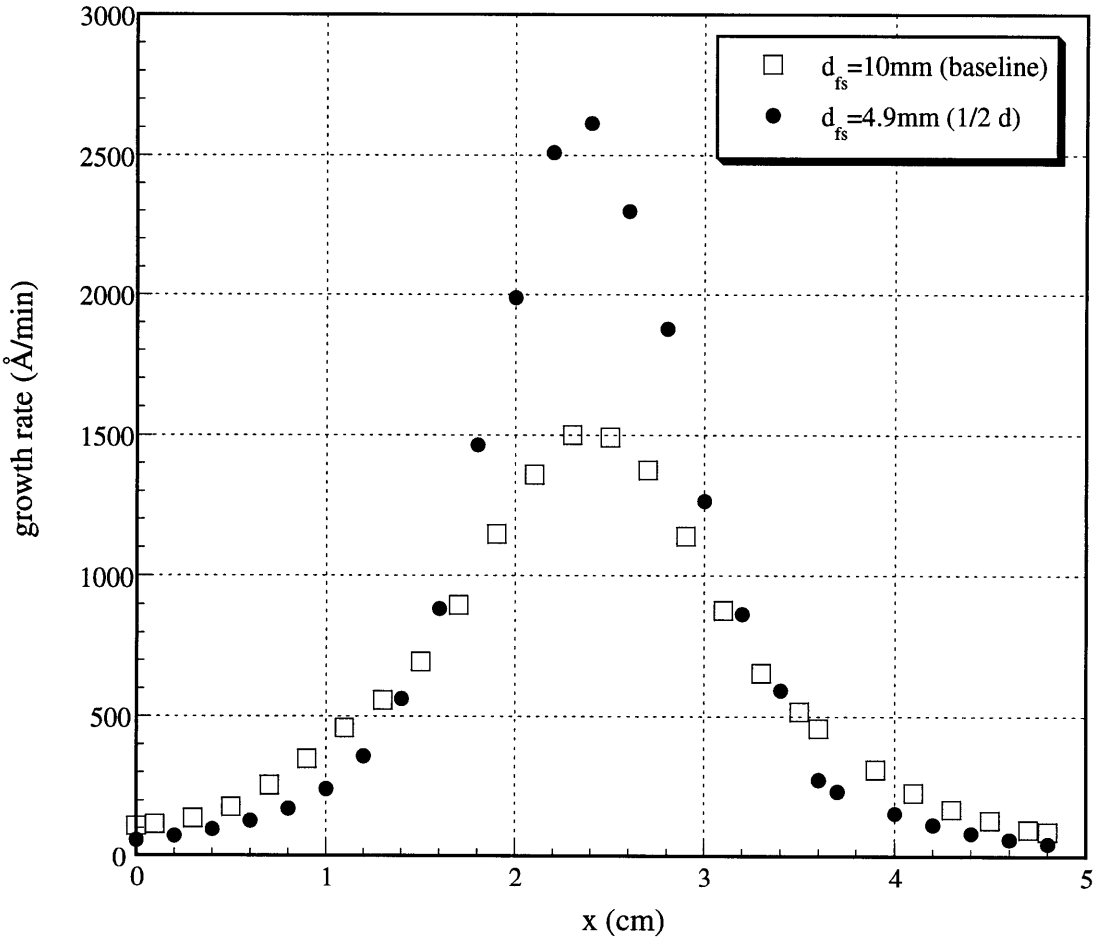

Figure 7-6: Deposition rates from a baseline experiment and a ½*$d_{fs,base}$ experiment

(P=0.6 torr, $d_{fs,base}$=10.0mm, filament power=72 W)

that convection is not a factor in the relatively small region between the filament and the Si wafer. At the wafer surface, it is assumed that the rate of desorption from surface sites is high relative to adsorption so that monolayer coverage never occurs. Otherwise, at monolayer coverage, the rate of reaction would no long depend on the gas phase concentration. Figure 7-7 displays a schematic representation of the model, including the finite difference grid and boundary conditions. The rectangular model region extends from the filament to the substrate in the y-direction and from the filament to a boundary at some distance past the edge of the substrate in the x-direction. The no-flux boundary conditions in the x-direction at the center of the wafer (x=0) and past the edge of the wafer (x=L) are due to a mirror plane and experimentally measured near-zero growth rates, respectively. The y-direction boundary conditions are due to a symmetry condition in the plane of the filament and the assumed first order reaction at the surface.

The mathematical details of the finite difference simulation were explained in Chapter 5 and will not be repeated here. The Matlab batch program which was used to run these particular simulation is listed in Appendix C.

Finally, one last aspect of the model setup should be explained. The choice of how far to extend the x=L boundary past the edge of the wafer was determined by a sensitivity analysis at a number of $k_m = \frac{k_s}{D}$ values. Figure 7-8 shows the simulated concentrations directly above the wafer surface for $k_m = 1\ cm^{-1}$ and three geometries: (1) the x=L no-flux boundary is at the edge of the wafer, (2) the boundary is 1 cm past the edge of the wafer, and (3) the boundary is 2 cm past the edge of the wafer. Figures 7-9 is the graph of the simulation results for $k_m = 100\ cm^{-1}$. While the differences between the three geometries

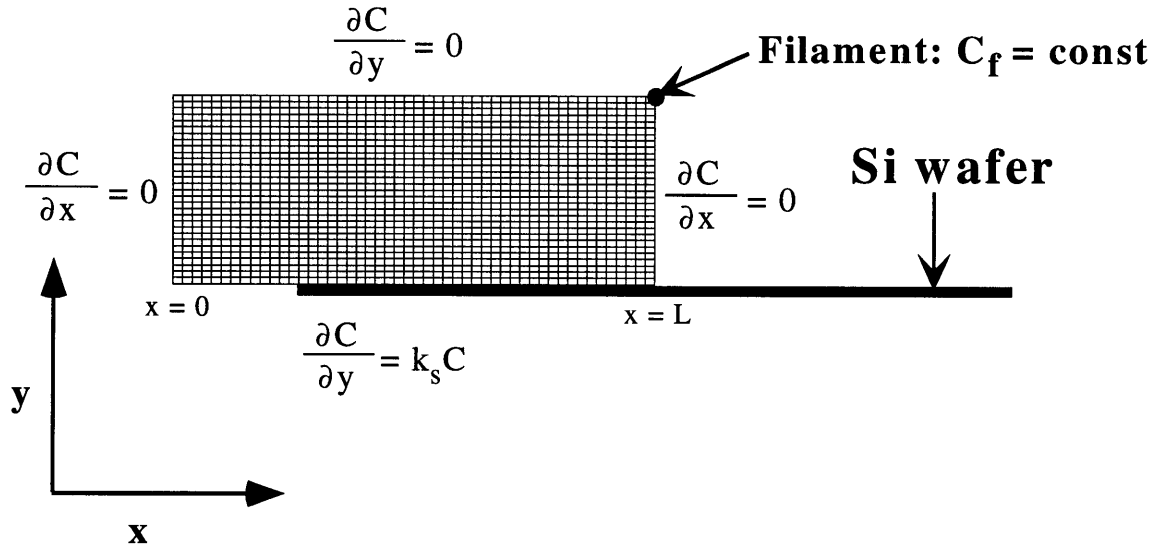

Figure 7-7: Details of the 2 dimensional PDMS HFCVD growth model

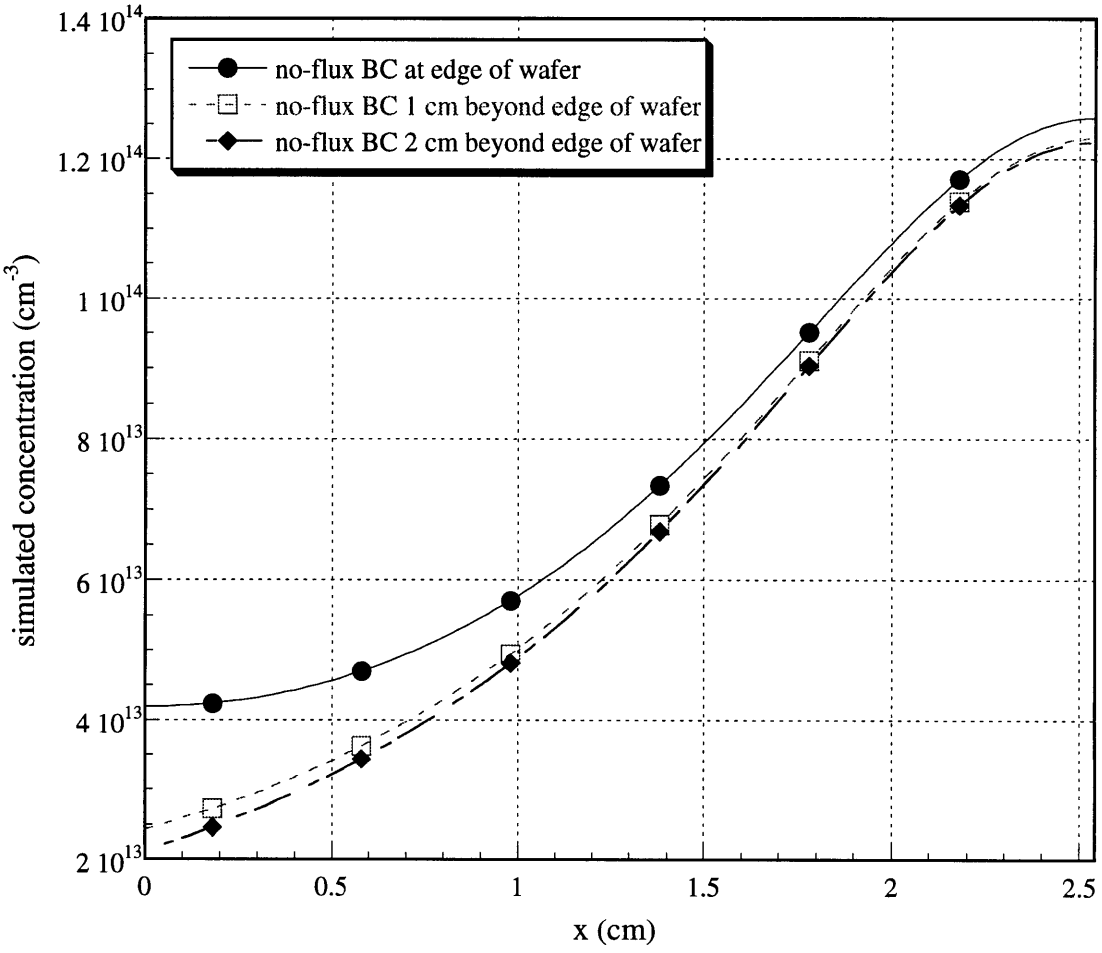

Figure 7-8: Simulated C_s results for k_m=1 cm^{-1} and three different boundary conditions: $\frac{\partial C}{\partial x} = 0$ at (1) the edge of the wafer, (2) 1 cm past the edge of the wafer, and (3) 2 cm past the edge of the wafer.

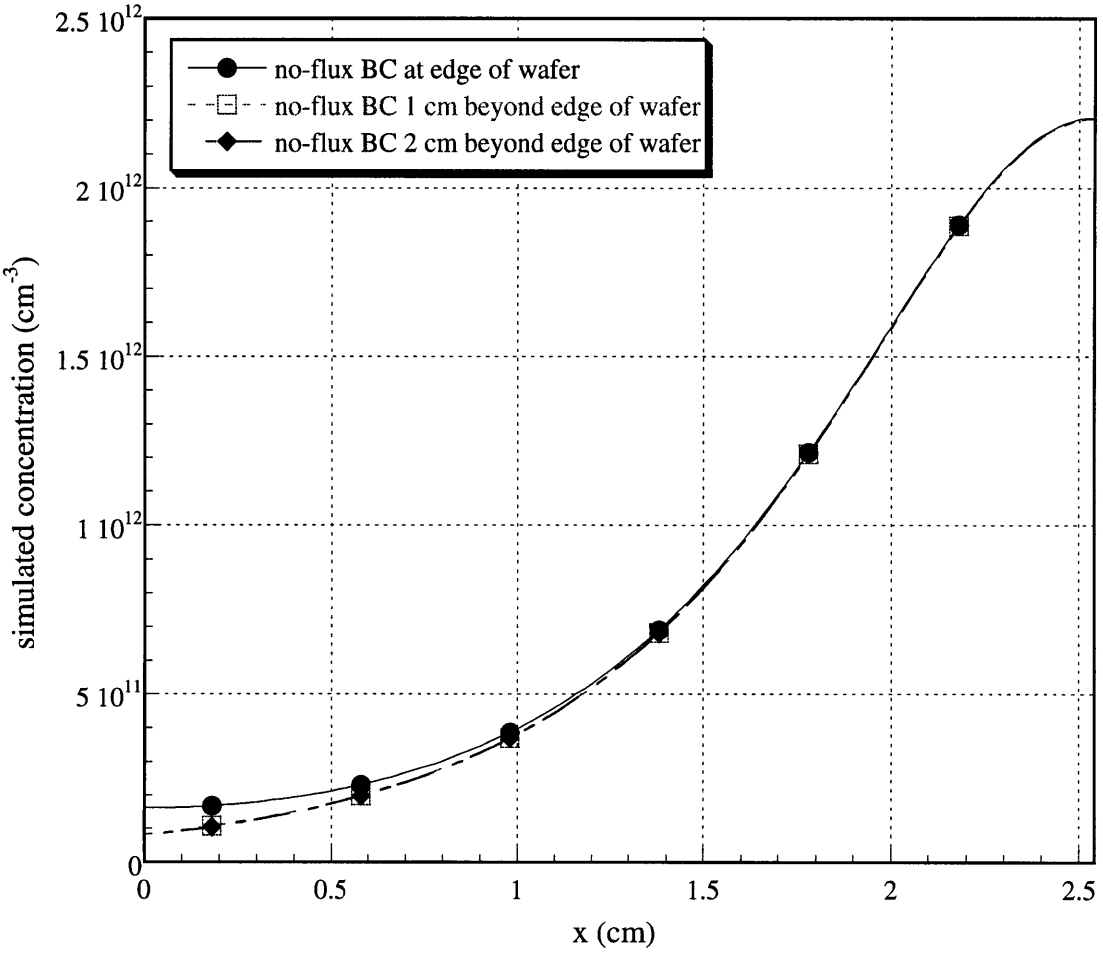

Figure 7-9: Simulated C_s results for k_m=100 cm^{-1} and three different boundary conditions: $\frac{\partial C}{\partial x} = 0$ at (1) the edge of the wafer, (2) 1 cm past the edge of the wafer, and (3) 2 cm past the edge of the wafer.

for k_m = 100 cm^{-1} are fairly small, there is still a noticeable difference between the cases where the boundary is at the wafer edge and at 1 cm out. For k_m = 1 cm^{-1}, that difference is till even greater. The difference between having the boundary at 1 cm and 2 cm past the edge of the wafer, however, is almost nonexistent for k_m = 100 cm^{-1} and fairly small for k_m = 1 cm^{-1}. In order to keep the computational expense to a minimal, that slight error was considered acceptable.

7.2.2 Model results

The baseline simulations were conducted for a reactor pressure of 0.6 torr, an assumed 10% dissociation at the hot filament, and a filament to substrate distance, d_{fs}, of 10.0 mm. At 0.6 torr, a 10% activation equals a constant concentration at the filament of $8x10^{14}$ cm^{-3}. The impact of this assumption will be taken up later in the Discussion section.

An example of the simulation result for the base case with k_m = 100 cm^{-1} over a 3.54 cm x 1.00 cm rectangular grid with a symmetric grid spacing of 0.02 cm is graphed in Figure 7-10. The x and y axes represent the spatial coordinates while the z-axis shows the concentration. The sharp spike in one corner of the plot is the fixed concentration at the filament. For the purposes of simulating the growth rate, the only part of the result that is needed is the concentration directly above the surface. C_s, the near-surface concentration directly above the wafer, for the case shown in Fig. 7-10 as well as for the two cases of k_m = 1 cm^{-1} and k_m = 10 cm^{-1} are plotted in Figure 7-11. Note that the region beyond the edge of the wafer is not shown. In addition to having markedly different maxima, each of the concentration profiles for the three cases simulated also have distinctly different shapes.

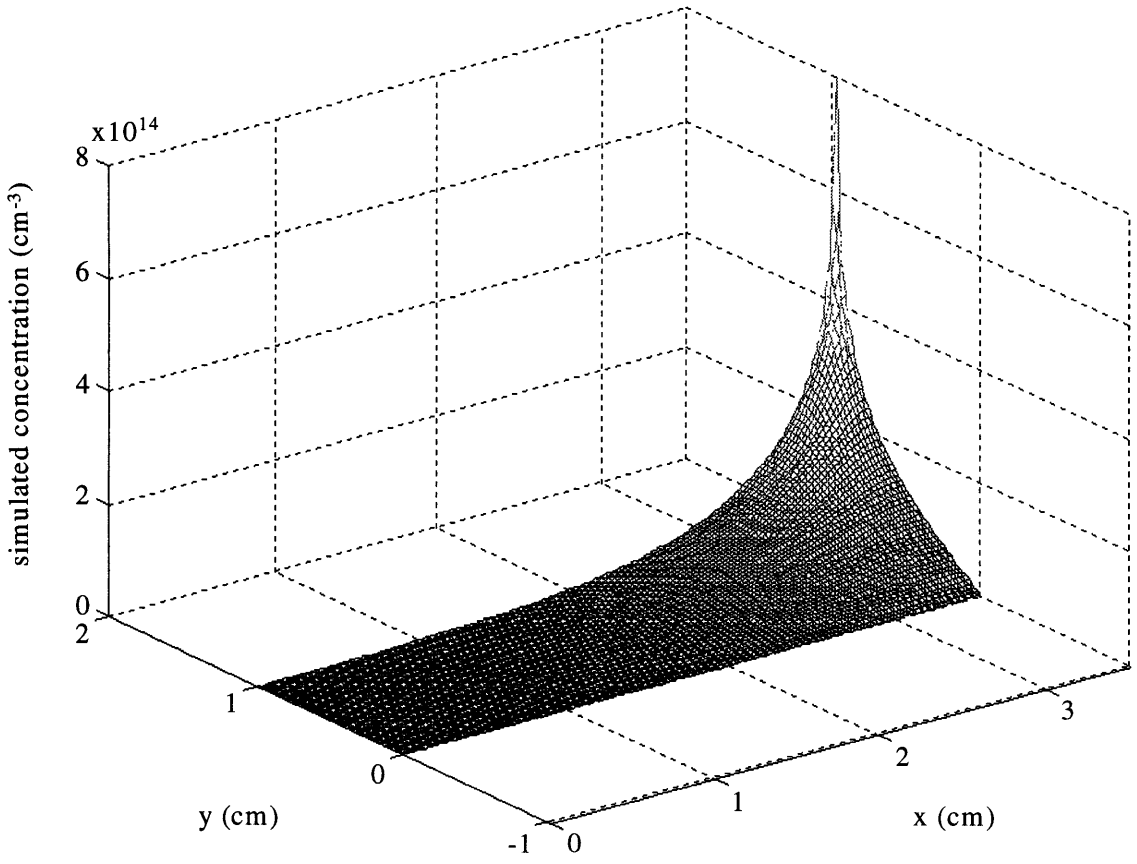

Figure 7-10: Baseline simulated gas phase concentrations for k_m=100cm^{-1} over a 3.54x1.00 cm^2 rectangular grid

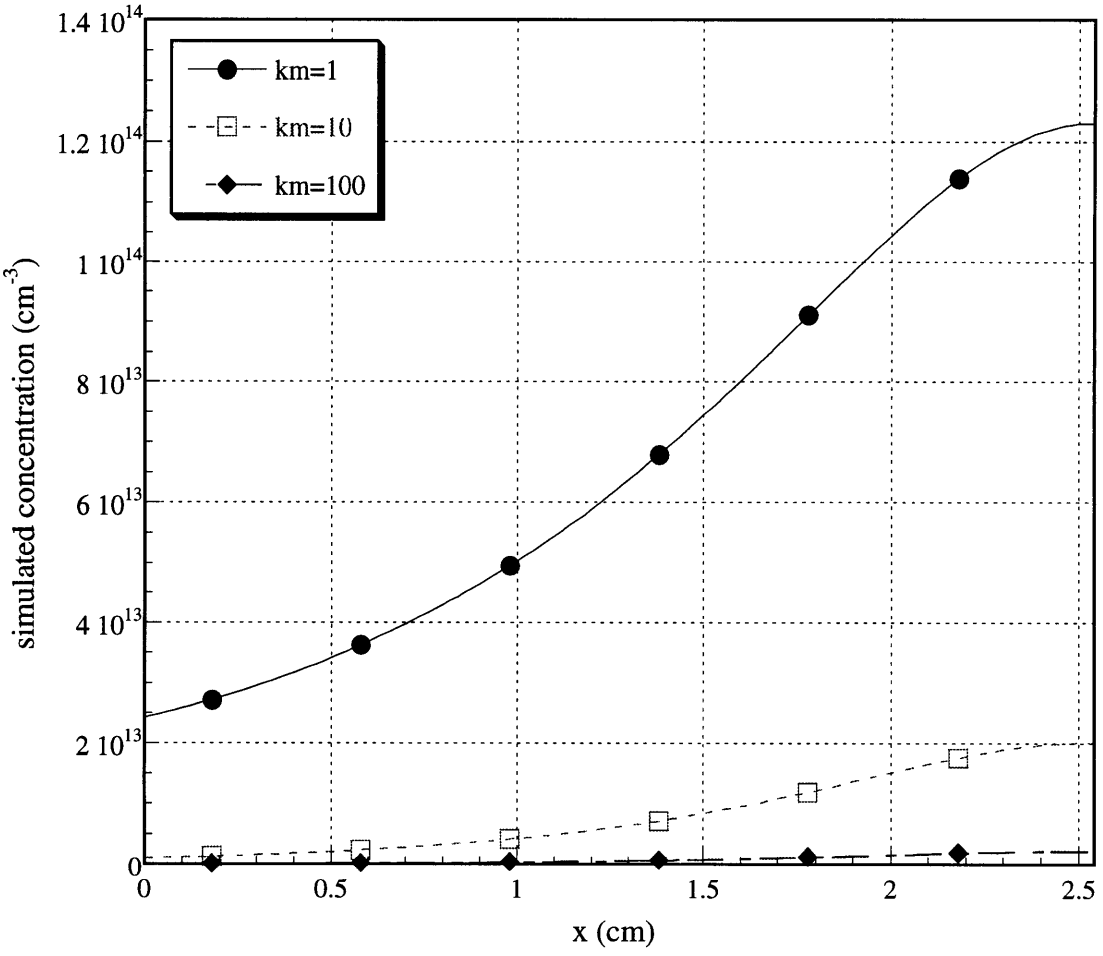

Figure 7-11: Baseline simulated C_s for k_m=1,10,100 cm^{-1}

This is shown in Figure 7-12, which redisplays the three curves from Fig. 7-11 after having each been normalized to their maximum concentrations. Also shown in Fig. 7-12 is the normalized growth rate data from Fig. 7-3. As you can see, the shape of the growth rate profile roughly matches that of the $k_m = 10$ cm^{-1} or $k_m = 100$ cm^{-1} simulation but definitely is not similar to the $k_m = 1$ cm^{-1} profile, implying that growth is in a transport limited regime and that the rate of reaction has an ever increasingly small effect on the growth rate distribution.

By changing the system pressure, we alter both the diffusion coefficient and the filament concentration. The self-diffusion coefficient from kinetic gas theory and the ideal gas law, D_{kin}, for spherical, non-interacting molecules can be expressed by

$$D_{kin} = \frac{2}{3}\left[\frac{k_b^3}{\pi^3 m}\right]^{\frac{1}{2}} \frac{T^{\frac{3}{2}}}{P d^2} \qquad (7\text{-}8)$$

where k_b = Boltzmann's constant
m = atomic mass
P = system pressure
T = gas temperature
d = molecular diameter

Note that $D_{kin} \propto \frac{1}{P}$ while $C_f \propto P$ from the ideal gas law. Therefore, the simulations of the $P = ½*P_{base}$ experiment were run with $k_m = ½*k_{m,base}$ and $C_f = ½*C_{f,base}$. The resulting concentration predictions were identical to the base case simulations with $C_f = C_{f,base}$ and $k_m = k_{m,base}$ for $k_m = 1$, 10, & 100 cm^{-1}.

Last of all, the half filament-to-substrate spacing experiments were modeled by running the simulation on a 3.54 cm x 0.49 cm rectangular grid with an asymmetric grid spacing of 0.02 cm in the x-direction and 0.01 cm in the shorter y-direction. The normalized near-surface concentration profiles for $k_m = 1$, 3, 5, 10, and 100 cm^{-1} are shown

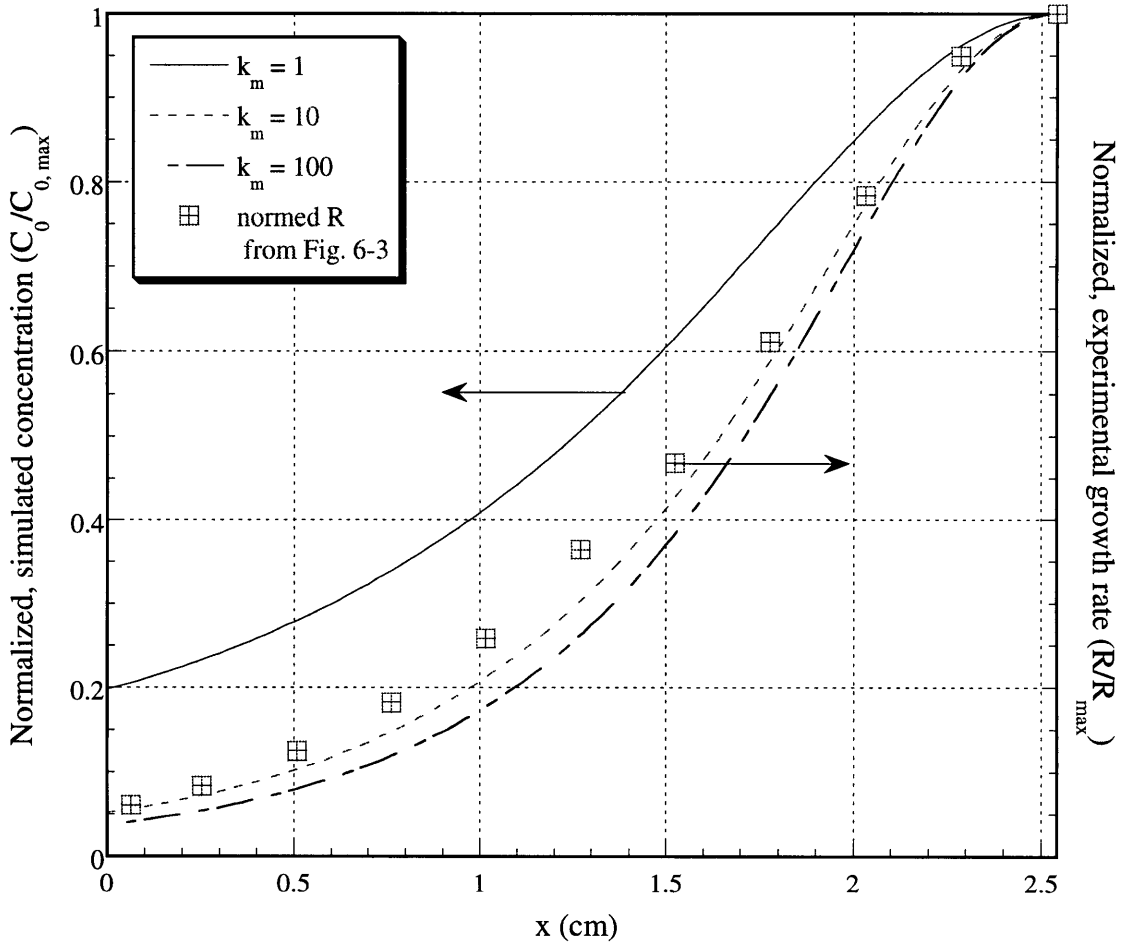

Figure 7-12: Normalized, simulated C_s for the baseline case and k_m=1,10,100 cm^{-1} and normalized growth rate from the trial case deposition (See Fig. 7-3)

in Figure 7-13, along with the normalized growth rate data from Fig. 7-6; k_m = 3 cm^{-1} would seem to give the best fit in this case.

However, based on the fit of the shape of the base case growth data to the simulation results shown in Fig. 7-12, we had previously estimated k_m to be about 10 cm^{-1}. Since k_m is the ratio of two parameters, k_s and D, which should not change with a change in the filament to substrate distance, a statistical approach to determine the best value for k_m is needed.

For a given k_m, the predicted gas phase concentration near the substrate surface is related to the growth rate by a proportionality constant, *p*, as a result of our first order reaction assumption; i.e.,

$$R = \frac{M_w}{\rho N_0} * (6x10^9 \frac{s\ Å}{min\ cm}) * flux$$

$$= \left\{\frac{M_w}{\rho N_0} * 6x10^9\right\} \left\{\left.\frac{\partial C_s}{\partial y}\right|_{y=0}\right\} = \left\{\frac{M_w}{\rho N_0} * 6x10^9\right\} k_s C_s = p C_s \qquad (7\text{-}9)$$

where R is the linear growth rate in units of Å/min
M_w is the molecular weight of the film in gm/mol
ρ is the density of the film in gm/cm^3
N_0 is Avogadro's number
p is the proportionality constant between R and C_s

By using *p* as an adjustable parameter, the best possible fit of the simulation results to both sets of experimental data together can be determined for a particular k_m. To quantify the fit, the chi-square statistic, χ^2, was calculated and minimized

$$\chi^2 = \sum_{i=1}^{N} \left[\frac{y_i - y(x_i; a_1, \ldots, a_M)}{\sigma_i}\right]^2 \qquad (7\text{-}10)$$

where x_i = independent variable (distance along wafer)
y_i = measured dependent variable (growth rate)

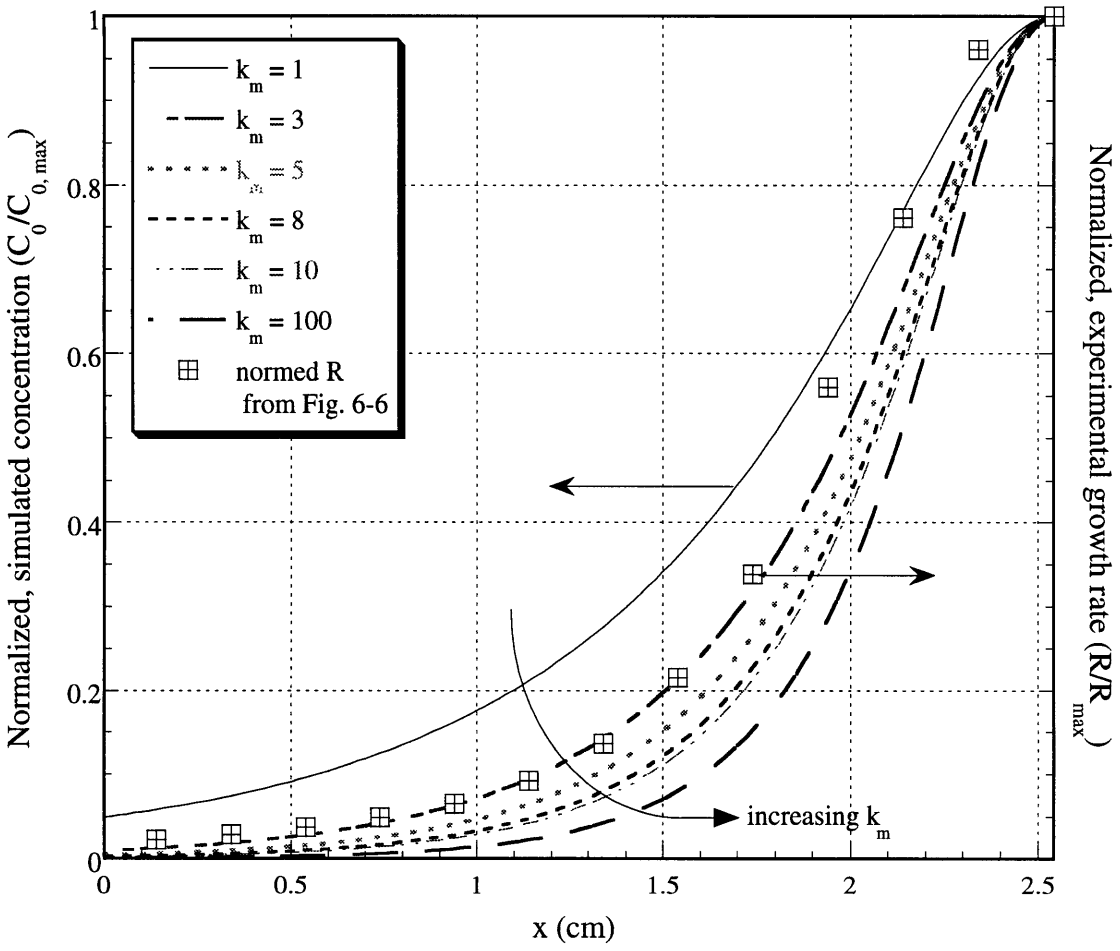

Figure 7-13: Normalized, simulated C_s for the ½d_{fs} case and k_m=1,10,100 cm^{-1} and normalized growth rate from the ½d_{fs} experiment (see Fig. 7-6)

$y(x_i)$ = predicted dependent variable
σ_i = standard deviation at each data point
a_j = adjustable parameters
N = number of data points
M = number of adjustable parameters

Since we have no measurement of the standard deviation of each data point, we first assigned an arbitrary σ for all points, minimized χ^2, and then recalculated σ

$$\sigma^2 = \sum_{i=1}^{N} \frac{(y_i - y(x_i))^2}{N-M} \tag{7-11}$$

This process was repeated until a final σ^2 and minimal χ^2 value were reached. Because this process resulted in a different σ^2 for each k_m, a uniform σ^2 was chosen from the average of all the final $\sigma^2(k_m)$'s. For the base case experiments, σ^2 was chosen to be 1800 $(Å/min)^2$ or σ = 42 Å/min which gave an estimated 2σ error of ±84 Å/min about each measurement which is reasonable. For the thicker film from the $½d_{fs}$ experiment, σ^2 was chosen to be 17000 $(Å/min)^2$ giving an estimated 2σ error of ±260 Å/min. Table 7-1 lists the minimum χ^2 and its corresponding value for *p* for k_m = 3, 5, 6, 7, 8, and 10 cm^{-1}. From the table, one can see that the smallest χ^2 value corresponds to the k_m = 6 cm^{-1} case. The quality of the fit to the base case and $½d_{fs}$ absolute growth rate data for k_m = 6 cm^{-1} can be seen in Figure 7-14. Furthermore, the quality of this fit can be statistically tested by calculating $Q(\chi^2|v)$ =

Table 7-1: Summary of χ^2 fits of simulated CVD PDMS deposition rates to values from the baseline and $½d_{fs}$ experiments

	$k_m = 3$	$k_m = 5$	$k_m = 6$	$k_m = 7$	$k_m = 8$	$k_m = 10$
p	2.48×10^{-11}	3.88×10^{-11}	4.56×10^{-11}	5.25×10^{-11}	5.93×10^{-11}	7.28×10^{-11}
χ^2	39.137	18.421	17.979	19.442	21.714	26.934

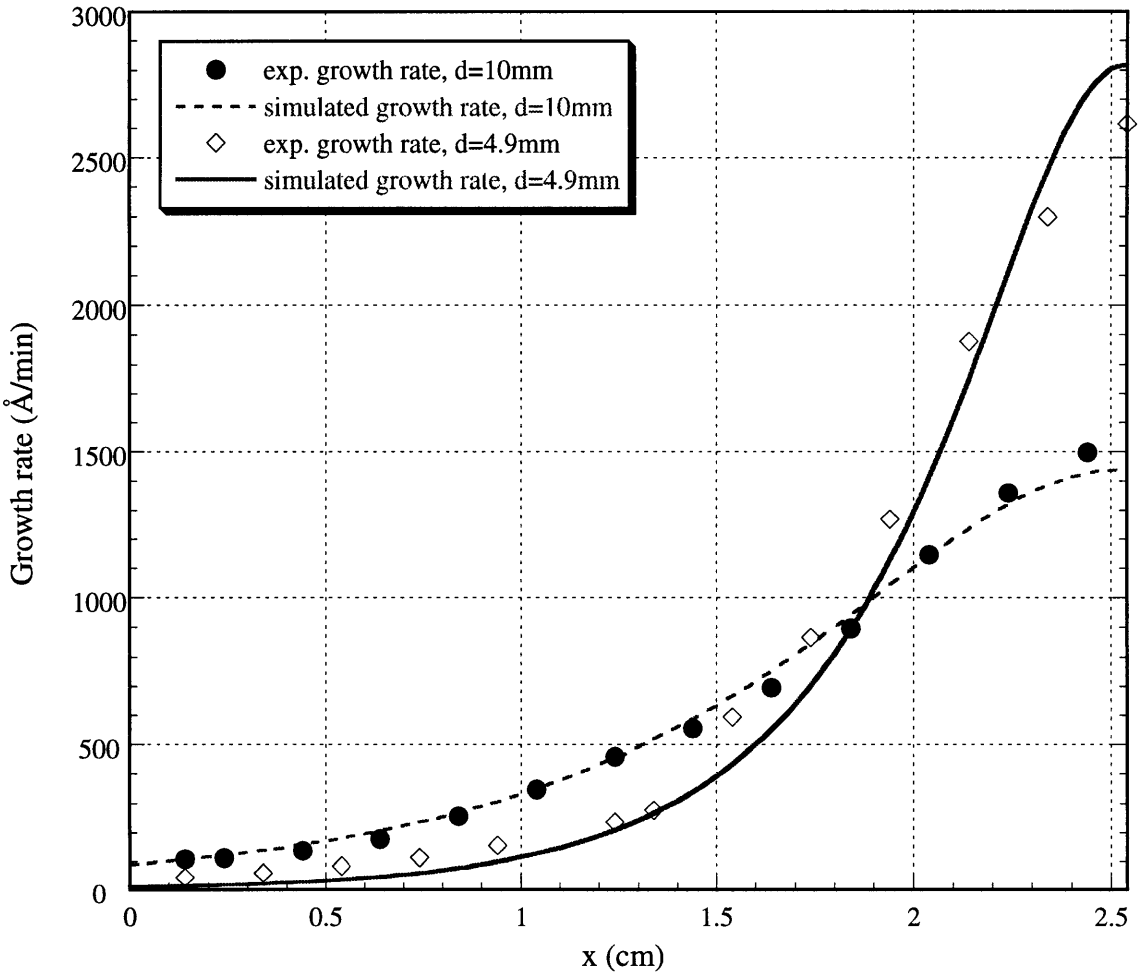

Figure 7-14: Comparison of simulated growth rate to experimentally measured deposition rate for $k_m = 6\ cm^{-1}$

$\Gamma_i\left(\frac{\nu}{2}, \frac{\chi^2}{2}\right)$ where Γ_i is the incomplete gamma function. Q is the probability that the chi-square statistic will exceed a particular value χ^2 by chance. For $\chi^2 = 17.98$ and $\nu = 24$, Q = 0.804 which means that there is an 80% probability that any differences between the data and the model are due to chance and not because the model is incorrect.[3] Like any hypothesis testing, this analysis does not prove that the model is right but rather shows that it is not likely to be wrong.

7.3 Discussion

7.3.1 Effect of pressure

One of the most notable effects of changing the reactor pressure was that there was no effect. The experimental measurements in Fig. 7-5 showed that halving the pressure did not affect the growth rate. The finite difference simulations produced the same results. One way to understand this lack of response is to study the analogous one dimensional problem. From the derivation in section 5.1,

$$r = \frac{k_s D C_0}{L k_s + D} = \frac{k_s C_0}{Da + 1} \qquad (7\text{-}12)$$

where $Da = \frac{L ks}{D}$ = Damköhler number

For Da<<1, $r \sim k_s C_0$, which is $\propto$ P while for Da>>1, $r \sim \frac{D C_0}{L}$, which is roughly P invariant. Looking back at our 2D case and using the filament-to-substrate distance of 1 cm as the characteristic length, Da = (1 cm)*k_m = 6 which would imply that R is in the pressure invariant growth regime. In order to test this hypothesis, deposition rate experiments can be done at lower pressure (<100 mtorr) or smaller d_{fs} (<0.1cm), but the first experiment

would suffer from considerably lower growth rates while the second one would be difficult to do experimentally because of the increased heat load to the wafer and the larger percentage variability in d_{fs}.

7.3.2 Interpretation of fitted k_m

From Eqn. 7-9, *p*, the fitting parameter involved in determining that $k_m = 6\ cm^{-1}$ gives the best fit to the experimental data, is also proportional to k_s. Furthermore, since that proportionality just involves constants related to the growing film which convert the rate of flux to a film deposition rate, k_s and D can be calculated; i.e.,

$$k_s = \frac{p}{\left\{\frac{M_w}{\rho N_0} * 6x10^9\right\}} \tag{7-14}$$

$$D = \frac{k_s}{k_m} \tag{7-15}$$

For example, assuming a film density of 0.975 gm/cm^3, a molecular weight for the activated species of 267 gm/mol (D_4 minus 2 CH_3's), and $k_m = 6\ cm^{-1}$, Eqn. 7-14 and 7-15 would give $k_s = 17$ cm/s and $D = 2.8\ cm^2/s$. Because C_s, the concentration near the surface, is a function of C_f, the active species concentration at the filament, which we have assumed up to this point to be $8x10^{14}\ cm^{-3}$ for the base case, k_s and D will also be functions of C_f. Baseline simulations for various values of k_m in which C_f was varied from $C_{f,0}$ to $2*C_{f,0}$ to $½*C_{f,0}$ show that the model results scale directly with C_f which implies that k_m is invariant with respect to C_f and that k_s and D are inversely proportional to C_f.

In order to narrow down the degree of gas phase activation, a plot of the estimated diffusion coefficient from the model versus the percentage of precursors in the gas phase was generated in Figure 7-15 using the fact that D*(10% dissociation) = 27.9. For

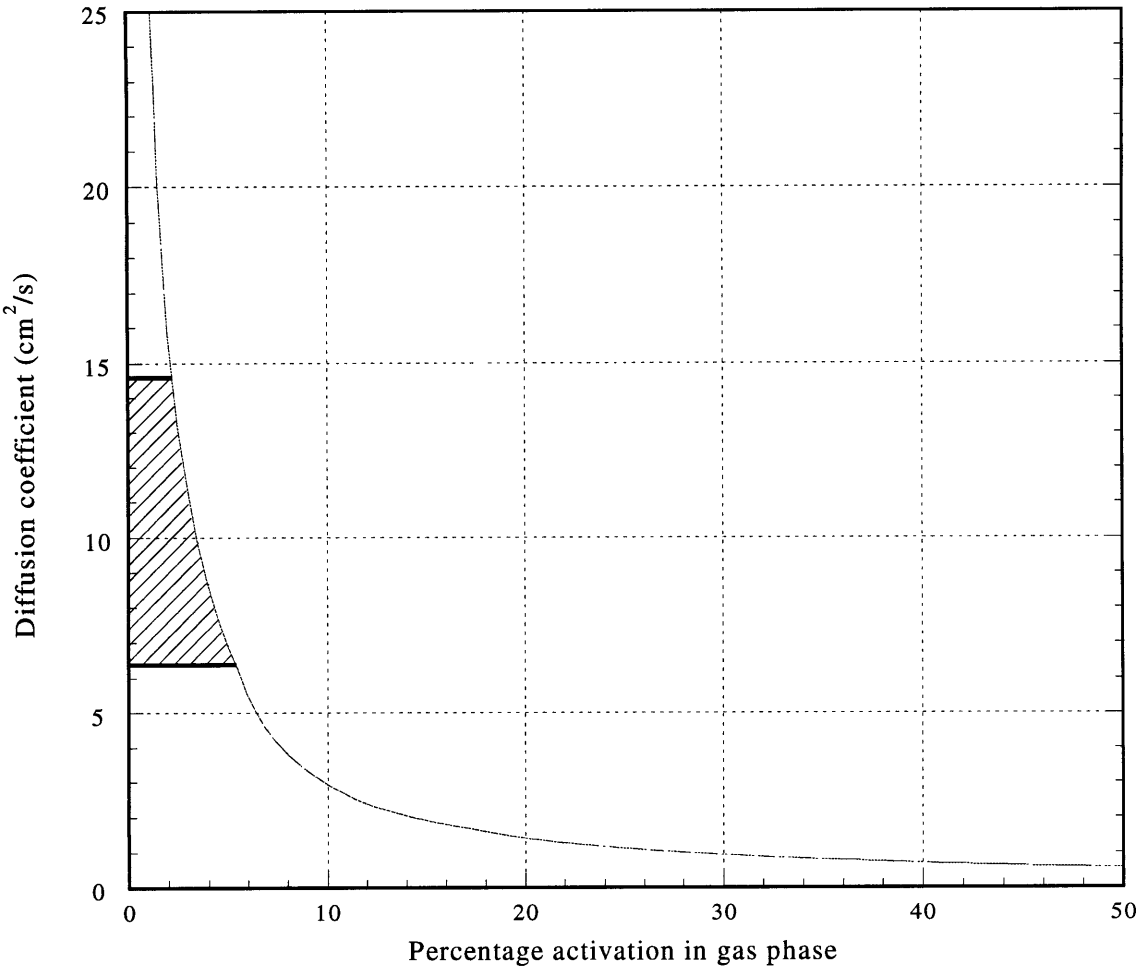

Figure 7-15: Effect of degree of gas phase activation on estimated diffusion coefficient from finite difference PDMS growth model

Hatched area is the range of diffusion coefficients from kinetic gas theory.

comparison, the self-diffusion coefficient from kinetic gas theory for hard, non-interacting spheres at low density (see Eqn 7-8) was also calculated for a range of molecular diameters (8.8 - 12.2 Å) and gas temperatures (150 - 200 °C). For example, if we assume an average gas temperature of 200 °C and a molecular diameter of 8.8 Å, then D_{kin} is 15 cm^2/s for our de-methylated D_4 molecule. The range of D_{kin} suggests that the degree of activation is low, in the range of 2-5%.

Within that range of 2-5% activation, k_s ranges from 33-84 cm/s. The sticking coefficient, γ, can be calculated from the following definition:

$$\gamma = \frac{k_s C_s}{\text{(flux from kinetic gas theory)}} = k_s \sqrt{\frac{2 \pi M_w}{R T}} \qquad (7\text{-}16)$$

For M_w = 267 gm/mol and T = 150 °C, $\gamma = (2.2 \times 10^{-4}\ s/cm) * k_s$ or γ = 0.007 - 0.02 for the range of k_s assuming that a de-methylated D_4 molecule is the growth limiting precursor. These values are reasonable and within the 10^{-2} to 10^{-5} range typical for CVD systems; e.g. the sticking coefficient for CF_2 addition onto a fluorocarbon surface in a pulsed plasma deposition system has been estimated to be in the 10^{-3} range.[4]

However, a unique solution for k_s and D and hence a definitive assignment of the most likely precursor is not possible from this analysis because there are basically three linear equations; i.e.,

$$C_s \propto C_f$$

$$k_s = 6\ D$$

$$R \propto k_s C_s$$

in four unknowns; i.e., C_s, C_f, k_s, and D. The best that we can do without additional information is conclude that the degree of activation in the gas phase is relatively low and probably less than 5% since growth precursors smaller than D_4 would necessitate smaller

dissociation fractions but greater than 1% since it is unlikely to have a precursor smaller than D_1. In a similar vein, the sticking coefficient for the growth precursor is calculated to be in the range from 0.007 to 0.09.

In conclusion, we have successfully modeled the variation in growth rate across a 2" substrate for a new pyrolytic CVD process for the deposition of thin, solid films of polydimethylsiloxane. The effect of a change in pressure and filament-to-substrate distance was modeled with a relatively simple generation / diffusion / surface reaction model with a Damköhler number of 6. Halving the pressure was shown experimentally and in the simulation to have no effect on the growth rate. Halving the filament-to-substrate distance had a significant effect, almost doubling the linear film growth rate in the center of the wafer. An analysis of the parameters from the model suggests that the mole fraction of growth precursors near the filament is low, 0.01 - 0.05, and that the sticking coefficient for the activated species is from 0.007 to 0.09.

List of variables:

ϕ	angle of incidence of light in ellipsometry measurement	rad
λ	wavelength of light for ellipsometry	Å
Ψ	measured ellipsometer parameter	rad
Δ	measured ellipsometer parameter	—
ρ	film density	gm cm^{-3}
C	gas phase concentration	cm^{-3}
C_f	gas phase concentration of activated species at filament	cm^{-3}
C_s	gas phase concentration of growth precursor at surface	cm^{-3}
d	film thickness	Å
d_{fs}	filament to substrate distance	cm
D	diffusion coefficient	$cm^2\ s^{-1}$
Da	Damköhler number, $k_s d_{fs}/D$	—
k_m	ratio of k_s/D	cm^{-1}
k_s	1^{st} order rate coefficient for surface growth reaction	cm s^{-1}
M_w	molecular weight	gm mol^{-1}
n_0	index of refraction of surround medium for ellipsometry	—
n_f	index of refraction of film for ellipsometry	—
n_m	index of refraction of reflecting substrate for ellipsometry	—
N_0	Avogadro's number	mol^{-1}
p	proportionality between gas phase concentration near surface and linear growth rate	Å cm^3 min^{-1}
P	pressure	torr
R	linear growth rate	Å min^{-1}
t_{cycle}	cycle thickness used in ellipsometry	Å
T	temperature	K
x	coordinate parallel to wafer surface	—
y	coordinate perpendicular to wafer surface	—

References:

1. R. H. Muller, *Optical Techniques in Electrochemistry*; **vol. 9**, ed. by R. H. Muller. John Wiley & Sons: New York. 1973. pp 167-226.
2. S. Wasserman, 1996 (Personal communication through Cathy Labelle).
3. W. H. Press, S. A. Teukolsky, W. T. Vetterling, and B. P. Flannery, *Numerical Recipes in FORTRAN*; 2nd ed. Cambridge University Press: Cambridge. 1992.
4. S. J. Limb, Ph. D. Thesis, Massachusetts Institute of Technology, 1997.

8. APPENDIX A

8.1 3D finite difference Matlab simulation batch file: *working.m*

```
% An M-file to construct an x*y*z x x*y*z element sparce band diagonal
% A-matrix for use in finite difference problem.  Also sets up related
% b-matrix.  Solving Laplace's equation in 3D on a x-y-z grid with
%     no-flux BC in x-directions and positive z-direction,
%      (mirror planes for +x & +z and extend to infinity for -x)
%     zero concentration BC in negative z-direction,
%     BC at y=y(max) is constant concentration at filament or no flux
%           otherwise,
%        at y=0 is C' = k*C(y=0) w/ k = f(x,z).
%
% h1=x-dir grid size[=]cm; h2=y-dir grid size[=]cm; h3=z-dir grid size[=]cm;
% km[=]cm^-1; conc[=]cm^-3;
%
%    y,2
%     |
%     |      z,3
%     |     /
%     |   /
%     |/___________ x,1
%
x = 45;
y = 6;
z = 12;
xy = x*y;
xyz = x*y*z;
h1 = 2.25/x;
h2 = .3/y;
h3 = 0.6/z;
theta1 = h2*h3/h1;
theta2 = h1*h3/h2;
theta3 = h1*h2/h3;
km = 9;
conc = 3e15;

%     Create square sub-matrices:
I1 = eye(y)*theta1;
I3 = eye(xy)*theta3;
I3 = sparse(I3);

% By default, no-flux in y-direction unless modified as below
A = zeros(y);
AA = zeros(y);
A(1,1:2) = [-2*(theta1+theta2+theta3) 2*theta2];
AA(1,1:2) = [-2*(theta1/2+theta2+theta3) 2*theta2];
A(y,(y-1):y) = [2*theta2 -2*(theta1+theta2+theta3)];
AA(y,(y-1):y) = [2*theta2 -2*(theta1/2+theta2+theta3)];
T = [theta2 -2*(theta1+theta2+theta3) theta2];
TT = [theta2 -2*(theta1/2+theta2+theta3) theta2];
for i=2:(y-1)
A(i,i-1:i+1) = T;
AA(i,i-1:i+1) = TT;
end
```

```
% For simple case (y=3), can simplify but won't -
% A(2,1:3) = [theta2 -2*(theta1+theta2+theta3) theta2];
% Uniform "gray" test surface:
% F = ones(z,x)*(-2*(theta1+theta2*(1+h2*km)+theta3));
%  or customized:
load F.txt

T = [I1 A I1];
%     Create matrix of zeros:
amatrix = spalloc(xyz,xyz,7*xyz);
    % Fill in matrix:
for i=0:(z-1)
    % Set x-direction no-flux BC's and y-direction component for x(min) &
    %  x(max), using 2-sided difference conditions for neg.x-direction and ...
      amatrix(xy*i+1:xy*i+y,xy*i+1:xy*i+2*y) = [A 2*I1];
    %   single-sided difference conditions for pos.x-direction.
      amatrix(xy*(i+1)-y+1:xy*(i+1),xy*(i+1)-2*y+1:xy*(i+1)) = [I1 AA];
    %   2-sided difference conditions for pos.x-direction.
    % amatrix(xy*(i+1)-y+1:xy*(i+1),xy*(i+1)-2*y+1:xy*(i+1)) = [2*I1 A];
    % z-direction component -
      if (i>0)&(i<(z-1))
      amatrix(xy*i+1:xy*(i+1),xy*(i-1)+1:xy*i) = I3;
      amatrix(xy*i+1:xy*(i+1),xy*(i+1)+1:xy*(i+2)) = I3;
      end
    % x-direction and y-direction components -
      for j=1:(x-2)
      amatrix(xy*i+y*j+1:xy*i+y*(j+1),xy*i+y*(j-1)+1:xy*i+y*(j-1)+3*y) = T;
      end
    % Set correct reactivity at surface (specify entire x-z surface) -
      for j=0:(x-1)
      amatrix(xy*i+y*j+1,xy*i+y*j+1) = -
2*((F(i+1,j+1)*km*h2+1)*theta2+theta1+theta3);
      end
end

% --------
%     Correct for filament (i.e., constant conc instead of no-flux):
for j=1:x
amatrix(xyz-xy+y*j,xy*(z-1)-1+y*j) = theta2;
end

%     Set no-flux BC in z-directions using 2-sided difference:
% amatrix(1:xy,(xy+1):2*xy) = I3*2;
% amatrix((xyz-xy+1):xyz,(xyz-2*xy+1):(xyz-xy)) = I3*2;

%     Set zero conc BC in neg.z-direction (C @ (-1)grid point):
amatrix(1:xy,xy+1:2*xy) = I3;

%     Set no-flux BC in pos.z-direction using single sided difference, ...
amatrix(xyz-xy+1:xyz,xyz-2*xy+1:xyz-xy) = I3;
for  i=1:xy
amatrix(xyz-xy+i,xyz-xy+i) = -2*(theta1+theta2+theta3/2);
end
%     ...fix correct surface reactivity (in z-dir...
for i=0:(x-1)
amatrix(xyz-xy+y*i+1,xyz-xy+y*i+1) =
      -2*((F(z,i+1)*km*h2+1)*theta2+theta1+theta3/2);
end
%     ...& x-dir), ...
for i=1:z
```

```
amatrix(xy*i-y+1,xy*i-y+1) = -2*((F(i,x)*km*h2+1)*theta2+theta1/2+theta3);
end
%     ... and fix last y-dir column to have correct z & x-dir BC:
amatrix(xyz-y+1,xyz-y+1) = -2*((F(z,x)*km*h2+1)*theta2+theta1/2+theta3/2);
for i=2:y
amatrix(xyz-y+i,xyz-y+i) = -2*(theta1/2+theta2+theta3/2);
end

% --------
%     Create constant matrix::
bmatrix = spalloc(xyz,1,x);
%     ... and put constant conc filament top edge of back xy plane:
for i=1:x
bmatrix(xyz-xy+y*i,1) = -theta2*conc;
end
%
% Clean up after myself...
clear T TT i j A AA I1 I3 F x y z xy xyz h1 h2 h3 theta1 theta2 theta3 conc km
```

8.2 Example of text file describing surface reactivity: *F.txt*

```
1 1 1 
```

9. APPENDIX B

```
(*^
::[   Information =

"This is a Mathematica Notebook file.  It contains ASCII text, and can be
transferred by email, ftp, or other text-file transfer utility.  It should be
read or edited using a copy of Mathematica or MathReader.  If you received
this as email, use your mail application or copy/paste to save everything from
the line containing (*^ down to the line containing ^*) into a plain text
file.  On some systems you may have to give the file a name ending with ".ma"
to allow Mathematica to recognize it as a Notebook.  The line below identifies
what version of Mathematica created this file, but it can be opened using any
other version as well.";

      FrontEndVersion = "Macintosh Mathematica Notebook Front End Version
2.2";

      MacintoshStandardFontEncoding;

      paletteColors = 128; currentKernel;
]

:[font = title; inactive; preserveAspect]
Ellipsometry

:[font = subtitle; inactive; preserveAspect; fontColorBlue = 65535]
Version 1

:[font = section; inactive; preserveAspect]
Original copyright ) 1996 by Stephen R. Wasserman
Sections modified by Michael Kwan, 1997

:[font = special1; inactive; preserveAspect]
This package contains basic routines for ellipsometry analysis

:[font = section; inactive; preserveAspect]
Begin Package

:[font = input; initialization; preserveAspect]
*)
BeginPackage["Ellipsometry`"]
(*

:[font = section; inactive; preserveAspect; fontColorRed = 65535]
Package User Definitions

:[font = subsection; inactive; Cclosed; preserveAspect; fontColorBlue = 65535;
start@roup]
Functions

:[font = input; initialization; preserveAspect; endGroup]
*)

snell::usage =
"snell[n2,phi1,n1] gives the angle of refraction, phi2, from
Snell's law.  The input values are the refractive indices of
the media, and the angle of incidence for light entering from
```

```
medium 1.  The returned value, phi2, is in radians.";

pFresnel::usage =
"pFresnel[n1,n2,n0,phi0] gives the Fresnel reflection
coefficient for the p polarization.  The routine is designed
to give a reflection coefficient for an arbitrary interface,
given the refractive indices of the two media, n1 and n2,
and the angle of incidence, phi0, in a reference medium with
refractive index n0.";

sFresnel::usage =
"sFresnel[n1,n2,n0,phi0] gives the Fresnel reflection
coefficient for the s polarization.  The routine is designed
to give a reflection coefficient for an arbitrary interface,
given the refractive indices of the two media, n1 and n2,
and the angle of incidence, phi0, in a reference medium with
refractive index n0.";

nSubstrate::usage =
"nSubstrate[phi0,n0] finds the refractive index of a bare
substrate.  Values for the analyzer and polarizer angles are
input by the user.";

dl::usage =
"dl is the command to solve for the length of the two films
in a double layer system.  It calls doubleLayer.";

doubleLayer::usage =
"doubleLayer[n0,n1,n2,n3,phi0,lambda] finds the two thicknesses
from a double film system.";

sl::usage =
"sl is the command to solve for the length of a film
in a single layer system.  It calls singleLayer.";

singleLayer::usage =
"singleLayer[n0,n1,n2,phi0,lambda] finds the length, d, of a
thin film from the analyzer and polarizer readings.";

singleLayerQuadratic::usage =
"singleLayerQuadratic[n0,n1,n2,phi0,lambda] finds the two routes
for a single layer thin film.  It is an alternative
equivalent of singleLayer; they solve the same equation.
Unlike singleLayer, quadraticSolve returns the two lengths
which solve the quadratic equation from the single layer
problem.  The solution will be 2 complex numbers.  According
to Muller, the one with the smaller imaginary component
is typically used.";


phaseAngle::usage =
"phaseAngle[d,lambda,n,n0,phi0] gives the phase angle
for a given film thickness.  Normally, d is left as a
variable, while values are provided for the other
parameters of this function.";


getRho::usage =
"getRho determines the value of rho from the analyzer and
polarizer angles.";
```

```
(*

:[font = subsection; inactive; Cclosed; preserveAspect; fontColorRed = 65535;
startGroup]
Variables

:[font = input; initialization; preserveAspect; endGroup]
*)

lambda::usage =
"lambda is the wavelength in angstoms of the light used for
the ellipsometry measurements.";

n0::usage =
"n0 is the refractive index of the ambient medium.  Typically,
the ambient is air, and n0=1";

n1::usage =
"n1 is the refractive index of the topmost layer, which
is the film closest to air.";

n2::usage =
"n2 is the refractive index of the second layer from the
top of the sample.  In a single layer system, it is the
refractive index of the substrate.";

n3::usage =
"n3 is the refractive index of the third layer from the
top of the sample.  In a double layer system, it is the
refracthve index of the substrate.";

phi0::usage =
"phi0 is the angle of incidence from the ambient
medium (usually air, n0=1)";
(*

:[font = section; inactive; preserveAspect; startGroup]
Begin Private

:[font = input; initialization; preserveAspect; endGroup]
*)
Begin["`Private`"];
(*

:[font = section; inactive; initialization; Cclosed; preserveAspect;
fontColorRed = 65535; startGroup]
Error Handling

:[font = input; initialization; dontPreserveAspect; endGroup]
*)

(* Turn off messages about possible spelling errors. *)

Off[General::spell1]

(*

:[font = section; inactive; preserveAspect; fontColorRed = 65535; startGroup]
General Parameters

:[font = input; initialization; preserveAspect; endGroup]
```

```
*)
phi0=70;

lambda=6328;            (* HeNe red laser *)

radConvert=N[Pi]/180;

(*

:[font = section; inactive; preserveAspect; fontColorRed = 65535; startGroup]
Refractive Indices

:[font = input; initialization; preserveAspect; endGroup]
*)
n0=1;                   (* Ambient-air *)

n1=1.4;                 (* First layer - PDMS *)

(* n2=1.460;            (* Second layer- Silicon Dioxide *) *)

n2=3.858-0.018*I; (* Substrate - Silicon *)
(*

:[font = section; inactive; Cclosed; preserveAspect; fontColorBlue = 65535;
startGroup]
Snell's Law

:[font = input; initialization; preserveAspect; endGroup]
*)
snell[n2_,phi1_,n1_] := Module[

      {radConvert,sinphi2,phi2},

      radConvert=N[Pi]/180;

      sinphi2=n1/n2*Sin[phi1*radConvert];

      phi2=ArcSin[sinphi2]/radConvert;

                        (* Return phi2 in degrees *)

      Return[phi2]

      ] (* End of Module snell *)
(*

:[font = section; inactive; Cclosed; preserveAspect; fontColorRed = 65535;
startGroup]
Fresnel Reflection Coefficients

:[font = input; initialization; preserveAspect]
*)
pFresnel[n1_,n2_,n0_,phi0_] :=

      Module[{radConvert,phi1,phi2,cosphi1,cosphi2,rp},

            radConvert=N[Pi]/180;

            phi1=snell[n1,phi0,n0];

            phi2=snell[n2,phi0,n0];
```

```
            cosphi1=Cos[phi1*radConvert];

            cosphi2=Cos[phi2*radConvert];

            rp=(n2*cosphi1-n1*cosphi2)/
                  (n2*cosphi1+n1*cosphi2);

            (*
                  Alternative Form

                  rp=Tan[(phi1-phi2)*radConvert]/
                        Tan[(phi1+phi2)*radConvert]

            *)

            Return[rp]

            ] (* End of Module pFresnel *)
(*

:[font = input; initialization; preserveAspect; endGroup]
*)
sFresnel[n1_,n2_,n0_,phi0_] :=

      Module[{radConvert,phi1,phi2,cosphi1,cosphi2,rs},

            radConvert=N[Pi]/180;

            phi1=snell[n1,phi0,n0];

            phi2=snell[n2,phi0,n0];

            cosphi1=Cos[phi1*radConvert];

            cosphi2=Cos[phi2*radConvert];

            rs=(n1*cosphi1-n2*cosphi2)/
                  (n1*cosphi1+n2*cosphi2);

            (*
                  Alternative Form

                        rs=-Sin[(phi1-phi2)*radConvert]/
                        Sin[(phi1+phi2)*radConvert]

            *)

            Return[rs]

            ] (* End of Module sFresnel *)
(*

:[font = section; inactive; Cclosed; preserveAspect; fontColorBlue = 65535;
startGroup]
Refractive Index of Bare Substrate

:[font = input; initialization; preserveAspect; endGroup]
*)
nSubstrate[phi0_,n0_] :=
```

```
      Module[

            {radConvert,rhoSubstrate,n},

            radConvert=N[Pi]/180;

            rhoSubstrate=getRho;  (* getRho returns the value for
                                          rho. *)


            n=n0*Tan[phi0*radConvert]*
                  Sqrt[1-4*rhoSubstrate*
                        Sin[phi0*radConvert]^2/
                  (rhoSubstrate+1)^2];

            Return[n];

            ] (* End of Module nSubstrate *)
(*

:[font = section; inactive; Cclosed; preserveAspect; startGroup]
Double Layer

:[font = input; initialization; preserveAspect]
*)
dl := doubleLayer[n0,n1,n2,n3,phi0,lambda];
(*

:[font = input; initialization; preserveAspect; endGroup]
*)
doubleLayer[n0_,n1_,n2_,n3_,phi0_,lambda_] :=

      Module[

            {d1Real,d1Imag,
                  d2Real,d2Imag,
                  beta1,beta2,
                  r01p,r12p,r23p,
                  r01s,r12s,r23s,
                  RpNumerator,RpDenominator,Rp,
                  RsNumerator,RsDenominator,Rs,
                  rhoTheory,rhoExpt},


            (* Separate distances into real and
                  imaginary parts. *)

            beta1=phaseAngle[d1Real+d1Imag*I,lambda,n1,n0,phi0];

            beta2=phaseAngle[d2Real+d2Imag*I,lambda,n2,n0,phi0];


            r01p=pFresnel[n0,n1,n0,phi0];

            r12p=pFresnel[n1,n2,n0,phi0];

            r23p=pFresnel[n2,n3,n0,phi0];


            r01s=sFresnel[n0,n1,n0,phi0];
```

```
            r12s=sFresnel[n1,n2,n0,phi0];

            r23s=sFresnel[n2,n3,n0,phi0];


            RpNumerator=r01p+r12p*Exp[-I*2*beta1]+
                  (r01p*r12p+Exp[-I*2*beta1])*r23p*Exp[-I*2*beta2];

            RpDenominator=(1+r01p*r12p*Exp[-I*2*beta1])+
                  (r12p+r01p*Exp[-I*2*beta1])*r23p*Exp[-I*2*beta2];

            Rp=RpNumerator/RpDenominator;



            RsNumerator=r01s+r12s*Exp[-I*2*beta1]+
                  (r01s*r12s+Exp[-I*2*beta1])*r23s*Exp[-I*2*beta2];

            RsDenominator=(1+r01s*r12s*Exp[-I*2*beta1])+
                  (r12s+r01s*Exp[-I*2*beta1])*r23s*Exp[-I*2*beta2];

            Rs=RsNumerator/RsDenominator;



            rhoTheory=Rp/Rs;

            rhoExpt=getRho;


            FindMinimum[Abs[rhoTheory - rhoExpt],

                  {d1Real,700,1500},{d1Imag,0,1},
                  {d2Real,0,105},{d2Imag,0,1}

                  ]

            ] (* End of Module doubleLayer *)
(*

:[font = section; inactive; Cclosed; preserveAspect; fontColorRed = 65535;
startGroup]
Single Layers

:[font = input; initialization; preserveAspect]
*)
sl := singleLayer[n0,n1,n2,phi0,lambda];
(*

:[font = input; initialization; preserveAspect]
*)
singleLayer[n0_,n1_,n2_,phi0_,lambda_] :=

      Module[

            {r01p,r12p,r01s,r12s,beta,Rp,Rs,
                  rhoTheory,rhoExpt},

            r01p=pFresnel[n0,n1,n0,phi0];

            r12p=pFresnel[n1,n2,n0,phi0];
```

```
            r01s=sFresnel[n0,n1,n0,phi0];

            r12s=sFresnel[n1,n2,n0,phi0];


            (* See Azzam and Bashara, p. 284, for phase angle. *)

            beta=phaseAngle[d,lambda,n1,n0,phi0];



            (* Azzam and Bashara, p. 285 *)

            Rp=(r01p+r12p*Exp[-I*2*beta])/
                  (1+r01p*r12p*Exp[-I*2*beta]);

            Rs=(r01s+r12s*Exp[-I*2*beta])/
                  (1+r01s*r12s*Exp[-I*2*beta]);

            rhoTheory=Rp/Rs;
            rhoExpt=getRho;

            (* A negative thickness solution can be fixed by reversing
                  the search start and end values. *)

            d1=Input["Thickness search start value: "];
            d2=Input["Thickness search end value: "];

            (* Use rule in following statement to get both real
                  and imaginary parts of distance. *)

            FindMinimum[Abs[rhoTheory - rhoExpt] /. d-> dReal+ I*dImag,
                        {dReal,d1,d2},{dImag,0,1} ]


            ] (* End of Module singleLayer *)



(*

:[font = input; initialization; preserveAspect; endGroup]
*)
singleLayerQuadratic[n0_,n1_,n2_,phi0_,lambda_] :=

      Module[

            {radConvert,
                  r01p,r12p,r01s,r12s,
                  rhoMono,
                  a,b,c,
                  root1,root2,
                  length1,length2},


            radConvert=N[Pi]/180;

            r01p=pFresnel[n0,n1,n0,phi0];

            r12p=pFresnel[n1,n2,n0,phi0];
```

```
            r01s=sFresnel[n0,n1,n0,phi0];

            r12s=sFresnel[n1,n2,n0,phi0];

            phi1=snell[n1,phi0,n0];


            rhoMono=getRho;


            a=r12p*r01s*r12s-rhoMono*r12s*r01p*r12p;

            b=r12p+r01p*r01s*r12s-rhoMono*r12s-
                                    rhoMono*r01s*r01p*r12p;

            c=r01p-rhoMono*r01s;


            root1=(-b+Sqrt[b^2-4*a*c])/(2*a);

            root2=(-b-Sqrt[b^2-4*a*c])/(2*a);


            length1=Log[root1]*lambda/
                  (4*N[Pi]*(-I)*n1*Cos[phi1*radConvert]);

            length2=Log[root2]*lambda/
                  (4*N[Pi]*(-I)*n1*Cos[phi1*radConvert]);


            Return[{length1,length2}]


      ] (* End of Module quadratic Solve *)
(*

:[font = section; inactive; Cclosed; preserveAspect; fontColorBlue = 65535;
startGroup]
Phase Angle

:[font = input; initialization; preserveAspect; endGroup]
*)
phaseAngle[d_,lambda_,n_,n0_,phi0_] :=

      Module[{radConvert,phi,beta},

            radConvert=N[Pi]/180;

            phi=snell[n,phi0,n0];

            beta=2*N[Pi]*d*n*Cos[radConvert*phi]/lambda;

            (*

                  Alternate Form

                  beta1=2*N[Pi]*d*
                        Sqrt[n^2-n0^2*Sin[phi0*radConvert]^2]/
                                                      lambda
```

```
            *)

            Return[beta]


            ] (* End of Module phaseAngle *)
(*

:[font = section; inactive; Cclosed; preserveAspect; fontColorRed = 65535;
startGroup]
Determine r
;[s]
2:0,0;10,1;12,-1;
2:1,18,14,Chicago,1,14,65535,0,0;1,16,12,Symbol,1,14,65535,0,0;

:[font = input; initialization; preserveAspect; endGroup]
*)
getRho := Module[

            {radConvert,
                  analyzer,polarizer,delta,psi,rho},

            radConvert=N[Pi]/180;
(*
            analyzer=Input["Analyzer angle in degrees"];

            polarizer=Input["Polarizer angle in degrees"];

            delta=N[Pi]/2+2*radConvert*polarizer;

            psi=analyzer*radConvert;
*)
            psi=Input["Input psi in degrees: "]*radConvert;

            delta=Input["Input delta in degrees: "]*radConvert;

            rho=Tan[psi]*Exp[I*delta];

            Return[rho]

            ] (* End of module getRho *)
(*

:[font = section; inactive; preserveAspect; fontColorRed = 65535;
fontColorBlue
= 65535; startGroup]
End Package Ellipsometry

:[font = input; initialization; preserveAspect]
*)
End[]

(*

:[font = input; initialization; preserveAspect; endGroup]
*)
EndPackage[]
(*

^*)
```

10. APPENDIX C

```
% An M-file to construct an x*y by x*y element sparce band diagonal A-matrix
% for use in finite difference problem.  Also sets up related b-matrix.
% Solving Laplace's equation in 2D with
%     no-flux BC in x-direction,
%      (extends to infinity at -x and mirror plane at +x)
%     BC at y=y(max) is const. conc. for select elements & no-flux otherwise,
%        at z=0 is C' = k*C(z=0) w/ k = f(x).
%
% hx=x-dir grid size[=]cm; hy=y-dir grid size[=]cm; km[=]cm^-1; conc[=]cm^-3;
%
%     matrix element ordering in xy-plane:
%
%       5   10  15            50
%       4   9   14  .         49    y
%       3   8   13  .         48    ^
%       2   7   12  .         47    |
%       1   6   11  16  ...   46     -->x
%
% **********
%  Uses Matlab SPARSE matrix format for speed increase and size reduction
% **********

% DEFINE VARIABLES:

x = 177;
y = 50;
xy = x*y;
hx = 3.54/x;
hy = 1.00/y;
theta = hx/hy;
km = 6;
conc = 8e14;

% DEFINE MATRICES:

% --> Create square sub-matrices::

%  A is the center diagonal sub-matrix and carries info on y-dir BC.
%  Currently set to no-flux in +/- y-dir except as  modified below.
%
A = zeros(y);
A(1,1) = -2*(theta+1/theta);
A(1,2) = 2*theta;
A(y,y) = -2*(theta+1/theta);
A(y,(y-1)) = 2*theta;
temp = [theta -2*(theta+1/theta) theta];
for i=2:(y-1)
      A(i,i-1:i+1) = temp;
end

% B is off center diagonal sub-matrix and carries info on x-dir BC.
B = eye(y)*(1/theta);

temp = [B A B];

% F is text file which defines the reactivity on the surface.
```

```
% -----
% Uniform "gray" surface -
%
F = ones(1,x);
% -----
% load F.txt

%     Create master matrix of zeros in sparse format with a max # of
% --> nonzero elements = 5*(grid points) [not optimized but is max
%     possible] and fill::

amatrix = spalloc(xy,xy,5*xy);

% Fill first and last master row:
%     - currently set to no-flux BC in +/- x-dir.
%
amatrix(1:y,1:y) = A;
amatrix(1:y,(y+1):2*y) = 2*B;
amatrix((xy-y+1):(xy),(xy-y+1):(xy)) = A;
amatrix((xy-y+1):(xy),(xy-2*y+1):(xy-y)) = 2*B;

% Remaining middle master rows:
%
for j=1:(x-2)
      amatrix(y*j+1:y*j+y,y*(j-1)+1:y*(j-1)+3*y) = temp;
end

      % Up to this point, the problem is defined with symmetric no-flux
      % B.C.'s at all four boundaries.  To make problem interesting,
      % need to include sink at surface plus source at filament.

% Set correct reactivity at surface:
%
for k=0:(x-1)
      amatrix(y*k+1,y*k+1) = -2*(theta*(1+hy*km*F(k+1))+1/theta);
end

% Set filament concentration at y(max):
%  Sparse matrix allocation for bmatrix would need to be increased for
%  anything more than a few grid points.
%
bmatrix = spalloc(xy,1,5);
% (a) set filament conc + allow for diffusion
% amatrix(xy,xy) = 0;
% bmatrix(xy,1) = 2*(theta+1/theta)*conc;
% (b) just set filament element = C, a const. val. directly
amatrix(xy,:) = zeros(1,xy);
amatrix(xy,xy) = 1;
bmatrix(xy,1) = conc;

% Clean up after myself
%
clear A B F temp i j k x y xy hx hy theta km conc
```